Università degli Studi di Firenze

DOTTORATO DI RICERCA IN
"*ATOMIC AND MOLECULAR SPECTROSCOPY*"

CICLO XXV

COORDINATORE Prof. FRANCESCO PAVONE

"Adaptive Detection of Arbitrarily Shaped Ultrashort Quantum Light States"

Settore Scientifico Disciplinare: FIS/03

Dottoranda
Dott. CONSTANTINA POLYCARPOU

_____
(firma)

Tutore
DR. MARCO BELLINI

_____
(firma)

Table of Contents

INTRODUCTION

The story of the sole journey of a single photon has been long told before and so has the one of his nearly identical twin. Nonetheless, it has been the uniqueness of their relationship in the vast choice in nature, that has triggered the scientific community to invest its time and resources in it. The 1935 paper by Einstein, Podolski and Rosen "Can Quantum-Mechanical Description of Physical Reality be considered complete?" [2], was only the beginning to a new exciting field of research, in which people are occupied with the extraordinary properties encountered in the microscopic world and with ways to exploit them for classically impossible tasks. In fact, research on fundamental tests of quantum mechanics, besides being one of the most fascinating current paths to the advancement in human knowledge, could soon lead to major advancements also from the technological point of view.

In particular, the discipline of quantum optics studies the quantum nature of light. Light has been often chosen as a study object for many reasons. In the experimental field, there have been great advancements that provided the tools for this research, lasers generating light of superb quality, devices processing light with great precision, and extremely sensitive detectors for measuring the quantum properties of light. The simplest quantum state of light is a single photon, the basis of most fundamental tests of quantum mechanics and of possible applications of light to future quantum technologies.

Most of the experiments performed so far in the field of quantum optics have relied on the generation, manipulation, and detection of single photons and other nonclassical light states in single, well-defined modes. Generation of

quantum light in a superposition of two spatial or spectrotemporal modes has been used to encode quantum information (e.g., time-bin schemes [3,4]) or for metrological applications [5,6]. However, simple single- or two-mode systems limit capacity in the communication, manipulation, and storage of quantum information and, equally importantly, are not able to seize the complexity of realistic states in the laboratory.

The possibility of using multimode quantum states of light, i.e., a single beam holding several independent quantum channels, may offer many advantages. As much as wavelength multiplexing has revolutionized the area of optical telecommunications, multimode states have the potential to boost the complexity of quantum networks and enhance the execution of quantum information protocols [7,8]. In the spatial domain, the orbital angular momentum of single photons has been explored [9,10], and multimode states have been used in quantum imaging applications [11–13]. In the spectral and temporal domain, they have been proposed for cluster-state quantum computing [14] and for enhanced time metrology [15,16]. The encoding of quantum information in the spectrotemporal degrees of freedom of a single photon has also been proposed for novel quantum cryptographic schemes, such as differential phase shift quantum key distribution [17].

Moreover, the modes where the quantum states are prepared often do not perfectly coincide with those used for their processing and detection, and this may degrade the quality of applications based on such states. For example, future quantum networks require that light not only conveys information through optical links but also interacts with atomic species, allowing one to perform quantum processing and implement memory units [18,19]. These tasks demand a very specific and precise preparation of the photonic wave packet, i.e., of its spatiotemporal mode, such that it optimally couples to the

different possible interfaces. This goal has already motivated a series of theoretical proposals [20,21] and experiments with ultrafast [22] and quasi-cw [23,24] single photons and with shaped two-photon wave packets [25].

We have developed an adaptive method to realize the mode-selective detection of quantum light states [1]. Besides demonstrating the capability to detect and characterize states in unknown and arbitrarily shaped modes, we also show that our scheme can be an important tool for novel quantum information protocols based on the encoding of qubits and qudits onto the spatiotemporal degrees of freedom of light.

The main idea relies on optimally mapping the mode structure of a general quantum light state onto that of an intense coherent field (the so-called local oscillator, LO). In a typical experiment for the complete tomographic reconstruction of some quantum light state, homodyne detection only works with sufficient efficiency if the mode of the reference classical coherent field is perfectly matched to that of the state under examination [26,27]. If little or no prior information on such a mode is at hand, or if the mode itself has been somehow distorted during the propagation from the source to the detector, one may completely miss the target in the detection stage.

Here, we use the measured homodyne data to extract the fitness parameter for a genetic algorithm. The shape of the LO mode is first adaptively adjusted to best match the one of the quantum light state. Successively, the complex mode of the quantum state is fully characterized by measurements on the optimized local oscillator.

We put this approach to a first stringent experimental test by analyzing the spectrotemporal (ST) mode of ultrashort single photons (in a well-defined

spatial mode) with a combination of techniques from the fields of ultrafast coherent control and quantum optics. Choosing to use ultrashort quantum states offers the advantage of an extended bandwidth that allows encoding more information in ST modes, higher rate of information transfer, more precise timing, etc. However, it is important to note that our method is much more general and certainly not confined to ST modes (the full spatiotemporal mode characterization can be simply achieved by also introducing a spatial modulation of the LO [28]) or to the detection of single photons.

Different from recent schemes using two-photon interference with a reference coherent field [29], our method can be effectively applied to any quantum state, including bright multiphoton ones, provided a suitable optimization parameter is at hand (e.g., the noise variance in an experiment for the generation of squeezed states). Furthermore, our method is not limited to retrieving the ‘‘shape’’ of quantum light: it directly provides the tools for manipulating and analyzing it. Our scheme is also superior to those involving array detection [30–32], which to our knowledge have never been used to probe any nonclassical state in the ST domain because of high losses and experimental complexity.

We thus have in our hands an ultraprecise measuring tool to not only control but deeply probe the complex mode structure of arbitrary quantum states, a prerequisite for the processing, detection and manipulation of photonic states and, moreover, for their application to the development of novel quantum information technologies.

Before I go into the details of the technique and the stages of setting up the experiment, I will provide a theoretical overview of each individual part of the setup. Starting with the generation of nonclassical light states, the 1st

chapter of the thesis is dedicated to the theory of Quantum Optics that is of interest for this experiment. The generation of ultrashort quantum light states by means of Spontaneous Parametric Down Conversion (SPDC) is a common way to obtain nonclassical states of light starting from a coherent laser source. A pump photon is converted into two lower energy photons correlated in frequency and wavevector and emitted in two channels named signal and idler. Following that, Homodyne Detection in combination to Optical homodyne tomography is used as the characterisation scheme for the nonclassical quantum light states. Repeated measurements on identically prepared states allows the reconstruction of the state density operator that can be represented in phase-space by quasi-probability distributions, which allow one to calculate the expectation value of any physical quantity in analogy to classical distributions. This is where the Wigner distribution comes to play a significant role, having a particular characteristic different from classical distributions that it can assume negative values, a hallmark of nonclassical behaviour. Balanced homodyne tomography, by measuring the field statistics in phase-space, allows one to reconstruct the density operator and its Wigner representations.

The 2nd chapter is dedicated to the mathematical representations from Ultrafast Optics, starting with the description of a femtosecond laser pulse, with particular emphasis to the spectral phase and its importance in the femtosecond regime, to pulse compression methods and the mathematical description of pulse modulation using a Spatial Light Modulator. Following that, I will speak of the experimental methods used in the 3rd chapter, only to prepare the ground for a better understanding of the last chapter where the experiment is described. It is about the use of new devices linked to pulse shaping and its diagnostic tools, like the Spatial Light Modulator (SLM) and the Frequency Resolved Optical Gating (FROG), including alignment and

calibration methods we tried in the laboratory. Finally, after reading the first 3 chapters, the reader can be in a better position to follow the development of the experiment described thoroughly in chapter 4, and appreciate the success of the measurements, proving the validity of this innovative method and its superiority to previous techniques applied in the field. Only then can one try to envision the possibilities and the future prospects it may offer, for which I will deliberate in the epilogue of this thesis.

List of Acronyms

AC	autocorrelator
APD	avalanche photodiode
BHD	balanced homodyne detection
BBO	beta-barium borate
BS	beam splitter
CCD	charge-coupled device
CW	continuous wave
FROG	frequency resolved optical gating
FTL	fourier transform limited
FWHM	full width at half maximum
GA	genetic algorithm
GDD	group delay dispersion
GPIB	general purpose interface bus
GVD	group velocity dispersion
HD	homodyne detection
HT	high transmission
HWP	half wave plate
IR	infrared
ITO	indium tin oxide
LC	liquid crystal
LO	local oscillator
MI	michelson interferometer
PDC	parametric down conversion
PZT	piezo-electric transducer
SHG	second harmonic generation
SLM	spatial light modulator
SMF	single mode fibre

SP	single photon
SPCM	single photon counting module
SPDC	spontaneous parametric down conversion
ST	spectrotemporal
SVEA	slowly varying envelope approximation
TBP	time-bandwidth product
UV	ultraviolet

CHAPTER 1

QUANTUM OPTICS

For my thesis, I have been occupied with nonclassical states of light and their generation by means of non-Gaussian operators. I will be providing a brief description of the phenomenon of Spontaneous Parametric Down Conversion, used for the generation of single-photon Fock states, as well as a brief guide to their characterisation by means of Homodyne Detection.

1.1 Nonclassical states of light: Single Photons

Nonclassical light, in contrary to classical light, and for the sake of clarity, is to refer to the light that can only be described by the quantised electromagnetic field and quantum mechanics [33-35]. In this case it is treated like a stream of photons, rather than electromagnetic waves, holding nonclassical properties such as quantum noise, which in its own turn relegates to the famous Heisenberg uncertainty principle.

The most representative state of all would be the "Fock state", or otherwise called "Number state", the quantum state containing a definite number of energy quanta. According to their definition, these states have a well-defined number of photons while their phase remains totally undefined. They constitute the essence of the quantum nature of light and are indispensable in research on the fundamental principles of quantum mechanics, and in applications such as the implementation of a qubit or quantum cryptography.

Let's consider a single mode field as follows:

$$\hat{E}(\bar{r},t) = i\sqrt{\frac{\hbar\omega}{2\varepsilon_0 V}}\left\{\hat{a}e^{-i(\bar{k}\bar{r}-\omega t)} - \hat{a}^{\dagger}e^{i(\bar{k}\bar{r}-\omega t)}\right\} \tag{3.1}$$

Where V is the quantization volume, $\hat{a}$ and $\hat{a}\dagger$ are the annihilation and creation operators respectively, for which the bosonic commutation relation

$$\left[\hat{a},\hat{a}^{\dagger}\right]=1 \tag{3.2}$$

applies [36-38], ω is the frequency, $\overline{k}$ is the wave vector and ε_0 is the dielectric constant.

The $\hat{x}$ and $\hat{y}$ variables are the quadratures of the electric field and are defined as

$$\hat{x}=\frac{\hat{a}+\hat{a}^{\dagger}}{\sqrt{2}} \tag{3.3}$$

and

$$\hat{y}=\frac{i\left(\hat{a}-\hat{a}^{\dagger}\right)}{\sqrt{2}} \tag{3.4}$$

Given the photon-number operator $\hat{n}=\hat{a}^{\dagger}\hat{a}$, Fock states, indicated by $|n\rangle$, are the eigenstates of the photon-number operator, and as such they have a perfectly fixed photon number *n*:

$$\hat{n}|n\rangle=n|n\rangle \tag{3.5}$$

If $|n\rangle$ is an eigenstate of $\hat{n}$, then $\hat{a}|n\rangle$ must be an eigenstate as well, with the eigenvalue $n-1$.

In fact,

$$\hat{n}\hat{a}|n\rangle=\hat{a}^{\dagger}\hat{a}^{2}|n\rangle=\left(\hat{a}\hat{a}^{\dagger}a-\hat{a}\right)|n\rangle=(n-1)\hat{a}|n\rangle \tag{3.6}$$

It can be proven in a similar way that $\hat{a}^{\dagger}$ is also an eigenstate of $\hat{n}$, with an eigenvalue of $n+1$.

Therefore we derive the fundamental relations:

$$\hat{a}|n\rangle=\sqrt{n}|n-1\rangle \tag{3.7}$$

$$\hat{a}^{\dagger}|n\rangle=\sqrt{n+1}|n+1\rangle \tag{3.8}$$

Because of these relations, we understand why $\hat{a}$ is called the annihilation operator and $\hat{a}^{\dagger}$ is called the creation operator. Their function on the photon number is to lower it or raise it in integer steps, respectively.

The Hamiltonian for a single-mode field, just like for the harmonic oscillator, is:

$$\hat{H} = \hbar\omega\left(\hat{a}^{\dagger}\hat{a} + \frac{1}{2}\right) \tag{3.9}$$

with eigenvalues $E_n = \hbar\omega\left(n + \frac{1}{2}\right)$, where n is an integer (n=0,1,2,..).

The energy of the vacuum state $|0\rangle$, is the so-called zero-point energy $\langle 0|\hat{H}|0\rangle = \frac{1}{2}\hbar\omega$.

In the Schrödinger representation the vacuum state wavefunction is:

$$\psi_0(x) = \sqrt[4]{\frac{2}{\pi}}\exp\left(-x^2\right) \tag{3.10}$$

If we apply the creation operator to the vacuum state we obtain the excited states of the number operator:

$$|n\rangle = \frac{\left(\hat{a}^{\dagger}\right)^n}{\sqrt{n!}}|0\rangle \tag{3.11}$$

If $H_n(x)$ is the n-th order of the Hermite polynomials, then, the corresponding wavefunctions of the excited states are:

$$\psi_n(x) = \frac{H_n\left(x\sqrt{2}\right)}{\sqrt{2^n n!}}\sqrt[4]{\frac{2}{\pi}}\exp\left(-x^2\right) \tag{3.12}$$

Furthermore, the Fock states are orthonormal because they are eigenstates of the Hermitian operator $\hat{n}$ and form a complete Hilbert-space basis, the Fock basis:

$$\langle n|n'\rangle = \delta_{nn'} \tag{3.13}$$

$$\sum_{n=0}^{\infty}|n\rangle\langle n| = 1 \tag{3.14}$$

The density matrix for a Fock state |n> has the simplest form $\rho_{nn} = 1$. Since the trace of a density matrix is normalized, all the other diagonal elements must be zero. The off-diagonal elements are zero as well.

This field state is very simple to formulate but difficult to fully understand and to generate experimentally. However, its value isn't only proven as a fundamental theoretical tool but also of its cornerstone role in applications of quantum mechanics.

1.2 Quantum state generation: Spontaneous Parametric Down-Conversion

"The quantum mechanical description of parametric fluorescence is the splitting of a single photon into two photons", reproducing the words of D.C.Burnham, who together with D.L.Weinberg, were the first to describe Spontaneous Parametric Down Conversion (SPDC) in their PRL paper of 1970 [39].

In the language of quantum mechanics, we would say that during the process of SPDC [40-42] a pump photon is annihilated into a non-linear crystal resulting in two lower-frequency photons produced simultaneously and within the coherence time of the pump. We would say that the two photons are entangled, their energy and momentum and polarisation being quantum-mechanically correlated, but these physical properties remain individually undefined until a measurement is performed on one of them. We shall below see the mathematical representation of this phenomenon and further characteristics of the particular case of Type-I non-collinear degenerate case that is of our interest.

SPDC is a probabilistic event, as occasionally photons from the "pump" beam of frequency ω_p, decay into pairs of new photons, namely signal and idler (

ω_s, ω_i) simultaneously ($t_i = t_s$). In order for this recipe to bind together, the laws of conservation of energy and momentum need to be satisfied:

$$\overline{k}_p = \overline{k}_s + \overline{k}_i \tag{3.15}$$

and

$$\omega_p = \omega_s + \omega_i \tag{3.16}$$

and therefore we expect the combined energy and momentum of our pair of photons to be equal to the one of the original photon (the state of the crystal is considered unchanged in the process).

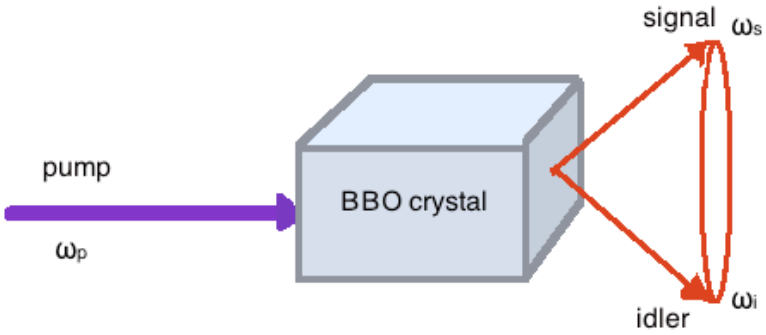

Figure 1.1 Schematic view of Spontaneous Parametric Down-conversion type I, where the nonlinear medium is a BBO crystal. A pump photon is converted into two lower energy photons correlated in frequency and wavevector and emitted in two channels named signal and idler.

For this three-wave mixing process to occur, one needs a non-linear medium, characterized by second order nonlinear susceptibility $\chi^{(2)}$, pumped by a strong laser beam. More generally, a noncentrosymmetric crystal (having a non-vanishing $\chi^{(2)}$) whose induced polarization depends quadratically on the incident pump field.

The electric field E_p incident on a nonlinear crystal creates a polarisation P having nonlinear dependence on E_p. The lowest nonlinearity order can be written as $P = \chi^{(2)} E_s E_i$, where E_i and E_s are the fields for the signal and idler channels respectively.

Assuming the signal and idler modes initially in the vacuum state (i.e. $|\psi(0)\rangle = |0\rangle_s |0\rangle_i$), the first-order perturbation theory gives the final two-photon state as

$$|\psi(t)\rangle = |0\rangle_s |0\rangle_i - \frac{i}{\hbar}\int_0^t dt' H_I(t') |0\rangle_s |0\rangle_i \tag{3.17}$$

where $H_I(t')$ is the Hamiltonian of the process of SPDC

$$H_I(t) = \chi^{(2)} \int_V E_s^{(-)}(\bar{r},t) E_i^{(-)}(\bar{r},t) E_p^{(+)}(\bar{r},t) d^3\bar{r} + h.c. \tag{3.18}$$

Since we are interested in the fields far from the crystal, and the interaction Hamiltonian is zero before the pump pulse enters the crystal and after the interaction, the time integration can be extended to run from -∞ to ∞; this leads to:

$$\int_{-\infty}^{+\infty} dt' \exp\left[-it'\left(\omega_s + \omega_i - \omega_p\right)\right] = \delta\left(\omega_s + \omega_i - \omega_p\right) \tag{3.19}$$

Therefore, the SPDC state vector reads as:

$$|\psi(t)\rangle = |0\rangle_s |0\rangle_i + \int d^3\bar{k}_s d\omega_s d^3\bar{k}_i d\omega_i \left(\bar{k}_s, \omega_s, \bar{k}_i, \omega_i\right) \left|1_{\bar{k}_s \omega_s}\right\rangle \left|1_{\bar{k}_i \omega_i}\right\rangle \tag{3.20}$$

where

$$\phi\left(\bar{k}_s, \omega_s, \bar{k}_i, \omega_i\right) = -\frac{i\chi^{(2)}}{\hbar} \int \varepsilon_p^{(+)}\left(\omega_s + \omega_i, \bar{k}_p\right) K\left(\bar{k}_p - \bar{k}_s - \bar{k}_i\right) d^3\bar{k}_p \tag{3.21}$$

and

$$K\left(\bar{k}\right) = \int_V \exp\left[-\bar{k}.\bar{r}\right] d^3\bar{r} \tag{3.22}$$

The function $\phi\left(\bar{k}_s, \omega_s, \bar{k}_i, \omega_i\right)$ describes the spatial and spectral properties of the two-photon state, which is sometimes called biphoton. The spatial and spectral behaviour of the biphoton state hence depends both on the spatial

and spectral distribution of the pump. The volume integration is performed as a transverse integral times an integral over the length of the crystal L. Assuming a crystal of infinite length and a pump beam infinitely wide in order to extend the transverse integral over an infinite domain, the above equation leads to the perfect spatial phase-matching condition:

$$K\left(\overline{k}_p-\overline{k}_s-\overline{k}_i\right)=\delta\left(\overline{k}_p-\overline{k}_s-\overline{k}_i\right) \tag{3.23}$$

In a more realistic case, where the pump beam is distributed in the transverse plane as a Gaussian of width Γ_p and is sufficiently wide in order to propagate along the crystal without any diffraction, $\Gamma_p \gg \sqrt{\lambda L/\pi}$, we obtain:

$$\begin{aligned}&\phi\left(\overline{k}_s,\omega_s,\overline{k}_i,\omega_i\right)=\\&-\frac{i\chi^{(2)}}{\hbar}\varepsilon_{pt}^{(+)}\left(k_z,\omega_s+\omega_i\right)\varepsilon_p^0 L\exp\left[-i\left(k_p-k_s-k_i\right)L/2\right]\\&\times\Gamma_p\exp\left[-\left(\kappa_i+\kappa_s\right)^2\left(\Gamma_p\right)^2/2\right]\frac{\sin\left(\left(k_p-k_s-k_i\right)L/2\right)}{\left(k_p-k_s-k_i\right)L/2}\end{aligned} \tag{3.24}$$

where the positive frequency part of the pump is factorised in the longitudinal and the transverse components $\varepsilon_p^{(+)}\left(\overline{k}_p,\omega_p\right)=\varepsilon_{pt}^{+}\left(k_z,\omega_p\right)\varepsilon_{ps}\left(\kappa\right)$ and $\tilde{\varepsilon}_{ps}\left(\rho\right)=\varepsilon_p^0\exp\left[-\rho^2/2\Gamma_p\right]$.

This equation shows that the down-conversion can be also obtained for "imperfect phase matching", and therefore SPDC is described by a spatial and spectral distribution. We have the maximum intensity of the output beams when the phase-matching conditions are exactly fulfilled. The two phase matching conditions can be combined to give the following constrains for the refractive index of the medium:

$$n\left(\omega_p\right)\left(\omega_s+\omega_i\right)=n\left(\omega_s\right)\omega_s+n\left(\omega_i\right)\omega_i \tag{3.25}$$

Because n is typically an increasing function of ω over the optical range of frequencies, the condition cannot be satisfied. However in a birefringent nonlinear medium it possible to achieve the above condition by making use of the different refraction index seen by waves propagating with different polarizations. In Type-I SPDC the signal and idler photons have the same polarisation but perpendicular to that of the pump, whereas in Type-II, they have perpendicular polarisations. SPDC process also distinguishes in degenerate if the two photons share the same free-space wavelength ($\lambda_i = \lambda_s = 2\lambda_p$), and in non-degenerate if they don't.

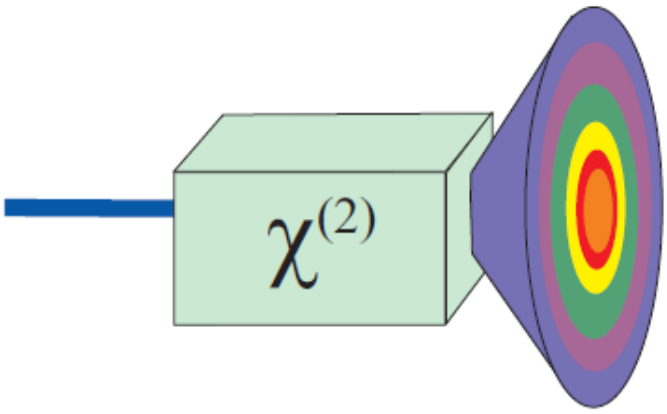

Figure 1.2 Spontaneous parametric down-conversion type I. A pump beam is injected on a nonlinear $\chi^{(2)}$ crystal and the down-converted light is emitted spontaneously in a form of a cone, with an angle of emission depending on the wavelength. The result is emission in concentric rings with the longer wavelengths in the centre and the shorter ones on the outsider circles.

In this thesis we are mainly concerned with Type-I, degenerate and slightly noncollinear down-conversion, and that is our single photon source. In this case the signal and idler photons emerge at equal yet opposite angles with respect to the beam direction. Since there is no preferred azimuthal angle for emission, the emerging radiation forms a ring of diametrically-opposed signal and idler photons.

1.3 Conditional generation of Fock states

As a single photon source to obtain photon-number states, we use conditional preparation from an SPDC source, which it is largely employed as a heralded single-photon source [43,44]. The ideal single photon source would be emitting upon the onset of a classical trigger, in a well-defined spatiotemporal mode but since that is yet not possible, the best and most efficient way is the technique of preparing single photons by conditional measurements on the biphoton state born in the process of parametric down-conversion.

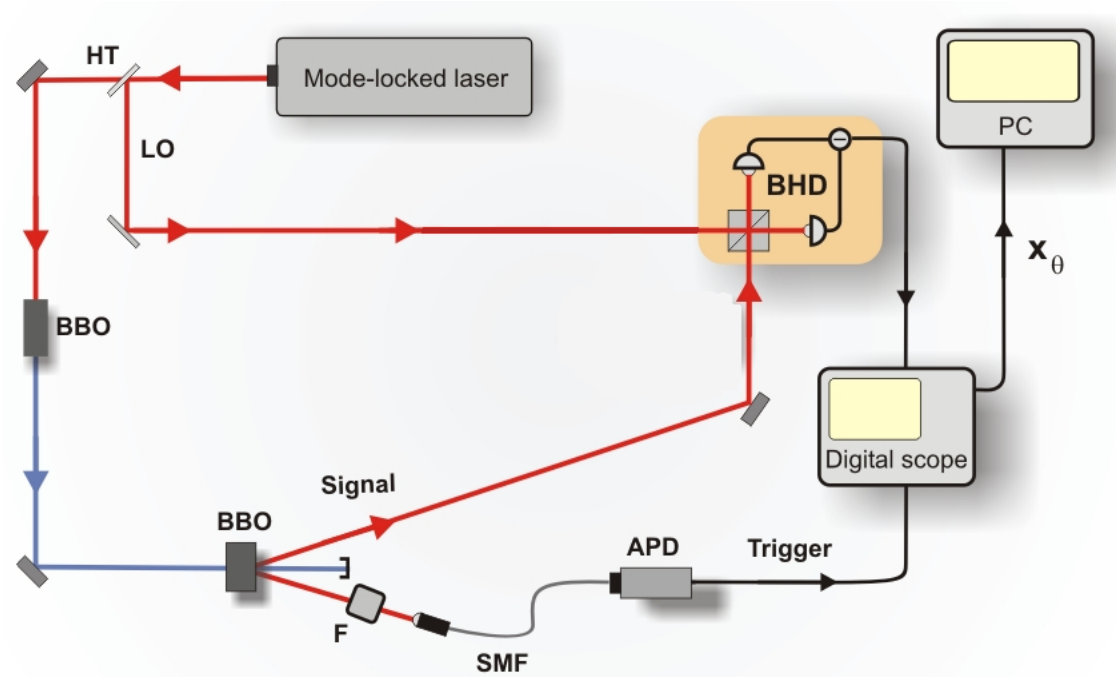

Figure 1.3 Conditional generation of the single-photon state by detection in the filtered trigger channel: when the single-photon counter (APD) "clicks" the signal field is projected into the Fock state.

The detection of a single-photon in a filtered idler channel projects the signal in a single-photon state. The idler photon, also named trigger photon, is selected by spatial and spectral filters. Because the emission of the two

photons is simultaneous, the single-photon Fock state in the signal channel is non-locally conditioned by the single-photon detection event in the idler one. The signal state preparation can be described by the following projection:

$$\hat{\rho}_s = tr_t\left\{\hat{\rho}_t|\psi\rangle\langle\psi|\right\} \tag{3.26}$$

where tr_t is the trace taken over the trigger states, $|\psi\rangle$ is the SPDC bi-photon state and $\hat{\rho}_t$ is the state ensemble selected by the trigger filters:

$$\hat{\rho}_t \int d^3k_t d\omega_t T\left(\overline{k}_t,\omega_t\right)\left|1\overline{k}_t,\omega_t\right\rangle_t\left\langle 1\overline{k}_t,\omega_t\right| \tag{3.27}$$

where $T\left(\overline{k}_t,\omega_t\right)$ is the filter spatiotemporal transmission function. An explicit calculation shows that the degree of spatial and spectral filtering of the trigger mode before detection determines the purity P of the generated quantum state in the signal mode. Only limiting ourselves to the case of the spectrotemporal contribution to the purity, one easily finds that it can be expressed as

$$P_t = \frac{1}{\sqrt{1+\sigma_f^2/\sigma_p^2}} \tag{3.28}$$

if one assumes a Gaussian spectral distributions of widths σ_f and σ_p for the filter and the pump field, respectively. We see from the above function that the purity of the generated state depends on the ratio between the pump and filter widths and it approaches unity only when the filter bandwidth is much smaller than the pump one. This is the reason why in order to obtain a pure single photon state whose properties are defined by the pump, we introduce narrowband filtering in the idler channel [45-48].

Generation of a two-photon Fock state is also possible and follows similar formalism as above, but it is much less probable and therefore much less efficient with use of SPDC process.

1.4 Quasi probability distribution and Wigner function

The cornerstone of quantum mechanics, the Heisenberg uncertainty principle, forbids simultaneous measurement of the variables x position and y momentum. This means that in quantum mechanics the construction of a probability distribution becomes problematic, which is the usual way of description of a system in classical mechanics. One simply needs to introduce a joint distribution for the position x and momentum y in a phase-space picture and when this joint probability distribution $P(x,y,t)$ is known, it is possible to calculate an expectation value for all the physical quantities of the system of interest. By joint probability, we refer to the probability of finding a certain value x and a certain value y in a simultaneous measurement, meaning at the same time t. Returning to the Heisenberg uncertainty principle we realize why this would be impossible for a quantum system.

The solution was provided by Wigner, who introduced the idea of a quasi-probability distribution in phase space, in 1932 [49]. A quasi probability distribution still allows one to calculate expectation values but, differently from a proper probability distribution, can also have negative regions. The latter turns out to be a very important quality as it is assumed as a proof of the nonclassicality of a state (a sufficient but not necessary criterion).

The Wigner function is defined by Wigner's formula as follows:

$$W(x,y)=\frac{1}{2\pi}\int_{-\infty}^{+\infty}e^{iy\xi}\left\langle x-\frac{\xi}{2}\middle|\hat{\rho}\middle|x+\frac{\xi}{2}\right\rangle d\xi \tag{3.29}$$

A notable property of the Wigner function is the overlap formula, as it allows calculation of the expectation values of observables:

$$Tr\left(\hat{\rho}_1\hat{\rho}_2\right)=2\pi\int_{-\infty}^{+\infty}\int_{-\infty}^{+\infty}W_1(x,y)W_2(x,y)dxdy \tag{3.30}$$

where W_1 and W_2 are the Wigner functions for the density operators $\hat{\rho}_1$ and $\hat{\rho}_2$.

So according to the above, the expectation value for an observable $\hat{A}$ is:

$$\left\langle \hat{A} \right\rangle = tr\left\{ \hat{\rho}\hat{A} \right\} = \int W(x,y) W_A(x,y)\, dxdy \tag{3.31}$$

Furthermore, if we integrate the Wigner function over one variable, we obtain the measurable probability distribution for the conjugated one –these are the so-called Marginal distributions:

$$\rho(x) = \left\langle x \middle| \hat{\rho} \middle| x \right\rangle = \int_{-\infty}^{+\infty} W(x,y) dy\,,\ \rho(y) = \left\langle y \middle| \hat{\rho} \middle| y \right\rangle = \int_{-\infty}^{+\infty} W(x,y) dx \tag{3.32}$$

In the case of a rotation by an angle θ in the space (*x,y*) the probability distribution of a rotated variable can be calculated using the Wigner representation as follows:

$$p(x,\theta) \equiv \left\langle x \middle| \hat{U}(\theta) \hat{\rho} \hat{U}^{+}(\theta) \middle| x \right\rangle = \int_{-\infty}^{+\infty} W(x\cos\theta - y\sin\theta, x\sin\theta + y\cos\theta) dy \tag{3.33}$$

The Wigner function for a Fock state $|n\rangle$ is

$$W(x,y) = \frac{(-1)^n}{\pi} L_n\left(2x^2 + 2y^2\right) e^{-x^2-y^2} \tag{3.34}$$

where L_n is the Laguerre polynomial of order n.

The Wigner representation for the vacuum state and the Fock states with *n*=1 and *n*=2 are respectively:

$$W_0(x,y) = \frac{2}{\pi} e^{\left(-2\left(x^2+y^2\right)\right)} \tag{3.35}$$

$$W_1(x,y) = \frac{2}{\pi} e^{\left(-2\left(x^2+y^2\right)\right)} \left(4x^2 + 4y^2 - 1\right) \tag{3.36}$$

$$W_2(x,y) = \frac{2}{\pi} e^{\left(-2\left(x^2+y^2\right)\right)} \left(1 + 8x^4 + 8y^4 - 8y^2 + 8x^2\left(2y^2 - 1\right)\right) \tag{3.37}$$

As we see from the image below, the nonclassical character of the Fock state, is made more than clear by the negativity of the Wigner function. Compared

to other representation of quantum states the Wigner has the advantage that it can be reconstructed from the experimental data and therefore constitutes a direct link between theory and experiment, providing an experimental tool for proving the nonclassicality of light states.

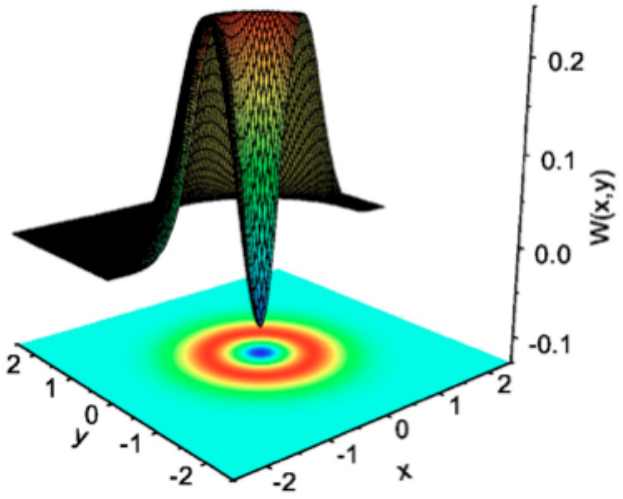

Figure 1.4 Reconstructed Wigner function for a single-photon Fock state [44].

1.5 Quantum state characterisation: Homodyne Detection and Quantum Tomography

Homodyne detection is a powerful method for measuring phase sensitive properties of travelling optical fields, which are suitable for quantum-state reconstruction. The scheme is basically the following: two fields are combined, through a lossless beam splitter, and forced to interfere with each other. A weak signal field with a highly stable reference field, which has the same mid-frequency as the signal field. The reference field, called local oscillator (LO), is usually prepared in a coherent state of large photon number. The superimposed fields impinge on two photodetectors,

the difference in the number of the emitted (and electronically processed) photoelectrons being the homodyne detection output.

The observed signal, which varies with the relative phase between the two fields, reflect the quantum statistics of the signal field and can be used – under certain circumstances – to reconstruct its quantum state.

More specifically and in our particular case, we detect the interference products at the outputs of a 50:50 beam splitter where the signal interferes with a strong coherent field. The local oscillator is derived from the same source as the other beam we wish to detect. As we see at the figure below, at the two outputs of our interferometer, we have placed two proportional photodetectors, whose induced photocurrents are subtracted to give a signal proportional to the quadrature of the electric field we wish to detect.

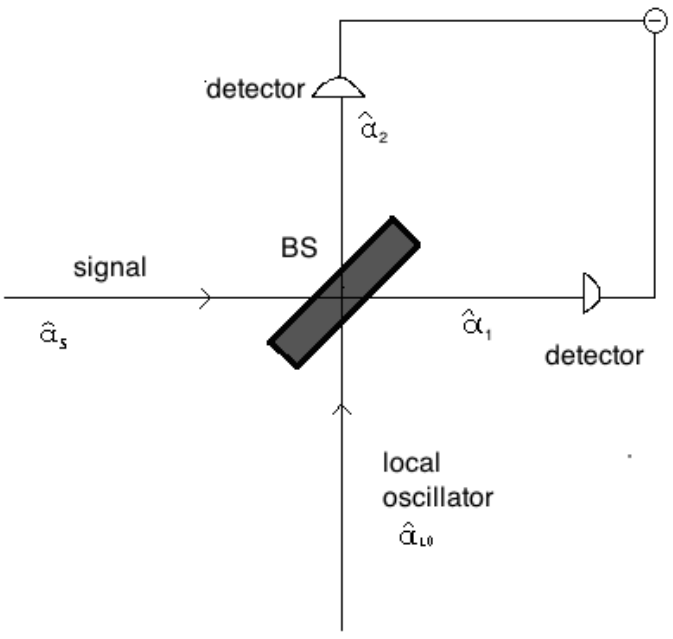

Figure 1.5 Diagram of a balanced Homodyne Detector.

The beam splitter is considered a passive device that neither creates nor destroys photons. We take r and t to be the (complex) reflectance and transmittance respectively, and for input states $\hat{a}_s$ the annihilation operator of the signal and $\hat{a}_{LO}$ the complex amplitude of the Local Oscillator, the beam splitter causes the following transformations:

$$\hat{a}_1 = t_1\hat{a}_s + r_2\hat{a}_{LO} \tag{3.38}$$

$$\hat{a}_2 = r_1\hat{a}_s + t_2\hat{a}_{LO} \tag{3.39}$$

where $\hat{a}_1$ and $\hat{a}_2$ are the mode operators of the fields emerging from the beam splitter.

If we consider the beam splitter to be lossless, then the coefficients r and t have to satisfy: $|r_{1,2}|^2 + |t_{1,2}|^2 = 1$ and $r_1 t_2^* + r_2 t_1^* = 0$.

We may now also consider a 50:50 Beam Splitter so that the conditions $t_1 = t_2 = 1/\sqrt{2}$ and $r_1 = -r_2 = 1/\sqrt{2}$ are imposed.

Now at the outputs of a 50:50 beam splitter we obtain:

$$\hat{a}_1 = \frac{1}{\sqrt{2}}\left(\hat{a}_s - \hat{a}_{LO}\right) \tag{3.40}$$

$$\hat{a}_2 = \frac{1}{\sqrt{2}}\left(\hat{a}_s + \hat{a}_{LO}\right) \tag{3.41}$$

We can calculate the photon number operators for the output channels 1 and 2, respectively:

$$\hat{n}_1 = \hat{a}_1^{\dagger}\hat{a}_1 = \frac{1}{2}\left(\hat{a}\dagger_s\,\hat{a}_s + \hat{a}\dagger_{LO}\,\hat{a}_{LO} - \hat{a}\dagger_s\,\hat{a}_{LO} - \hat{a}\dagger_{LO}\,\hat{a}_s\right) \tag{3.42}$$

$$\hat{n}_2 = \hat{\alpha}_2\hat{\alpha}_2 = \frac{1}{2}\left(\hat{a}\dagger_s\,\hat{a}_s + \hat{a}\dagger_{LO}\,\hat{a}_{LO} + \hat{a}\dagger_s\,\hat{a}_{LO} + \hat{a}\dagger_{LO}\,\hat{a}_s\right) \tag{3.43}$$

The photon number difference operator between the two channels is:

$$\hat{n}_{21} = \hat{n}_2 - \hat{n}_1 = \hat{a}\dagger_s\,\hat{a}_{LO} + \hat{a}\dagger_{LO}\,\hat{a}_s \tag{3.44}$$

If the local oscillator $|\alpha_{LO}\rangle = ||\alpha| e^{i\theta}\rangle$, is a strong coherent field, $|\alpha|^2 \gg 1$, such that it can be assumed to be classical and $|\alpha|^2 \gg Tr\left(\hat{\rho}\hat{\alpha}^{\dagger}\hat{\alpha}\right)$, then

the expectation value of the photon number difference we write

$$\langle \psi\alpha | \hat{n}_{21} | \psi\alpha \rangle = |\alpha| \langle \psi | \hat{a}^{\dagger} e^{-i\theta} + \hat{a} e^{i\theta} | \psi \rangle \tag{3.45}$$

where $|\psi\rangle$ is the state of the signal that is under investigation.

We define now the phase quadrature as follows:

$$\hat{x}_{\theta} = \hat{x}\cos\theta - \hat{y}\sin\theta \tag{3.46}$$

because the quadratures of the electric field (defined with equations 1.3 and 1.4) are $\hat{x} = \frac{1}{\sqrt{2}}\left(\hat{a}^{\dagger} + \hat{a}\right)$ and $\hat{y} = \frac{i}{\sqrt{2}}\left(\hat{a}^{\dagger} - \hat{a}\right)$ so that:

$$\hat{x}_{\theta} = \frac{1}{\sqrt{2}}\left(\hat{a}^{\dagger} e^{-i\theta} + \hat{a} e^{i\theta}\right) = \frac{\hat{n}_{21}}{\sqrt{2}|\alpha|} \tag{3.47}$$

and the expectation value for the photon number difference becomes:

$$\langle \psi\alpha | \hat{n}_{21} | \psi\alpha \rangle = \sqrt{2}|\alpha| \langle \psi | \hat{x}\cos\theta - \hat{y}\sin\theta | \psi \rangle = \sqrt{2}|\alpha| \langle \psi | \hat{x}_{\theta} | \psi \rangle \tag{3.48}$$

We see how the difference number operator, which is what we measure with homodyne detection, becomes linearly related to the field quadrature at a particular phase. Experimentally, we are able to adjust θ, the phase difference between the two fields, with the help of a mirror mounted on a piezoelectric translation stage. Repeating many times this measurement on identically prepared states, we collect an ensemble of data that is later used to construct an histrogram distribution of the quadrature operator P($\hat{x}$, θ), which is one of the marginal distributions of the state Wigner function.

At this point one can use a similar approach to that used in medicine to reconstruct the Wigner function of the state. In medical imaging a cross-section of the human body is scanned by a thin X-ray beam, whose attenuated intensity is recorded by a detector for different observation angles. The data of these intensity distributions are then processed by a computer to build a picture of the object in the form of a spatial distribution of the absorption coefficient.

Thanks to Vogel and Risken [50,51], the method was also applied in quantum optics to solve the problem of the limitation imposed by the Heisenberg uncertainty principle, that prevents the simultaneous and precise observation or measurement of the complementary features of a quantum state. Similarly the Wigner function can be recovered from its one-dimensional projections for different angles θ in phase-space, i.e. from the quadrature probability distributions, which can be precisely measured using balanced homodyne detection. To measure the quadrature distributions, we may fix the phase angle θ and perform a series of homodyne measurements at this particular phase to build up a quadrature histogram. Then the LO phase should be changed in order to repeat the procedure at a new phase, and so on. In quantum optics preparing a number of identically prepared light modes is not a problem, and repeated homodyne measurements on them can be implemented in order to gain sufficient statistical information about the quadrature values at a certain number or reference phases. This collection of data can be used then to tomographically reconstruct the Wigner function, a method called optical homodyne tomography.

CHAPTER 2

ULTRAFAST OPTICS

In our days lasers exist in a variety of complex setups but more and more interest has been attracted in the last decades by the development of new sources emitting very short pulses, with the latest records now reaching pulse durations of only a few optical cycles [55-57].

Along with this, and in analogy with electronic function generators comes the possibility to produce ultrafast optical waveforms. Powerful optical waveform synthesis methods have been developed, that allow generation of complicated ultrafast optical waveforms according to user specification. Coupled with the now widespread availability of femtosecond laser systems, pulse shaping systems are already having a strong impact as an experimental tool providing unprecedented control over ultrafast processes. We have used such a system in our lab, that has given us the possibility to characterise and exploit the broadband spectrum of our nonclassical light states.

2.1 Femtosecond Mode-locked Laser System

The most common form of ultrashort laser source, and the one we are using for the experiments of this thesis, is a mode-locked laser. In the following I will give a brief description of its working principle and characteristics.

In a general continuous wave multi-mode laser, the different longitudinal modes of the laser cavity oscillate independently of each other and have random relative phases. Since the total electromagnetic field at any point inside the cavity is given by the sum of the fields of the oscillating modes, the output of such a laser will be noise-like, fluctuating in intensity due to interference between the modes. However it is possible to manipulate the phases of the modes to obtain a more useful output, with a technique known as mode-locking.

A multi-mode laser is said mode-locked if its modes have a well-defined and fixed phase relationship. If the phases are locked in such way that there is a constructive interference between the modes at an instant and a destructive interference at other times, the output will appear as a pulse. It is instructive to consider a simple example of mode-locking in which all oscillating modes have equal amplitude. The electromagnetic field due to ***2n+1*** equally spaced modes is given by:

$$E(t) = \sum_{q=-n}^{n} E_q e^{i\left[(\omega_0 + q\Delta\omega)t + \varphi_q\right]} \tag{3.49}$$

where E_q is the amplitude of the q-th mode, ω_0 is the frequency of the central mode, $\Delta\omega$ is the (angular) frequency spacing between the modes and φ_q is the phase of the q-th mode.

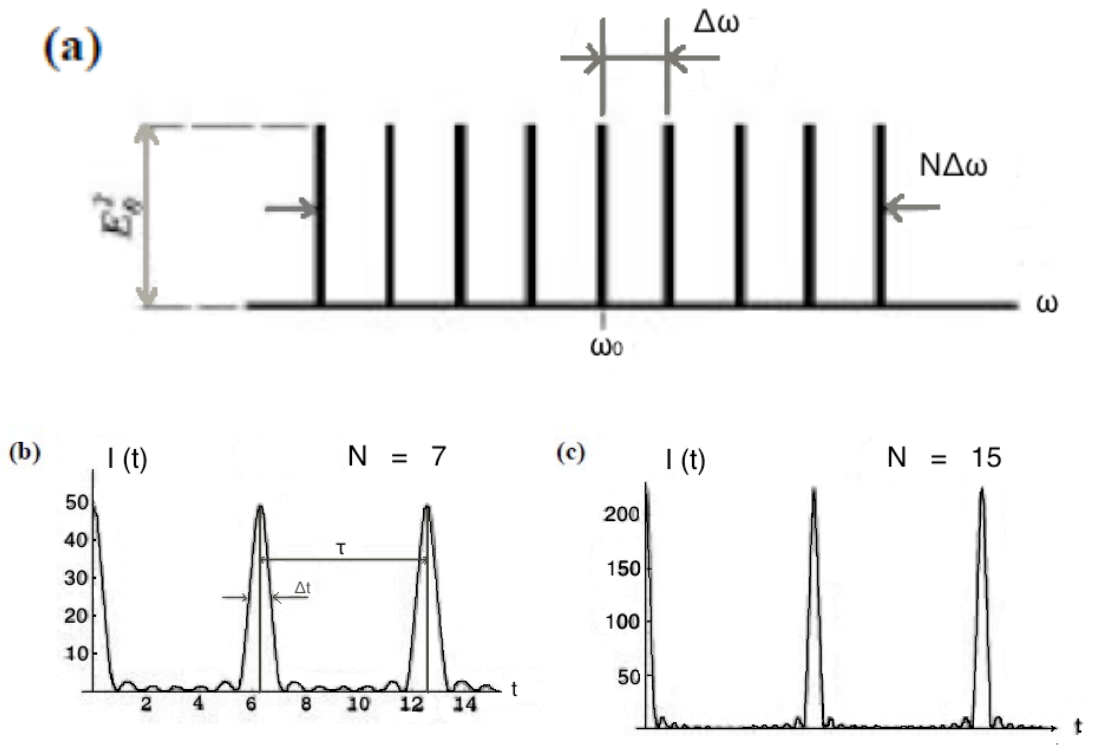

Figure 2.1 Mode locked output for the equal-amplitude approach. a) spectrum
b & c) the output in time domain (variation of intensity with time) for different numbers (N) of involved modes.

In the case of equal amplitudes (E_0) and locked phases ($\varphi_q - \varphi_{q-1} = const$) the above representation becomes:

$$E(t) = E_0 e^{i\omega_0 t} \sum_{q=-n}^{n} e^{iq\Delta\omega t} \tag{3.50}$$

This can be written as

$$E(t) = A(t) e^{i\omega_0 t} \tag{3.51}$$

where $A(t) = E_0 \sum_{q=-n}^{n} e^{iq\Delta\omega t}$.

This is an amplitude-modulated wave oscillating at the central mode frequency ω_0. The corresponding intensity profile is the following:

$$I(t) \propto \left[A(t)\right]^2 = \frac{\sin^2\left[(2n+1)\Delta\omega t/2\right]}{\sin^2(\Delta\omega t/2)} \tag{3.52}$$

The above function is periodic, with strong peaks (pulses) spaced by very weak subsidiary peaks. Careful analysis of the above function leads to acknowledgement of the importance of its properties: the pulse duration decreases and its amplitude increases as the number of modes increases; the period of this function is $T = 2\pi / \Delta\omega$. The pulse duration Δt can be approximately given as $\Delta t \approx 2\pi / (2n+1)\Delta\omega = 1/\Delta\nu$, where $\Delta\nu$ is the full width of the laser emission spectrum. Short pulses can be obtained from lasers with a large gain bandwidth. This is one of the main reasons for the choice of Ti:sapphire as the active medium of a pulsed laser in the visible and near-IR part of the spectrum. Ti:sapphire is basically a crystal of sapphire (Al_2O_3), doped with titanium ions, that has emission bandwidth covering the range approximately from 650 nm to 1150 nm with the maximum near 800 nm. Moreover, Ti:sapphire can be easily pumped in the blue-green range where some powerful laser sources are available (argon-ion lasers (514,5 nm) and frequency-doubled Nd:YAG, Nd:YLF and Nd:YVO lasers), and it has great photo- and thermo-resistance. Obviously, not only the active medium provides ability of a laser to generate ultra short pulses, it also depends on the possibility to compensate the dispersion due to all intracavity optical elements.

For our experiments, we used a CW Millennia (Newport) laser emitting 8 Watts at 532 nm to pump a mode-locked Ti:sapphire (Tsunami, Newport) laser providing ultrashort pulses of duration about 80 fs at 800 nm (FWHM 10 nm), with 82 MHz repetition rate and output power 1,5 Watt.

2.2 Mathematical description of femtosecond laser pulses

As a starting point, the real-valued scalar temporal electric field

$$E(t) = 2A(t)\cos\left(\Phi(t)\right) = A(t)e^{i\Phi(t)} + c.c. = E^{+}(t) + E^{-}(t) \tag{3.53}$$

is chosen to represent a laser pulse, which contains the real-valued temporal amplitude $A(t)$ (the envelope of the electric field) and the temporal phase function $\Phi(t)$. For an unambiguous description, it is sufficient to restrict the temporal electric field to the complex-valued function

$$E^{+}(t) = A(t)e^{i\Phi(t)} \tag{3.54}$$

The phase function $\Phi(t)$ in the expression for the electric field is responsible for the oscillation of the electric field. It is dominated by a term linear in time bringing forth the fast oscillations with the carrier frequency ω_0 of the light, but also comprises nonlinear contributions that are described by the function

$$\varphi(t) = \Phi(t) - \omega_0 t \tag{3.55}$$

The electric field can also be characterised by the carrier frequency ω_0 and a complex envelope $\hat{A}(t)$, so that it is written as

$$E^{+}(t) = A(t)e^{i\Phi(t)} \times e^{i\omega_0 t} = \hat{A}(t)e^{i\omega_0 t} \tag{3.56}$$

The above equation is called slowly-varying envelope approximation (SVEA) and is applicable for all but the shortest light pulses that are currently generated.

In the temporal domain we define the pulse intensity as the average of $E^2(t)$ over one optical cycle, and can be further simplified as follows:

$$I(t) = c_o \varepsilon_0 n \frac{1}{T} \int_{t-T/2}^{t+T/2} E^2(t')dt' = 2c_o \varepsilon_0 n A(t)^2 \tag{3.57}$$

where n is the index of refraction of the medium in which the intensity is measured.

The energy fluence F, i.e. the amount of energy per unit area contained in the electric field is given by

$$F = \int_{-\infty}^{\infty} I(t)dt \tag{3.58}$$

while the total pulse energy W is given by further integration over the spatial coordinates in the complete formula for the electric field.

The first derivative of the phase $\Phi(t)$ with respect to time yields the actual frequency with which an electric field oscillates at a given moment in time. This instantaneous frequency is

$$\omega_m(t) = \frac{d\Phi(t)}{dt} = \omega_0 + \frac{d\varphi(t)}{dt} \tag{3.59}$$

may vary significantly with time, and from the above equation the physical meaning of the reduced phase function $\varphi(t)$ obtained under the SVEA becomes obvious: it describes the deviation of the actual oscillation frequency from the carrier frequency ω_0.

The analysis of this term will be important for us in this thesis. In the case of a constant phase, the pulse experiences no frequency variation in time, whereas a linear variation of φ with time represents a simple frequency shift. However, a quadratic variation of φ with time, starts to make it more interesting as it represents a linear ramp of frequency versus time, and we say we have "positively chirped", or "negatively chirped" for increasing or a decreasing ramp respectively. Then, the chirp is said to be linear for a simple quadratic phase distortion and nonlinear when higher order terms get involved in our function.

It is useful to expand the temporal phase into a Taylor series

$$\Phi(t) = \sum_{j=0}^{\infty} \frac{a_j}{j!} t^j \tag{3.60}$$

with coefficients a_j defined as

$$a_j = \left. \frac{d^j \Phi(t)}{dt^j} \right|_{t=0} \tag{3.61}$$

The zeroth-order coefficient a_0 determines the position of the peaks of the actual oscillation with respect to the pulse envelope, and is called the absolute phase (or carrier-envelope phase). In conventional femtosecond laser systems, the absolute phase does not remain constant but fluctuates from pulse to pulse, an effect that can be overcome by an interferometric setup used to stabilise a_0. It has been demonstrated that the absolute phase may play an important role in experiment with few-cycle pulses but for the typical pulses of this thesis it is not important.

The first-order coefficient is identical to the carrier frequency $a_1 = \omega_0$, high-order terms lead to a variation in the carrier frequency ω_0. When $a_j = 0$ for all $j \geq 2$, the pulse is unchirped, and $\omega_m(t)$ is constant. In contrast, if $\omega_m(t)$ is increasing with time (i.e. $\frac{d\omega_m(t)}{dt} > 0$), one speaks of upchirped laser pulses, while the pulse is downchirped if $\frac{d\omega_m(t)}{dt} < 0$).

For complex pulse shapes, the momentary frequency may vary from upchirped to downchirped character several times. In the special case $a_2 \neq 0$ and $a_j = 0$ for all $j \geq 3$, the momentary frequency changes linearly with time, and thus the pulse is linearly chirped.

The electric field can also be characterised in the spectral domain, which is connected to the temporal domain via the Fourier transform (denoted by F)

$$E(\omega) = \frac{1}{\sqrt{2\pi}} \int_{-\infty}^{\infty} E(t) e^{-i\omega t} dt = F\{E(t)\} \tag{3.62}$$

The inverse Fourier transform (denoted by F^{-1})

$$E(t) = \frac{1}{\sqrt{2\pi}} \int_{-\infty}^{\infty} E(\omega) e^{i\omega t} d\omega = F^{-1}\{E(\omega)\} \tag{3.63}$$

reproduces the temporal electric field $E(t)$.

Since $E(t)$ is a real-valued function, the electric field in the spectral domain has contributions both at positive and negative frequencies, which obey the relation

$$E(\omega) = E^*(-\omega) \tag{3.64}$$

where the star indicates complex conjugation.

Therefore, the field still is unambiguously characterised if the description is restricted to the part at positive frequencies:

$$E^+(\omega) = \begin{cases} E(\omega) \xrightarrow{if} \omega \geq 0 \\ 0 \xrightarrow{if} \omega < 0 \end{cases} \tag{3.65}$$

This expression can be divided into a real-valued spectral amplitude (or envelope) function $A(\omega)$ (spectrum) and an exponential term containing the spectral phase $\Phi(\omega)$:

$$E^+(\omega) = A(\omega) e^{-i\Phi(\omega)} \tag{3.66}$$

Similarly to the Fourier transform relation for the complete fields $E(t)$ and $E(\omega)$, the electric field $E^+(\omega)$,

$$E^+(\omega) = F\{E^+(t)\} \tag{3.67}$$

is connected to its Fourier counterpart $E^+(t)$ by

$$E^+(t) = F^{-1}\left\{E^+(\omega)\right\} \tag{3.68}$$

and the spectral intensity in analogy to Eq.(2.9) is defined as

$$I(\omega) = 2c_o\varepsilon_0 nA(\omega)^2 \tag{3.69}$$

Since the energy fluence, is a property of the laser pulse that is obtainable by either describing the field in time or frequency space, the condition

$$F = \int_{-\infty}^{\infty} I(t)dt = \int_{-\infty}^{\infty} I(\omega)d\omega \tag{3.70}$$

known as Parseval's Theorem is fulfilled.

Just like in the time domain, it is useful to expand the phase into a Taylor series. The spectral amplitude is usually centred around the carrier frequency ω_0, so the expansion is most conveniently performed according to

$$\Phi(\omega) = \sum_{j=0}^{\infty} \frac{b_j}{j!}(\omega - \omega_0)^j \tag{3.71}$$

With the spectral phase coefficients

$$b_j = \left.\frac{d^j\Phi(\omega)}{d\omega^j}\right|_{\omega=\omega_0} \tag{3.72}$$

The zeroth order coefficient is identical to the absolute phase, i.e $b_0 = a_0$. The coefficient of first order is equivalent to a translation of the laser pulse in the time domain, as can be explained by the Fourier transform of an arbitrary field $E(\omega)$ with an additional linear spectral phase term b_1. The associated temporal field then becomes

$$F^{-1}\left\{E(\omega)\times e^{-b_1\omega}\right\} = \frac{1}{2\pi}\int_{-\infty}^{\infty} E(\omega)e^{i\omega(t-b_1)}d\omega = E(t-b_1) \tag{3.73}$$

It is now useful to introduce parameters to describe how long our pulse and broad its spectrum is, as well as a constant called the time bandwidth product (TBP) that defines a relationship between the two.

The spectral width $\Delta\omega$ and the pulse duration Δt are defined as the full width at half maximum of the associated intensity profiles

$$\Delta\omega = FWHM\left\{I(\omega)\right\} \tag{3.74}$$

$$\Delta t = FWHM\left\{I(t)\right\} \tag{3.75}$$

It is clear from the Fourier transform that the electric fields in time and frequency space are directly related and therefore they cannot vary independently of each other.

The so-called time-bandwidth product sets a lower limit to their relationship as follows [58]:

$$\Delta\omega\Delta t \geq 2\pi c_B \tag{3.76}$$

where c_B is a constant on the order of one, which depends on the actual pulse shape and on the definition of the quantities $\Delta\omega$ and Δt. If they are defined as above then $c_B = 4\ln(2)/(2\pi) = 0.441$ in case of Gaussian-shaped spectrum, while it is different for other $I(\omega)$ profiles.

The quantities $\Delta\omega$ and Δt as defined above are only a good measure for pulses that are not very complex. For structured pulses, different concepts have been developed in order to consider the complete intensity distribution in an estimate of the pulse properties but an exact description of complex pulses is only given by the complete electric field functions.

A pulse is called bandwidth-limited or transform-limited if the equality sign in the equation of the time-bandwidth product holds. This is the case for any

given spectrum if all $b_j = 0$ for $j \geq 2$ in the Taylor expansion. Analogously, for a given temporal intensity profile the narrowest spectrum, with which a pulse can be obtained, is found by setting all $a_j = 0$ for $j \geq 2$.

2.2.1 Spatial propagation and material dispersion

Now that the description of the electromagnetic field of our ultrashort pulses has been completed, we have to consider its propagation in space and in dispersive or non-dispersive media and see how its properties would change.

We start with the wave equation, assuming a plane wave as follows

$$\left(\frac{\partial^2}{\partial z^2} - \frac{1}{c^2}\frac{\partial^2}{\partial t^2}\right) E(t,z) = \mu_0 \frac{\partial^2}{\partial t^2} P(t,\bar{r}) \tag{3.77}$$

where $\bar{P}(t,\bar{r})$ is the polarisation and it is treated like in classical electrodynamics, so that it can be assumed to be a linear response to the electric field $E(t,z)$. The two quantities are connected through the dielectric susceptibility tensor χ, leading to the simple relation

$$P(\omega,z) = \varepsilon_0 \chi(\omega) E(\omega,z) \tag{3.78}$$

in the spectral domain.

Combination of the above equation (2.30) and the Fourier transform of the previous eq. (2.29) results in the further reduced wave equation

$$\left(\frac{\partial^2}{\partial z^2} + \frac{\omega^2}{c^2}\left[1 + \chi(\omega)\right]\right) E(\omega,z) = 0 \tag{3.79}$$

Solutions for this equation are the traveling waves

$$E(\omega,z) = E^+(\omega,0) e^{-ik(\omega)z} + c.c. = E^+(\omega,z) + E^-(\omega,z) \tag{3.80}$$

The expression $E^+(\omega,0)$ is equivalent to $E^+(\omega)$ defined previously by Eq.(2.18) and the quantity

$$k = \frac{\omega}{c}\tilde{n}(\omega) \tag{3.81}$$

is the wavevector, pointing into the z-direction and containing the complex index of refraction

$$\tilde{n}(\omega) = n(\omega) - i\kappa(\omega) = \sqrt{1+\chi(\omega)} \tag{3.82}$$

While the imaginary part $\kappa(\omega)$ (extinction coefficient) is responsible for processes like absorption or gain in a medium, the real part $n(\omega)$ describes dispersion and refraction. For idealised propagation without losses, $\kappa(\omega)$ becomes zero, and the index of refraction reduces to the real part $n(\omega)$.

In analogy to the temporal domain, where the rapid oscillations in time with the carrier frequency ω_0 are separated from the phase function according to Eq.(2.11), the rapid oscillations in space can be factored out as follows:

$$E^+(\omega,z) = E^+(\omega,0)e^{-ik(\omega)z} = E^+(\omega,0)e^{-i\delta kz} \times e^{-ik_0 z} \tag{3.83}$$

With $k_0 = n(\omega_0)\omega_0 / c$ and δk defined by a Taylor expansion

$$\delta k = \sum_{j=1}^{\infty} \frac{1}{j!}\frac{d^j k}{d\omega^j}\bigg|_{\omega=\omega_0} (\omega-\omega_0)^j \tag{3.84}$$

If the SVEA is valid, it is therefore sufficient to describe the electric field by a complex envelope function

$$\hat{A}(\omega,z) = E^+(\omega,0)e^{-i\delta kz} = A(\omega,0)e^{-i\Phi(\omega,0)}e^{-i\delta kz} = A(\omega,0)e^{-i\varphi(\omega,z)} \tag{3.85}$$

that contains the reduced phase term $\varphi(\omega,z)$.

The SVEA in space requires that the pulse envelope does not change significantly while travelling a distance that is on the order of one wavelength $\lambda_0 = 2\pi / k_0$. Therefore the condition

$$\left|\frac{d}{dz}\hat{A}(\omega,z)\right| = k_0\left|\hat{A}(\omega,z)\right| \tag{3.86}$$

has to be fulfilled. By inverse Fourier transform of Eq.(2.35) the temporal electric field

$$E^+(t,z) = F^{-1}\left\{E^+(\omega,z)\right\} \tag{3.87}$$

is obtained, which now describes the temporal evolution and the spatial propagation of a laser pulse.

If Eq.(2.39) is rewritten in the form

$$E^+(t,z) = F^{-1}\left\{A(\omega,0)e^{-i\varphi(\omega,z)}e^{-i\delta kz}\right\}\times e^{i(\omega_0 t - k_0 z)} \tag{3.88}$$

The term resulting from the inverse Fourier transform yields the complex envelope function $\hat{A}(t,z)$ which varies slowly in time and space, and which contains the information about the shape and chirp of the laser pulse.

The combined description of the temporal and spatial properties of the electric field allows study of how laser pulses change while propagating through optical elements.

As an example a dispersive material of length L and with an index of refraction $n(\omega)$ is considered. Using the SVEA, the additional spectral phase acquired along propagation is

$$\Phi(\omega,L) = \Phi(\omega,0) + kL = \Phi(\omega,0) + \frac{\omega n(\omega) L}{c} \tag{3.89}$$

The additional contribution due to propagation has to be included in the Taylor expansion of the spectral phase, so that the coefficients b_j of Eq. (2.24) become

$$b_j = \left.\frac{d^j\Phi(\omega,L)}{d\omega^j}\right|_{\omega=\omega_0} = \left.\frac{d^j\Phi(\omega,0)}{d\omega^j}\right|_{\omega=\omega_0} + \frac{L}{c}\left.\left(j\frac{\partial^{j-1}n(\omega)}{\partial\omega^{j-1}} + \omega\frac{\partial^j n(\omega)}{\partial\omega^j}\right)\right|_{\omega=\omega_0} \quad (3.90)$$

If the pulse would propagate in vacuum, i.e. $n(\omega)=1$ for all frequencies, only the zero-order and the first-order coefficients would change by $k_0 L$ and by L/c respectively. This accounts for a constant phase $k_0 L$ and a temporal shift $\Delta t = L/c$ of the pulse's maximum due to propagation from the position z=0 to z=L.

For a dispersive medium, however, the situation is different, and the first order term takes the form

$$b_1 = \left.\frac{d\Phi(\omega,0)}{d\omega}\right|_{\omega=\omega_0} + \frac{L}{c}\left.\left(n+\omega\frac{dn(\omega)}{d\omega}\right)\right|_{\omega=\omega_0} = \left.\frac{d\Phi(\omega,0)}{d\omega}\right|_{\omega=\omega_0} + \frac{L}{\upsilon_g(\omega_0)} \quad (3.91)$$

where the group velocity $$\upsilon_g(\omega_0) = \left(\left.\frac{dk}{d\omega}\right|_{\omega=\omega_0}\right)^{-1} \quad (3.92)$$

is the actual velocity of the pulse envelope in the dispersive material, and the group delay

$$\tau_g(\omega_0) = \frac{L}{\upsilon_g(\omega_0)} \quad (3.93)$$

is the time it takes the pulse to propagate through the medium.

As already discussed the temporal shape of a laser pulse changes if the spectral phase coefficients b_j for $j \geq 2$ are altered. After passing the dispersive medium, the second-order coefficient has an additional contribution

$$\frac{L}{c}\left.\left(2\frac{\partial n(\omega)}{\partial\omega} + \omega\frac{\partial^2 n(\omega)}{\partial\omega^2}\right)\right|_{\omega=\omega_0} = \left.\frac{d\tau_g(\omega)}{d\omega}\right|_{\omega=\omega_0} \quad (3.94)$$

which is called group-delay dispersion (GDD) and is linear with respect to the traversed distance in the medium. Therefore, by dividing Eq.(2.46) by L the

linear dependence is cancelled and a characteristic property of the dispersive material is obtained, the so-called group velocity dispersion (GVD) parameter

$$\frac{1}{c}\left(2\frac{\partial n(\omega)}{\partial \omega}+\omega\frac{\partial^2 n(\omega)}{\partial \omega^2}\right)\Bigg|_{\omega=\omega_0}=\frac{d\left(\frac{1}{\upsilon_g(\omega)}\right)}{d\omega}\Bigg|_{\omega=\omega_0} \tag{3.95}$$

As we will see in the following, the coefficient b_2 will be occupying us and in the case that $b_2 \neq 0$, this leads to a linear chirp of the laser pulse. The GVD parameter can therefore be understood as amount of linear chirp introduced per unit distance in the medium. Similarly to b_2, higher-order coefficients of the spectral phase are also affected by propagation through a dispersive medium, and subsequently lead to a change in the temporal profile of the laser pulse. Thus, they always have to be considered in the design of femtosecond laser sources and whenever optical components like lenses, filters or attenuators are employed. Depending on pulse length and central wavelength, the effect may be more or less pronounced, and in general it is more drastic for shorter pulse durations and shorter wavelengths. For instance, propagation through 1 cm of Fused Silica will stretch (and thereby chirp) an initially transform-limited 80 fs pulse to 81 fs if centred at $\lambda_0 = 800$ nm, but to 87 fs or even 105 fs if the central wavelength is $\lambda_0 = 400$ nm or =266 nm, respectively.

However, no matter how complicated the spectral phase imposed onto a pulse by a dispersive material is, it is well determined by the index of refraction and the length of the medium, and therefore the phase relations between different frequency components are always unambiguously defined and can be derived with the equations discussed above. Therefore, a dispersive material and the length the light has to propagate through it can be

chosen in such a way, that the intended amount of chirp be imposed on the laser pulse.

2.3 Shaping of ultrafast waveforms: linear filtering

The linear filtering process can be described in either the time or the frequency domain, as depicted in the picture below[59].

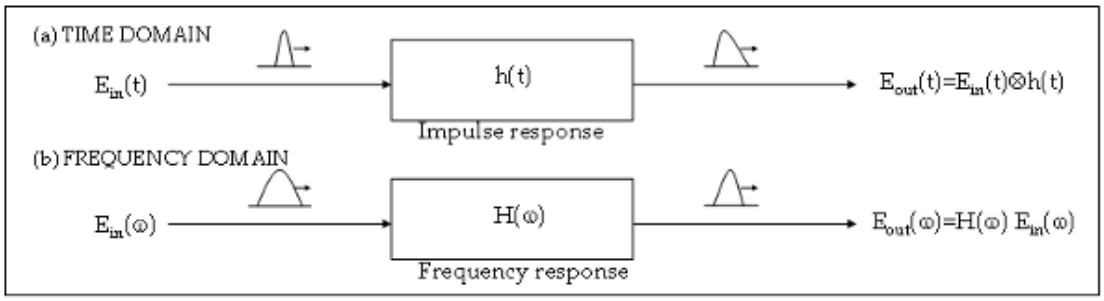

Figure 2.2 Pulse shaping by linear filtering: (a) time domain and (b) frequency domain

In the time domain the filter is characterised by its impulse response function $h(t)$. The output of the filter $E_{out}(t)$ in response to an input pulse $E_{in}(t)$is given by the convolution of $E_{in}(t)$ and $h(t)$:

$$E_{out}(t) = E_{in} * h(t) = \int dt' E_{in}(t') h(t - t') \tag{3.96}$$

where $*$ denotes convolution. If the input is a delta function, the output is simply $h(t)$. Therefore, for a sufficiently short input pulse, the problem of generating a specific output pulse shape is equivalent to the task of fabricating a linear filter with the desired impulse response.

In the frequency domain, the filter is characterised by its frequency response $H(\omega)$. The output of the linear filter $E_{out}(\omega)$ is the product of the input signal $E_{in}(\omega)$ and the frequency response $H(\omega)$, i.e.

$$E_{out}(\omega) = E_{in}(\omega) H(\omega) \tag{3.97}$$

Here $E_{in}(t)$, $E_{out}(t)$ and $h(t)$ and $E_{in}(\omega)$, $E_{out}(\omega)$ and $H(\omega)$ respectively, are Fourier transform pairs, i.e.

$$H(\omega) = \int dt h(t) e^{-i\omega t} \tag{3.98}$$

and

$$h(t) = \frac{1}{2\pi} \int d\omega H(\omega) e^{i\omega t} \tag{3.99}$$

For a delta function input pulse, the input spectrum $E_{in}(\omega)$ is equal to unity, and the output spectrum is equal to the frequency response of the filter. Therefore, due to the Fourier transform relations, generation of a desired output waveform can be accomplished by implementing a filter with the desired frequency response.

2.4 Mathematical representation of pulse modulation by a pulse shaper operating in the spectral domain

We shall be examining in the following the mathematical representation of the effect on the ultrashort pulse when travelling through a pulse shaping setup operating in the spectral domain [60-62].

As we already saw the output pulse $E_{out}(\omega)$ is the product of the input pulse $E_{in}(\omega)$ and the transfer modulation function $H(\omega)$, that describes the phase and/or amplitude modulation applied by the pulse shaping apparatus to the input pulse:

$$E_{out}(\omega) = H(\omega) E_{in}(\omega) \tag{3.100}$$

where ω is the angular frequency.

So, based on the above, one could easily obtain the modulation function to convert the input pulse to the desired output pulse, by simply dividing the

latter by the actual input pulse, provided that sufficient spectral bandwidth is available.

The general form of the applied modulation function is the following:

$$H_{appl}(\omega) = \left|A_{des}(\omega)\right| \exp\left[\frac{i}{2\pi}\left(\phi_{des}(\omega)+1\right)+\frac{i}{4}sign\left[A_{des}(\omega)\right]\right] \qquad (3.101)$$

where $A_{des}(\omega)$ is the desired spectral amplitude, $\phi_{des}(\omega)$ is the desired spectral phase and the function $sign(x)$ is defined as

$$\begin{aligned} sign(x) &= 1, \text{ for } x > 0 \\ &= 0, \text{ for } x = 0 \\ &= -1, \text{ for } x < 0 \end{aligned} \qquad (3.102)$$

The above function is useful for calculating the desired modulation to be performed with any pulse shaping device and setup.

However, in this thesis we are particularly interested in the modulation performed using a Liquid Crystal Spatial Light Modulator. Without going into much detail (it will be explained better later), it works by independently modulating the amplitude and phase of the different spectral components of the pulse. This can be achieved by using a voltage to modulate the index of refraction of a liquid crystal material as seen by light polarized along a particular direction. An input light field polarized along this direction can be accurately phase shifted by an amount ϕ.

The single-layer LC SLM depicted in figure 2.3 is typically used for phase-only pulse shaping. The double-layer LC SLM in the same figure is capable of phase and amplitude modulation. It consists of a polariser and two orthogonal LC layers whose axes are tilted at +45° and -45°relative to the input laser polarisation.

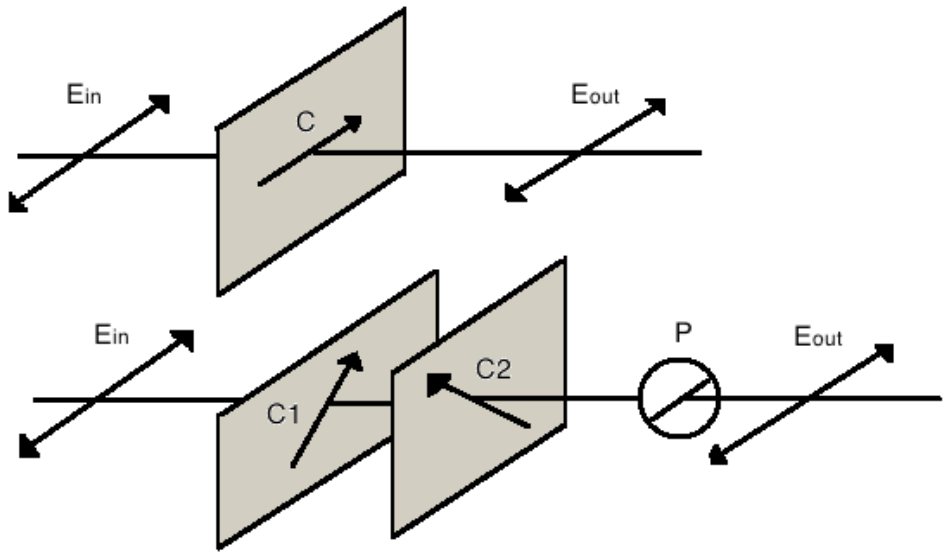

Figure 2.3 Common geometries for liquid crystals: Single-layer LC SLM for phase-only modulation (top) and Dual layer LC SLM with polarizer (P) for independent phase and amplitude modulation (bottom).

There is a very practical way to analyse the above configurations using Jones matrix formalism. The horizontally-polarised input light field is given by the vector E_{in} and the modulator, polariser and rotation matrices are given by $H(\phi)$, P_x and $R(\theta)$, respectively:

$$E_{in} = \begin{pmatrix} 1 \\ 0 \end{pmatrix} \tag{3.103}$$

$$H(\phi) = \begin{pmatrix} \exp(i\phi) & 0 \\ 0 & 1 \end{pmatrix} \tag{3.104}$$

$$P_x = \begin{pmatrix} 1 & 0 \\ 0 & 0 \end{pmatrix} \tag{3.105}$$

$$R(\theta) = \begin{pmatrix} \cos\theta & \sin\theta \\ -\sin\theta & \cos\theta \end{pmatrix} \tag{3.106}$$

Because the matrix $H(\phi)$ is written in its own coordinate system relative to its c-axis, a rotation matrix $R(\theta)$ is used to transform between x-y and the LC coordinate systems. Assuming that the shift of the absolute phase is unimportant, the solution of the phase-only configuration (with only one liquid crystal array) is the following:

$$E_{out} = H(\phi)E_{in} = \begin{pmatrix} \exp(i\phi) \\ 0 \end{pmatrix} \tag{3.107}$$

The solution of the phase and amplitude configuration takes a few more steps:

$$E_{out} = P_x R\left(\frac{\pi}{4}\right) H(\phi_2) R\left(-\frac{\pi}{2}\right) H(\phi_1) E_{in} \tag{3.108}$$

Considering the matrix definitions, after calculation one arrives to the following result:

$$E_{out} = \exp\left(i\left[\phi_1 + \phi_2\right]/2\right)\begin{pmatrix} \cos\left(\left[\phi_1 - \phi_2\right]\right)/2 \\ 0 \end{pmatrix} E_{in} \tag{3.109}$$

The amplitude modulation applied to the output field is therefore determined by the difference between ϕ_1 and ϕ_2, while the phase modulation is determined by their sum.

CHAPTER 3

OVERVIEW OF EXPERIMENTAL METHODS

3.1 Pulse compression methods

In the femtosecond regime pulses easily get chirped going through the dispersive optics on the optical table. Group delay dispersion (GDD) is an ultrafast phenomenon that can be ubiquitous, and often irritating, in ultrafast laser labs. When ultrashort pulses propagate through dispersive media, their frequency components emerge at different times due to GDD, causing the resulting pulse to be chirped and stretched and reducing the pulse's peak power. This effect can be compensated using a pulse compressor, which can introduce negative GDD.

Pulse compression, basically means to compress a pulse to a shorter duration. In our experiment in particular a 10 cm long Single Mode Fibre was causing a non-negligent dispersion to the pulse that we needed to compensate. We used a double prism configuration although there are a number of options each one appropriate for different cases of diverse priorities.

Multitudinous methods, devices and materials have been developed in order to compress laser pulses to their shortest possible lengths and to check whether or not the pulses are properly compressed. Indeed, ample is the pool of options to choose from, if you are in need for your ultrafast newly built laser lab. These can be distinguished by their efficiency, the maximum path length difference between frequency components that can be induced and if they are capable of negative or positive dispersion. Any of these can be the criteria upon which one can select the right combination of optics for their particular setup [63,64].

Stretchers and compressors are characterized by their dispersion. With *negative dispersion*, light with higher frequencies (shorter wavelengths) takes less time to travel through the device than light with lower frequencies (longer wavelengths). With *positive dispersion*, it is the other way around.

With regard to the vast options there are for pulse compression, the most popular ones are based on angular dispersion and consist of pairs of gratings or prisms. Martinez, et.al. [65-67] showed that angular dispersion, regardless of its sign, yields negative GDD. Therefore, simply propagating the pulse through a prism or diffracting it off a grating yields negative GDD, whose magnitude depends on the propagation distance. But the output pulse has inconvenient angular and spatial dispersion. Adding a second identical prism, anti-parallel to the first one, eliminates the angular dispersion from the output beam. Eliminating the spatial dispersion requires propagation through an additional identical pair of prisms. As a result, the four-prism pulse compressor can compensate material dispersion and also reconstruct the beam. It also compensates for the pulse-front tilt that it introduces in the process.

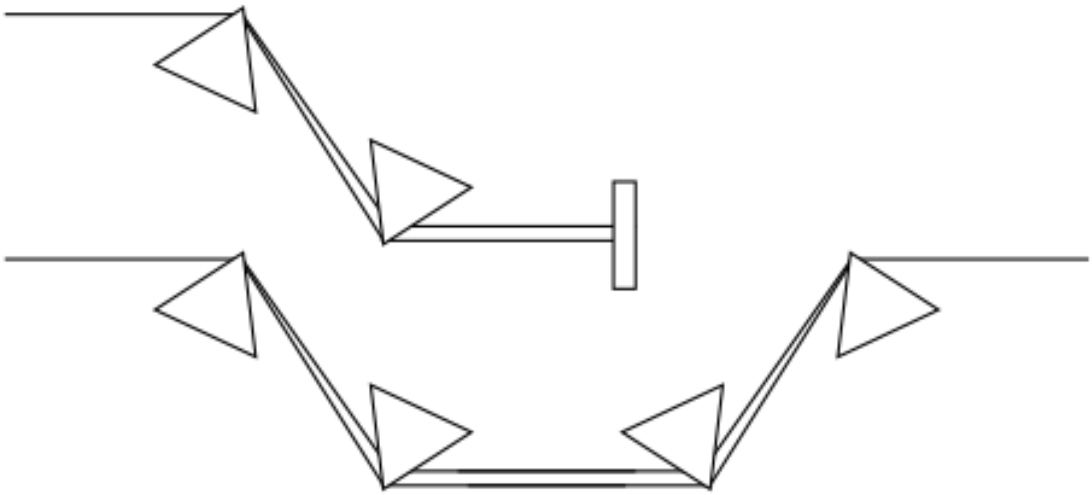

Figure 3.1 Two and four prism pulse compressor, used to produce negative dispersion. In the first case a mirror reflects the light back in order to form a more compact and easier to tune configuration.

Unfortunately, the pulse compressor is as unwieldy as it is essential. While the GDD can be conveniently fine-tuned by translating one of the prisms into or out of the beam, to vary the GDD over a wider range of values, the separations between the first and second prisms and the third and fourth prisms must be varied (and maintained precisely equal), which involves several alignment parameters and an inconvenient set up. Also, pulse compressors have stringent alignment conditions, and, when not perfectly aligned, they yield an output pulse with residual amounts of spatio-temporal distortions including angular dispersion, pulse-front tilt, spatial chirp, and one-dimensional beam magnification or demagnification (yielding an elliptical output beam) [71,72]. Because pulse compressors must generate massive amounts of these distortions in order to operate, even residual amounts of them can be a serious problem. It is also very inconvenient to tune in wavelength: if the input wavelength changes, all the prisms must be carefully rotated by the same amount, or else all of the above distortions occur. Finally, the device is bulky. To obtain the desired amount of negative GDD, the prism or grating separations can be quite large.

The prism pulse compressor is an indispensable tool in essentially all ultrafast labs. It has been used in many ultrashort pulse applications, for over two decades and it has been simplified to two prisms through the use of a mirror after the second prism, which made it much more practical for use.

The two-prism design is more compact and slightly easier to tune (only two prisms must be rotated by precisely the same amounts) –the main reason for which it was initially chosen for our setup. We will be seeing this again later in Chapter 4, together along with its main drawbacks, because let's call a spade a spade, it inherits most of the unwieldiness and propensity for spatio-temporal distortions of the four-prism design.

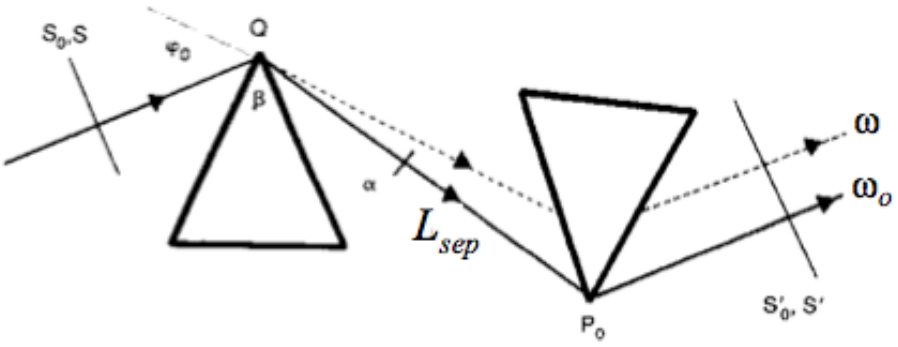

$$\left.\frac{d^2\varphi}{d\omega^2}\right|_{\omega_0} \approx -4L_{sep}\frac{\lambda_0^3}{2\pi c^2}\left(\left.\frac{dn}{d\lambda}\right|_{\lambda_0}\right)^2 + L_{prism}\frac{\lambda_0^3}{2\pi c^2}\left.\frac{d^2n}{d\lambda^2}\right|_{\lambda_0} \tag{3.1}$$

Figure 3.2 Two prism compressor, for negative or positive dispersion. This can be tuned by varying L_{sep} or L_{prism} (the additional length the beam crosses inside the prism).

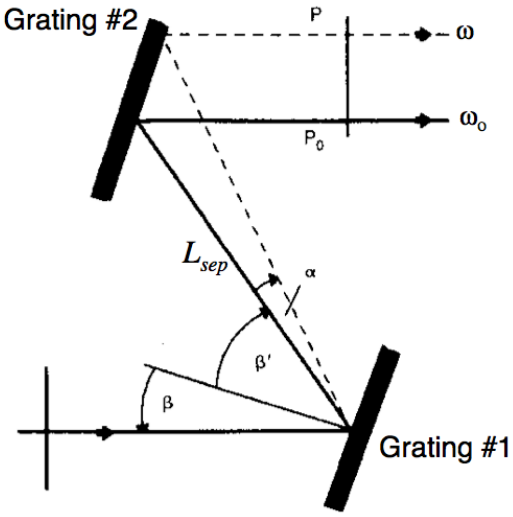

$$\left.\frac{d^2\varphi}{d\omega^2}\right|_{\omega_0} \approx -\frac{\lambda_0^3}{2\pi c^2 d^2}\frac{L_{sep}}{\cos^2(\beta')} \tag{3.2}$$

Figure 3.3 Schematic layout of a grating-based compressor of grating spacing d, with negative dispersion. As in the prism pulse compressor, the larger L_{sep} is the larger the negative GDD.

It is also fair to make a comparison with the most common pulse compressor based on gratings, which can easily create a much larger negative dispersion than a prism compressor. However, a grating compressor has losses of at least 30% due to higher-order diffraction and absorption losses in the metallic coating of the gratings. A prism compressor with an appropriate anti-reflection coating can have less than 2% loss, which makes it a feasible option inside a laser cavity. This difference in effective losses between the two, resulted important for the choice of prisms rather than gratings in the initial scheme of the experimental setup for dispersion compensation of a 10 cm long Single Mode Fibre, as we will see again in Chapter 4.

The "zero-dispersion pulse compressor"

The discourse is about an apparatus that makes possible the synthesis of femtosecond optical waveforms with precisely controlled shapes. The apparatus consists of a pair of diffraction gratings and lenses as shown in the image below.

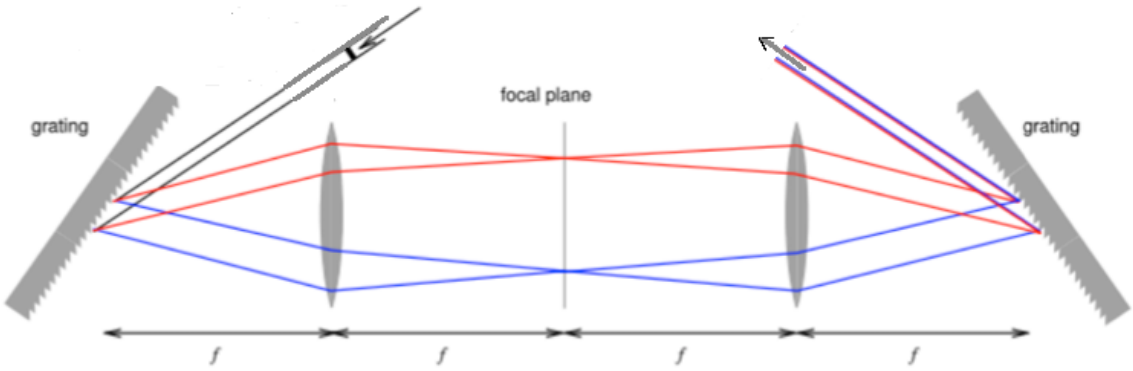

Figure 3.4 Zero-dispersion pulse compressor composed by a pair of gratings and a pair of lenses placed in a 4-f line configuration. The focal plane between the two lenses is the Fourier transform plane.

The first grating and lens spatially disperse the individual optical frequency components contained within an incident pulse. The second lens and grating are placed in that order and with a distance 2f and 3f from the first lens respectively. All the frequencies are recombined spatially in a single collimated beam by the 2nd lens and grating. The focal plane between the two lenses is called the Fourier transform plane, and it is where the optical spectral components obtain the maximal spatial separation between them. This way, when a modulation mask is placed at the focal plane it is possible to apply a different modulation to each component. If the setup is aligned perfectly in the 4f configuration, the output pulse should be identical to the input pulse if no modulation device is placed in the Fourier transform plane. In other words the grating and lens system would be free of dispersion in such configuration, hence the name "zero-dispersion pulse compressor". The first lens performs a spatial Fourier transform between the plane of the first grating and the masking plane and the second lens perform a second Fourier transform from the masking plane to the plane of the second grating. The total effect of these two consecutive Fourier transforms is that the input pulse is unchanged in travelling through the system if no pulse shaping mask is present. Note that, if the output grating is moved closer or further from the second lens, the optical setup can provide a positive or negative group velocity dispersion of the output pulse, respectively.

In our experiments we first used a twin prism compressor setup as it was able to provide a substantial negative dispersion while maintaining the power level of the beam intact. We later replaced the twin prism compressor with a full shaping system composed of a zero-dispersion compressor and modulation mask. This gave us the possibility to achieve a programmable control of both the spectral amplitude and phase of our pulses. With use of a computer we could thus precisely generate arbitrarily complex pulse shapes.

For the zero-dispersion pulse compressor we used two holographic gratings and two cylindrical lenses, and it was used in combination to a liquid crystal Spatial Light Modulator device (SLM) placed in the Fourier plane. This was a significant upgrade to the capacity of the setup, as we will see in Chapter 4. It is necessary first to present the device and the calibration procedure we followed.

3.2 Programmable pulse shaping with use of Spatial Light Modulators

Our pulse shaping setup consists of a liquid crystal SLM device placed in the Fourier plane of a zero-dispersion pulse compressor setup, in order to provide modulation on each individual frequency component of a broadband pulse [63]. It can (depending on the particular model) perform both amplitude and phase modulation separately on each spectral component contained in an ultrashort pulse, easily and accessibly through a simple computer program.

However, for one to appreciate this brilliant new device I need to mention that this was not the first available masking technology in the market, but early femtosecond shaping experiments had to settle for fixed spatial masks produced using microlithography [64]. Even though the pulse shaping quality that prefabricated masks provided was admittedly good, their limitations of not easily giving continuous phase variations and that a new mask had to be fabricated for each experiment, along with the inability to reprogram pulse shapes in real time, and the difficulty of achieving gray-level phase control, demanded that the scientific community made a leap in a direction for a better technology.

Below, I will be describing the procedure of preparing a pulse shaping setup for an experiment, starting from the choice of optics for the zero-dispersion compressor, explanation of the function of an SLM and how to calibrate it. In the last chapter of the thesis, you can find a description of the alignment procedure of the pulse shaping setup and how we managed to integrate it in the experiment.

3.2.1 How to choose the correct optics for your "zero-dispersion compressor"

In order to provide proper pulse shaping of either phase or amplitude, it is necessary first to disperse the various frequency components spatially. This way each pixel of the liquid crystal mask is responsible for the shaping of the particular component impinging on it. In order to do that, building the "zero-dispersion pulse compressor or stretcher" is a first essential step of the procedure.

Depending on the particular requisites for each different experiment, that is in practical terms how much spatial dispersion would be necessary, what is the bandwidth available, or how much space there would be for use on the optical table to setup the apparatus, one needs to make correct choice of the optics. The dispersions translates into the type and groove density for the gratings and the type and focal length for the lenses, in terms of the physical parameters of the optics, that once they are chosen and combined the amount of spatial dispersion of the broadband pulse is fixed.

Diffraction gratings, rather than prisms, are generally used in dispersing laser pulses of modest bandwidths since prisms are typically unable to provide sufficient spectral dispersion without introducing unwanted aberrations to the beam. As already noted in chapter 2, prisms are a wiser choice in cases where the overall efficiency is more important. Holographic gratings, rather than ruled ones, are preferred since they lack the defects, such as ghosts, that

ruled gratings are unable to avoid. With a holographic grating, the best efficiency can be achieved when the incident light is polarized perpendicular to the grating grooves. In order to have the light dispersed horizontally within the plane of the laser table, which is the usual case, the grating grooves need to be vertically oriented to disperse a horizontally polarized input laser pulse. The grating is chosen to have a high enough groove density such that when used near the Littrow angle, mostly one diffraction order (in addition to the zero order beam) is produced. This is useful since it means the output light is divided amongst the fewest possible output beams. A slightly higher or lower groove density would also work, and may be desirable depending on other design considerations (such as the size of the LC SLM).

Given the angular dispersion provided by the diffraction grating, the lens focal length should be determined based on the desired dispersion of the laser spectral components. When the laser pulses are very short, it may be best to use reflective optics in order to avoid material dispersion due to propagation through glass. In such cases, spherical mirrors (designed for near-normal incidence) are most often used, but the design considerations are similar. Assuming a Gaussian input laser spectrum, the full-width at half maximum (FWHM) of the laser spectrum should be fit to about one third of the width of the LC SLM in order to reach a compromise between avoiding clipping of the laser spectrum at the low and high frequency edges of the LC SLM and achieving the lowest $\Delta\nu$ per pixel (i.e. a large time window). Since an 80 fs laser pulse centred at 800 nm has a spectral bandwidth of about 35 THz (approximately 12 nm), the lens should be chosen such that approximately 105 THz span the LC SLM. We used a 7.5 cm lens with the input beam at 55.5° relative to the surface normal such that 91.5 THz spanned the LC SLM (128 pixels, with 100 μm/pixel) and holographic gratings of d=1/1800 mm^{-1}.

Once the grating and lens have been chosen, the dispersion is fixed, although the spectral resolution is not. This is because the spectral resolution is also a

function of the input beam diameter. Use of a large input beam increases the spectral resolution relative to a small input beam, since the spectral resolution is determined by the spot size of a given spectral component.

By spectral resolution we imply the amount of λ impinging on a single pixel. So this also depends on the spot size of each individual component:

$$\Delta x_0 = 2\ln(2)\frac{\cos\theta_i}{\cos\theta_d}\frac{f\lambda_0}{\pi\Delta x_{in}} \tag{3.3}$$

where Δx_{in} is the width of the input beam, θ_i the angle of incidence and θ_d the angle of diffraction (see image below).

Generally, it is best to use an input beam size, which yields a spot size (FWHM) at the focal plane of approximately one LC SLM pixel width. In our case the input beam FWHM was 5 mm.

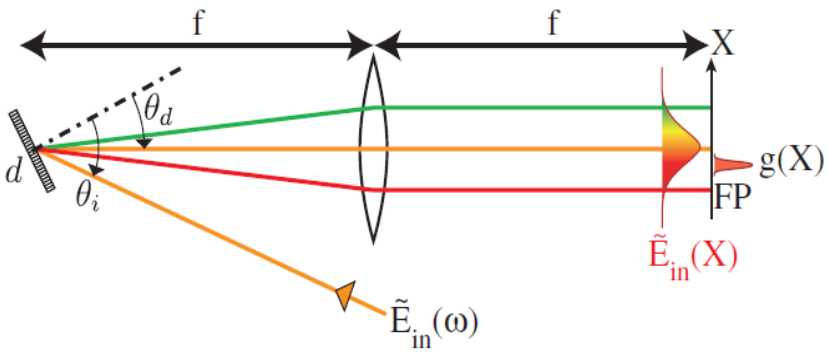

Figure 3.5 Half a 4f line of a zero-dispersion pulse compressor: The Fourier plane is situated in the back focal plane of the lens, f is the focal length, $g(X)$ is the spatial extension of a given frequency component, θ_i is the angle of incidence, d is the grating period, θ_d is the angle of diffraction [59].

$$\lambda = d\left(\sin\theta_i + \sin\theta_d\right) \tag{3.4}$$

$$x = f\tan\left[\theta_d(\lambda) - \theta_d(\lambda_0)\right] \tag{3.5}$$

$$x_k = a\omega_k, \text{ where } a = \frac{\lambda_0^2 f}{2\pi c d\cos\theta_d} \tag{3.6}$$

From Equation (3.5), if one sets $x = L/2$, where L is the length of the SLM window (in our case L=12.8 mm), it is then possible to calculate the angle of dispersion that would make the most of the SLM capacity, for a specific focal length and then from that recover how much would be the necessary groove density in order to choose the grating. The calculation can be reversed for a given groove density of a grating looking for the right lens f to have the desired dispersion.

3.2.3 Spatial Light Modulator

The Spatial Light Modulator, is a computer controlled device, able to provide spatially varying modulation on a beam of light. We have already reviewed the function of an SLM device and its mathematical representation in chapter 2.4 Here I will be focusing on the experimental point of view of the device, that is a description of its manufacture, in order to better understand how it works, with a description of calibration of the device to follow.

Each pixel of a liquid crystal spatial light modulator (LC-SLM) [57], is a programmable waveplate controlled by voltage. A LC-SLM consists of a thin layer of nematic liquid crystal placed between two glass substrates. One substrate is covered with transparent ITO (indium tin oxide) electrodes, which allow the application of independent voltages to each pixel. The nematic liquid crystals are small rods that are oriented parallel to the substrate when no voltage is applied. Their anchorage direction is fixed by brushing off the electrodes. When a voltage is applied, the nematic molecules tend to align along the field. This modifies the birefringence of the medium, leading to a modification of the optical path for light polarized along the anchorage direction.

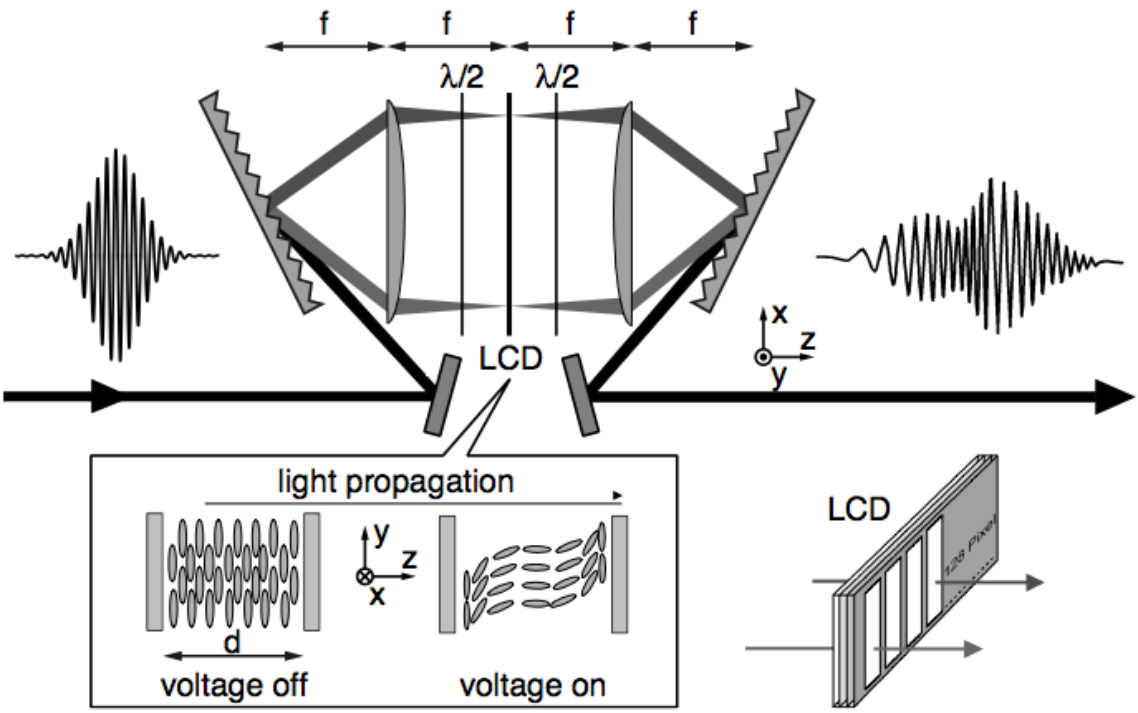

Figure 3.6 Femtosecond pulse shaper. A zero-dispersion compressor in 4f configuration contains a liquid-crystal (LC) spatial light modulator in its Fourier plane. By adjusting the voltages of the individual LC pixels, the liquid-crystal molecules reorient themselves partially along the direction of the electric field. This leads to a change in refractive index and therefore to a phase modulation which can be independently controlled for the different wavelength components. The half-wave plates ($\lambda/2$) are used to rotate the linear input polarization from x to y and back to x [68].

To achieve amplitude and phase shaping, two spatial light modulators are needed with the anchorage direction at +45◦ and −45◦ with respect to the horizontal axis. By placing horizontal polarizers at both the input and output of the 4f - line, the complex transfer function of one particular pixel k can be written as:

$$H_k = \exp\left(i\frac{\phi_1(\omega_k)+\phi_2(\omega_k)}{2} \right)\cos\left(\frac{\phi_1(\omega_k)-\phi_2(\omega_k)}{2} \right) \tag{3.7}$$

where ω_k is the frequency impinging on pixel k, ϕ_1 and ϕ_2 correspond respectively to the phase introduced by the first and second LC-SLM.

Our device is a commercially available liquid crystal from Cri, Model: SLM – 128-D-VM [69], and it provides independent control of each element in a linear array of 128 pixels, in the visible range of wavelengths (VM). The arrays are 5 mm high, and the pitch is 100 μm, resulting in total array apertures of 12.8 mm.

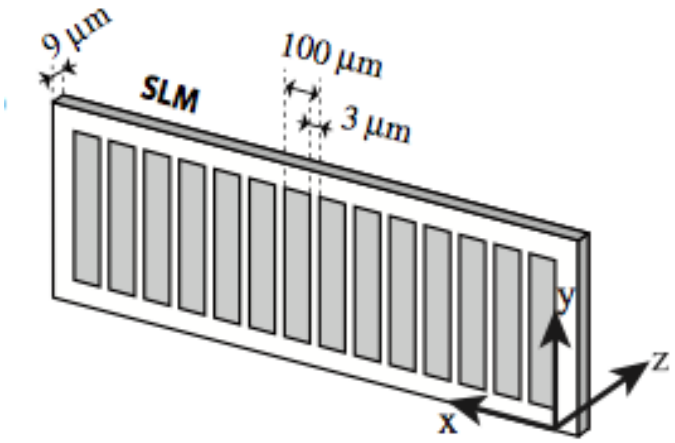

Figure 3.7 Schematic diagram of a 128-element (pixels) liquid crystal phase modulator array. Pixel pitch is 100 μm, interpixel gap is 3 μm, pixel height is 5 mm and thickness is 9 μm.

It is a dual-array modulator - consists of two precisely aligned modulators, providing a unique and convenient method for simultaneous modulation of both phase and amplitude at each pixel. The dual mask configuration can operate either as a phase and amplitude of specifically polarized incident light or as simply a phase modulator of arbitrarily polarized incident light. The optics the device is equipped with, are optimized to work in the following wavelength range: 488 nm to 900 nm. It is currently in the transmissive mode, with two polarizers at the input and output window of the crystal allowing only horizontally polarized light to pass. (It gives also the possibility to function in the reflective mode as well by replacing the output polarizer with a mirror and therefore providing double modulation). It communicates via a USB interface, and can be controlled with a set of ASCII

commands, software drivers for C++, MATLAB and LabVIEW or Windows graphical user interface.

The SLM maintains a table of drive levels in its memory, which specify the drive at each pixel in the liquid crystal array. The drive level is a number from 0 to 4095, resulting in a drive signal of

$$V_i = V_{ref} \times D_i / 4095 \tag{3.8}$$

where V_i is the voltage at pixel element i, and D_i is the digital drive level corresponding to that element and V_{ref} is the reference voltage, 10.000 V.

3.2.3 Calibrating the pulse shaping setup

1st calibration: Phase vs. Voltage

The first step is the careful alignment of the 4f-line of our dispersive optics, with an optimized control of the input/output condition of our pulse duration (see chapter 4.2 for details). Thereupon, one can proceed to the second important step of the preparation of the setup before inserting it in the experiment, which would be the calibration of the SLM.

The phase response of each SLM, is not precisely known, so one needs to calibrate the introduced phase $\phi(\omega,U)$ as a function of both voltage U and frequency ω [59,63,64]. In principle each pixel should be calibrated independently and at the specific frequency that impinges on it. In practice however, the process is much simpler. First, the LC-SLM is usually homogenous enough to use a unique voltage calibration for all the pixels. Second, from the voltage calibration at one specific frequency ω_{cal}, we can derive the voltage calibration for any frequency by a simple multiplication to a constant taken from the diagram in the user manual, implicating the

modulation produced at different wavelengths by the liquid crystal (that is the change in index of refraction).

For a frequency ω, the pixel acts as a waveplate whose phase ϕ is given by

$$\phi(\omega,U)=\frac{\omega\Delta n(\omega,U)L}{c} \tag{3.9}$$

where $\Delta n(\omega,U)$ is the index difference between the slow and the fast axes (birefringence), U is the applied voltage and L is the thickness of the liquid crystal layer.

The usual way to calibrate the phase is to place the mask between two horizontal polarisers (in our case they are included inside the device), illuminate with the monochromatic HeNe laser at $\lambda = 633$ nm, focus the beam at a single pixel and measure the transmitted intensity I_{cal} as a function of the voltage U applied to all the pixels of the mask.

Another method we tried was with the pulsed femtosecond laser with $\lambda = 800$ nm and $\Delta\lambda = 12$ nm with use of a spectrometer. We apply the voltage to all the pixels increasing step by step. Later, we compare the relative intensity between the zero level and the level in question for all the frequencies at the same time (for normalisation). The downside of this method is the large fluctuation of the intensity levels of the spectrum due to limited resolution of the spectrometer. This significantly decreased with the use of a round paper rotating with high frequency in front of the multimode fibre of our spectrometer, however not enough as the fluctuation was still much higher than the actual change in the intensity caused by the difference in voltage.

Following the same logic as before, we also tried to do the same calibration with the pulsed femtosecond laser but only using the power meter instead of the spectrometer, that is connected to a GPIB interface that sends the data to the computer. The calibration was done in an automated way with use of a

program registering the change of voltage with the transmitted power and saving all the data directly to be elaborated. The procedure is repeated for both masks of the SLM, after what the data are plotted first to obtain an intensity (transmission) vs. levels (voltage) curve, which is then normalised. Following that, the phase values are retrieved from the normalised intensity as the sinusoidal form of the curve reveals the corresponding phase change for each level (voltage). Their relationship is represented by the function of the general form below:

$$\bar{I}(\omega) = \sin^2\left[\frac{\phi(\omega,U)}{2}\right] = \frac{1}{2}\left[1-\cos\left(\phi(\omega,U)\right)\right] \tag{3.10}$$

Therefore, the phase versus levels curve is obtained by inverting the above function, and plotting the phase $\phi(\omega,U)$ as a function of the normalised Intensity $\bar{I}(\omega)$.

The exact function that describes the phase ϕ -levels(voltage U) curve is unknown and in order to have a fit more precise, closer to the experimental data, we selected the part of the curve that is of our interest (for phase change from 0 to 2π) and plotted with a linear function.

Furthermore, from the voltage calibration at the specific frequency ω_{cal}, one can derive the voltage calibration for any frequency:

$$\phi(\omega,U) = \phi(\omega_{cal},U)\frac{\omega}{\omega_{cal}}\frac{\Delta n(\omega,0)}{\Delta n(\omega_{cal},0)} \tag{3.11}$$

This is all the information one needs to be able to programme the SLM, together with the second calibration (pixel number to wavelength).

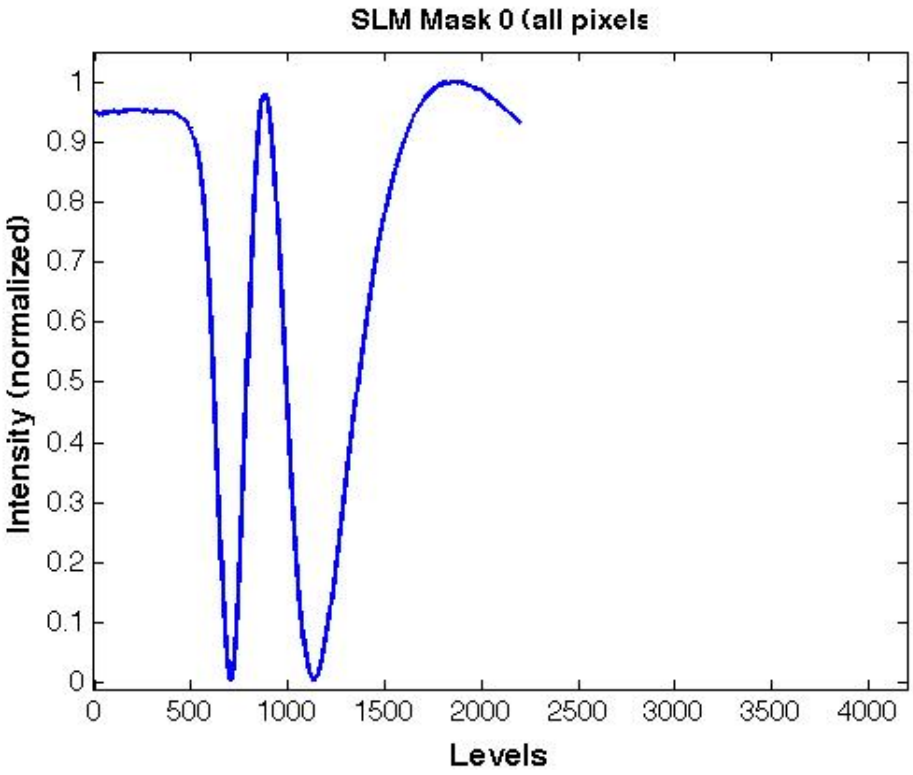

Figure 3.8 Experimentally retrieved curve for normalised Intensity vs. Levels, for SLM calibration

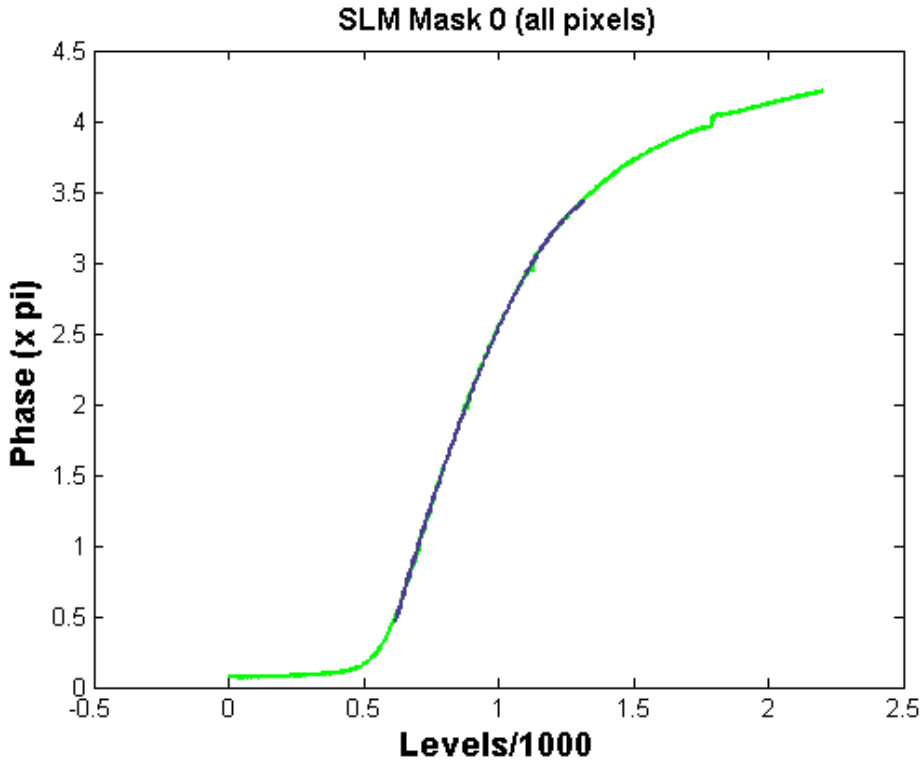

Figure 3.9 Experimentally retrieved curve for Phase vs. Levels, for SLM calibration

2nd calibration: Wavelength vs. Pixel number

The second calibration, i.e. mapping the different wavelengths vs. pixel numbers is a much simpler one. Practically we measure the spectrum of the output beam using a well-calibrated spectrometer. To pair the frequency ω_k with the pixel *k*, we programme a zero transmission at the pixel *k* or a π-jump between the pixels *k* and *k+1*. This leads to a hole in the spectrum that is easy to spot. Otherwise, we alternatively program zero or maximum transmission for adjacent pixels. In both cases, each different pixel number is thus assigned a specific wavelength and by plotting one against the other, we find a remarkably linear behaviour. Of course, this calibration is required each time the alignment of the 4f-line is modified.

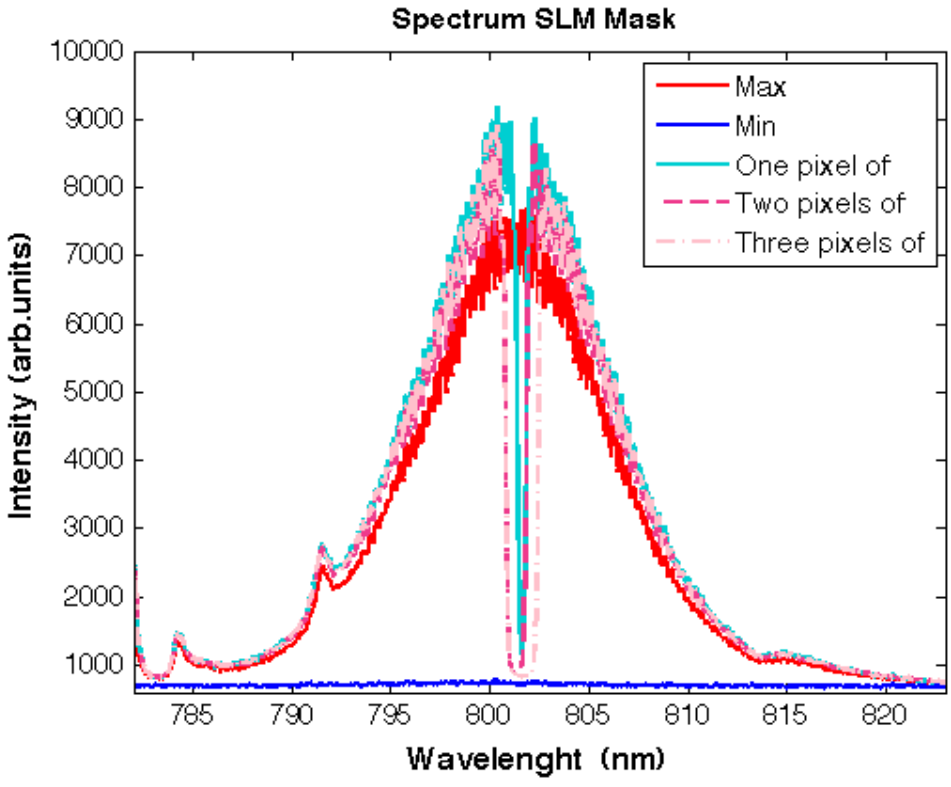

Figure 3.10 Spectrum at the exit of the pulse shaper with pi (off) phase in 1, 2 and 3 pixels, for the SLM calibration pixel number vs. wavelength.

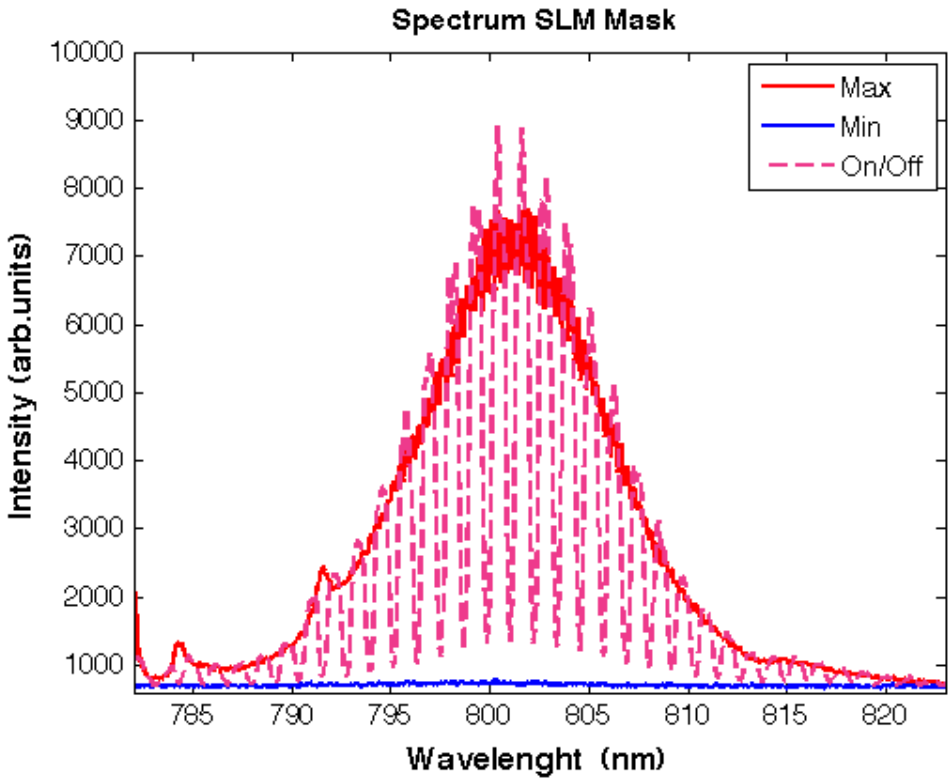

Figure 3.11 Spectrum at the exit of the pulse shaper with alternating 0(on) and pi (off) phase pixels, for the SLM calibration pixel number vs. wavelength

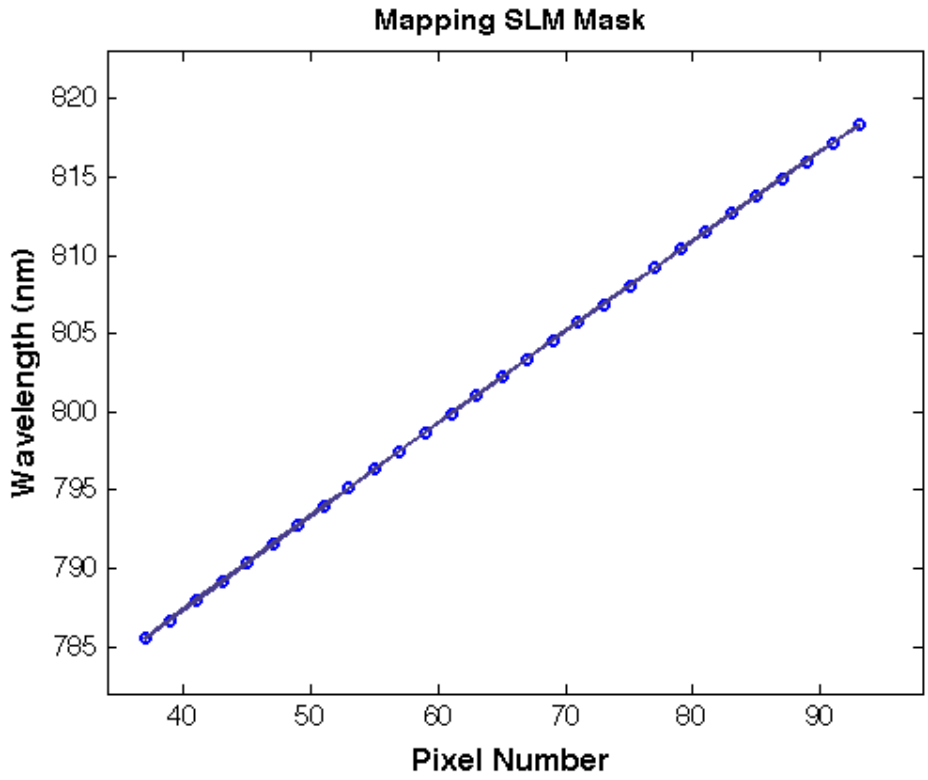

Figure 3.12 Wavelength vs. Pixel number experimentally retrieved linear curve from calibration of the Spatial Light Modulator

3.3 Pulse Diagnostics

After the advancement of lasers emitting ultrashort pulses, immediately the need was created for another detection technique. Science has currently arrived at the record of 80 attoseconds [70], the shortest laser pulse duration ever created. Needless to emphasize the importance of precise knowledge of the pulse properties for experiments and for further progress in the ultrashort field, and for the aim of decreasing even further the durations of creation, control and measurement of laser pulses.

That is the story of how the FROG has been introduced, as an innovative technique, designed for the complete characterisation of ultrashort pulses. Of course, here I am not referring to the measly green four-legged we all know by that name, and even though the trace may resemble as such, what FROG really stands for, is Frequency Resolved Optical Gating [73].

Having introduced the representation of our pulse both in frequency and time domain in chapter 2.1, that are equivalent, we are in a position to say what we mean by "complete" characterisation of the pulse: our desire is to measure $E(t)$ [or $\tilde{E}(\omega)$] completely, that is to know both the intensity and phase profile of the pulse in either frequency or time domain.

How hard is it or has it been to measure both intensity and phase in either temporal or frequency domain? The answer is that it has been impossible with conventional techniques. More specifically, with autocorrelation devices we obtain the intensity $I(t)$ but no information about the phase is possible. Below, I will be discussing further this technique and make a comparison to the FROG.

3.3.1 Previous techniques – The Autocorrelator

Before the appearance of the time-frequency methods, what was really the workhorse in ultrafast optics was the Autocorrelation and Spectrometer, the only available technology before the 80's. The spectrometer operates in the frequency domain and measures the spectrum $I(\omega)$ but it is unable to obtain information on the spectral phase. On the contrary in the time domain, the problem was that these pulses are much shorter than the resolution of the available measuring devices and so it made it impossible to measure intensity $I(t)$ or temporal phase $\varphi(t)$.

The solution to this problem came when someone had the clever idea, to use no other but the pulse itself, since no event shorter than the pulses in question was available. Autocorrelators first split the pulse into two replicas, after what one of the two paths is variably delayed with respect to the other, and spatially overlapping the two pulses in some instantaneously responding nonlinear-optical medium, such as a second-harmonic-generation (SHG) crystal.

The intensity of the SHG light produced from the crystal is proportional to the product of the intensities of the two input pulses and therefore depends on the relative delay between the two pulses. Second-harmonic light is only generated when the two pulse replicas overlap in time; from this it is possible to obtain a measure of the pulse length.

The SHG signal light of twice the frequency of the input light with a field envelope given by:

$$E_{SHG}(t,\tau) \propto E(t)E(t-\tau) \tag{3.12}$$

where τ is the delay.

This field has an intensity that's proportional to the product of the intensities of the two input pulses:

$$I_{SHG}(t,\tau) \propto I(t)I(t-\tau) \tag{3.13}$$

Detectors are too slow to resolve this beam in time, so they'll measure:

$$A(\tau)^2 = \int_{-\infty}^{\infty} I(t)I(t-\tau)dt \tag{3.14}$$

This is the intensity autocorrelation. The superscript (2) implies that it's a second-order autocorrelation; third-order autocorrelations are possible, too.

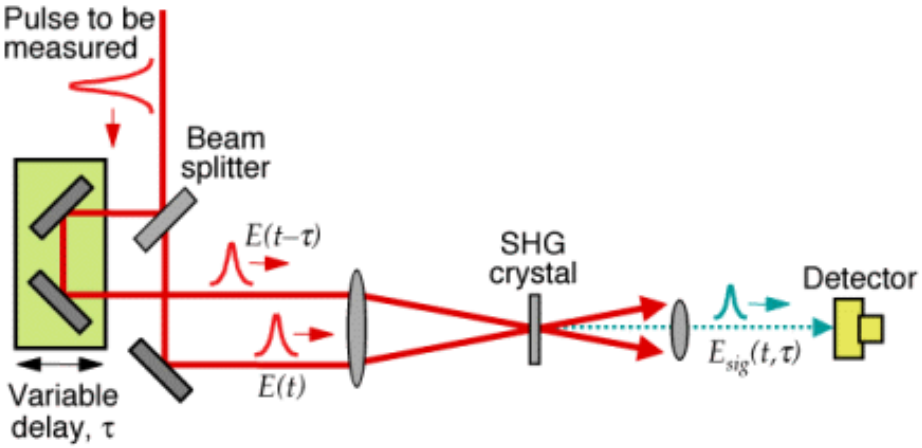

Figure 3.13 Experimental layout for an intensity autocorrelator using second-harmonic generation. A pulse is split into two, one is variably delayed with respect to the other, and the two pulses are overlapped in an SHG crystal. The SHG pulse energy is measured vs. delay, yielding the autocorrelation trace. Other nonlinear-optical effects, such as two-photon fluorescence and two-photon absorption can also yield the autocorrelation, using similar beam geometries.

Unfortunately, this measurement yields a smeared out version of $I(t)$, and it often hides structure. In addition, in order to obtain as little information as the pulse length, a guess must be made as to the pulse shape, yielding a multiplicative factor that relates the autocorrelation full width at half-maximum to that of the pulse $I(t)$. This factor varies significantly for different common shapes and this has resulted in an unfortunate temptation

to choose an “optimistic” pulse shape, such as $\mathrm{sec}h^2(t)$, which yields a large multiplicative factor and hence a shorter pulse length for a given measured autocorrelation width.

In the case of a measurement of more complicated pulses the autocorrelation's tendency to wash out structure in the intensity is most evident. In fact, for complex pulses, it can be shown that, as the intensity increases in complexity, the autocorrelation actually becomes simpler and approaches a simple shape of a narrow spike on a pedestal, independent of the intensity structure.
The resulting conclusion is that autocorrelation trace is able to only yield rough measures of intensity autocorrelation, without saying anything really of the actual intensity structure or anything at all of the spectrum.

On the other hand, there is the "Interferometric Autocorrelation," which involves placing an SHG crystal at the output of a Michelson interferometer, yielding some information about the pulse phase. This certainly constitutes an improvement with respect to conventional AC techniques but there is no way to extract the full pulse intensity and phase from it, and, worse, very different pulses (even pulses with very different pulse lengths) can have very similar interferometric autocorrelations.

Thus, a pulse intensity shape and phase must typically be assumed when using any type of autocorrelation. And the resulting pulse length will depend sensitively on the shape chosen. Worse, in view of these issues, it generally isn't possible to sense from an autocorrelation when other pulse distortions (such as spatio-temporal distortions like spatial chirp or pulse-front tilt) or systematic errors are present. Additionally the presence of systematic error -

due to misalignment for example- may be present and judgement of the universality of the measurement is difficult.
As a result, autocorrelation is no longer an acceptable measure of most ultrashort pulses.

3.3.2 The F.R.O.G.

It can be shown that the problem of retrieving the pulse intensity from the intensity autocorrelation is equivalent to a mathematical problem called the one-dimensional phase-retrieval problem, which is the attempt to retrieve the Fourier-transform phase for a function when only the Fourier-transform magnitude is available. This problem is unsolvable because typically many solutions ("ambiguities") exist, and it isn't possible to determine which is the correct one. The solution had to come from mathematics: one dimensional phase retrieval fails because polynomials of one variable can always be factored. But two-dimensional phase retrieval succeeds because polynomials of two variables cannot. This is exactly the logic behind the operation of the FROG: the mathematics that it uses yields a well-behaved and well-posed two-dimensional phase-retrieval problem, whereas traditional autocorrelation involves a highly ill-posed one-dimensional phase-retrieval problem. This measurement problem was solved in 1991 using a technique called frequency resolved optical gating, which generates a spectrogram of the pulse by measuring the autocorrelator-generated second-harmonic spectrum as a function of the pulse delay [73].

From a practical point of view, FROG does not require a shorter event than the pulse because short-time behaviour is resolved in the frequency domain through FROG's spectral measurements.

Frequency-Resolved Optical Gating (FROG) involves operating in a hybrid domain: the time-frequency domain. Measurements in the time-frequency domain involve both temporal and frequency resolution simultaneously. A well-known example of such a measurement is the musical score, which is a plot of a sound wave's short-time spectrum vs. time. Specifically, this involves breaking the sound wave up into short pieces and plotting each piece's spectrum (vertically) as a function of time (horizontally). So the musical score is a function of time as well as frequency, it graphically shows the waveform's instantaneous frequency vs. time, and, even better, it has additional information on the top indicating the approximate intensity vs. time.

A mathematically rigorous version of the musical score is the spectrogram:

$$\Sigma_g(\omega,\tau)=\left|\int_{-\infty}^{\infty}E(T)g(t-\tau)\exp(-i\omega t)dt\right|^2 \tag{3.15}$$

where $g(t-\tau)$ is a variable-delay gate function. How do we measure a spectrogram of light? We use FROG!

It's easy to make FROG measurements of even the shortest pulses, and it robustly yields the complete intensity and phase vs. time. FROG can measure even complex pulses and it has been used to measure a wide range of pulses from the mid-IR to the extreme UV.

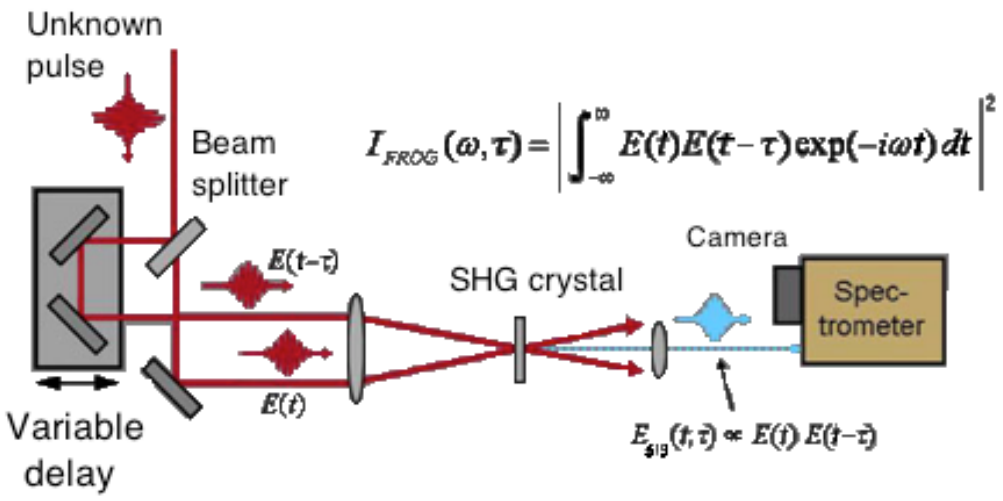

Figure 3.14 Experimental layout for a Frequency Resolved Optical Gating device, using second-harmonic generation. A pulse is split into two, one is variably delayed with respect to the other, and the two pulses are overlapped in an SHG crystal. Differently from the Autocorrelator, the SHG pulse energy is measured vs. delay and frequency, using a spectrometer as a detector. It yields the complete intensity and phase vs time, for even complex pulses and for even very short durations.

There are several types of FROG with different beam geometries and traces such as the polarization-gate FROG, the self-diffraction FROG, the transient grating FROG, the second harmonic generation frog, and the third harmonic generation FROG.

In our experiment we use a second-harmonic generation FROG that has the main advantage of its high sensitivity: it involves a second-order nonlinearity, while the other FROG variations use third-order optical nonlinearities, which are much weaker. As a result, for a given amount of input pulse energy, SHG FROG will yield more signal pulse energy.

The main disadvantages of SHG FROG are that unlike the previously mentioned third-order versions of FROG, it has an unintuitive trace that is

symmetrical with respect to delay, and as a result, it has an ambiguity in the direction of time. The pulse $E(t)$, and its time-reversed replica, $E(-t)$, both yield the same SHG FROG trace. Thus, when an SHG FROG trace is measured and the phase retrieval run on it, it's possible that the actual pulse is the time-reversed version of the retrieved pulse.

Perhaps the best feature of FROG is its over-determination of the pulse: it is a 2D array of points even though the pulse is only 1D. As a result, agreement between the measured and retrieved traces tells us that the measurement was made well and the pulses (if the measurement averaged over many of them) were stable.

3.3.3 FROG alignment and calibration

In our Lab we have a second-harmonic-generation based FROG device (FROG-Scan, MesaPhotonics [74]).

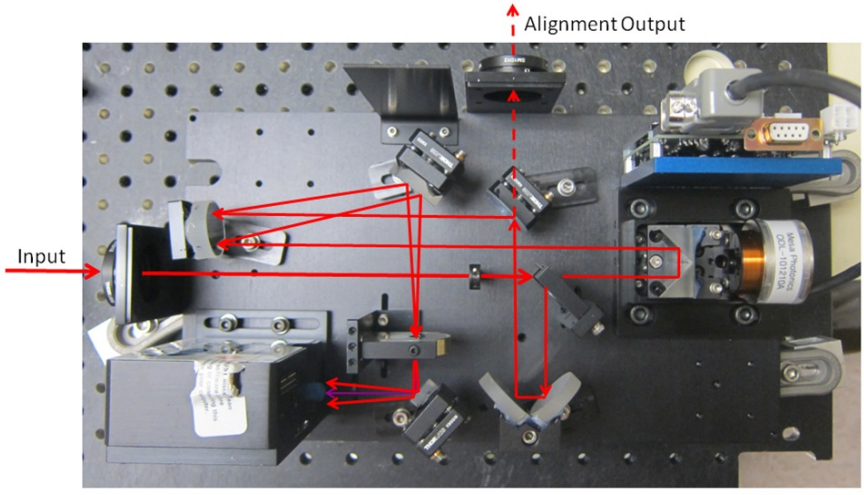

Figure 3.15 Beam diagram of FROG Scan. The input beam enters on the left though the external iris and passes to the beam splitter and the servo stage. The beam that does not hit the servo, hits another beam splitter that allows some of the beam to pass through a second alignment iris.

The first thing to do is making sure that the beam is aligned and that its polarisation is horizontal. The beam has to be perfectly centred in the two irises when they are closed. On the computer program VideoFROGScan, we subtract the background and check if there is a signal.

In order to see a FROG signal, both beams (the two output beams of the beam splitter) must hit the same point on the SHG crystal at the same time. The diffraction effect can be indicative of the spatial overlap and the temporal overlap optimisation can be done with the translation stage. In case there is no signal to begin with, one should increase the integration time, this way increasing the signal to noise ratio, and adjust very finely the beam crossing on the SHG crystal. It is easy to saturate the signal, so reducing the input power may be necessary.

Once this procedure is repeated sufficiently, one can start to scan the delay between the two pulses. The range of time delays and wavelengths can be adjusted and optimized for the measured FROG trace. By increasing the grid size, larger time bandwidth products can be accommodated. Changing the time spacing or using the scan range control, adjusts the time window. When the time window increases, the spectral window decreases. If the pulse is so chirped that the time window must be increased in order to capture the entire temporal part, the spectral portion of the FROG trace may be clipped, therefore the grid size will need to be increased. The general aim is to obtain a clear trace without warning messages.

The selection of the background subtraction settings can be critical. If too much background is present, retrievals will appear noisy. However, if too much background is removed, the pulses will not be measured correctly and unphysical time-bandwidth products can occur.

Also important in this respect is the integration time of the acquisition: using too short integration times can produce erroneous results due to the high levels of noise. To check this, I performed FROG measurements of beams with different chirp, for various integration times.

Below we see a graph of the second order coefficient b2 as a function of the integration time of the FROG, for a slightly chirped pulse. We observe that it converges to a steady value only for integration times longer than about 40000 ms.

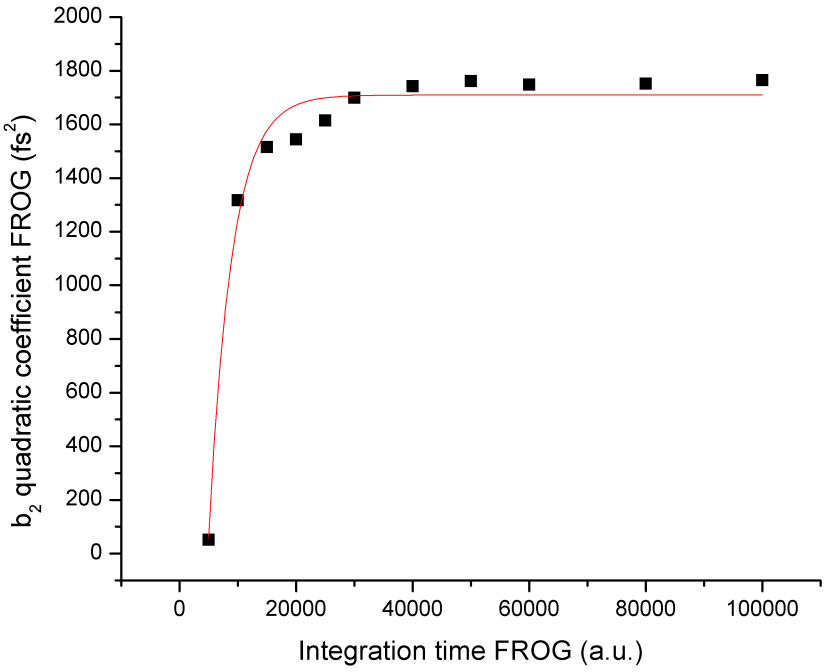

Figure 3.16 Experimentally retrieved curve for plotted quadratic coefficient with Integration time of FROG, for an unmodulated LO.

In the graph below (figure 3.17) we observe again the plotted dispersion coefficient b_2 as a function of the integration time of the FROG but now our

pulse is highly chirped thanks to our computer-controlled SLM device. Also in this case we observe that convergence to a reliable value is only obtained for sufficient integration times.

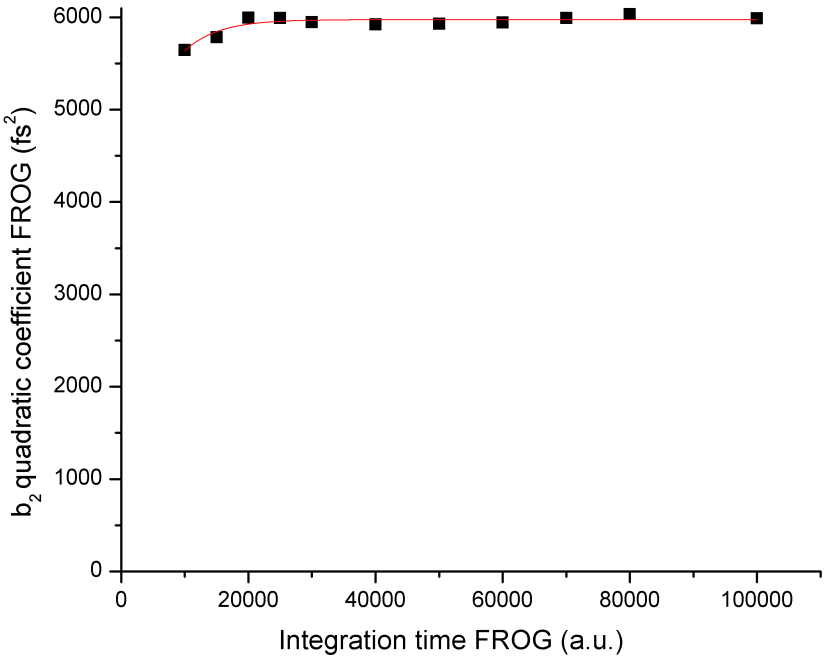

Figure 3.17 Experimentally retrieved curve for plotted quadratic coefficient with Integration time of FROG, for a dispersed LO.

CHAPTER 4

THE EXPERIMENT

Introduction

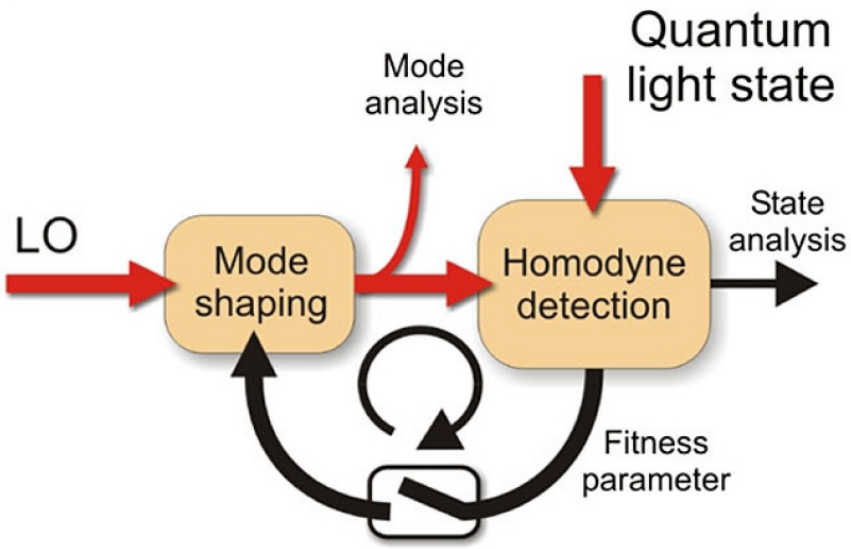

Figure 4.1 Schematic view of the experimental concept. A quantum light state of an unknown mode is characterised by means of Homodyne detection, that in order to be efficient needs to have the two states, the unknown and the LO perfectly matched. For this reason the Homodyne detection efficiency can be used as a fitness parameter, that tells us how well the two modes are matched. For optimisation this is repeated in a loop scheme, where a computer applies random profiles to the LO and the ones with the best efficiency reveal the profile of the unknown mode of the state under analysis.

The idea behind our experiments is based on the fact that the homodyne detection technique, in order to be efficient, requires the state under investigation to be perfectly mode-matched to the reference homodyne field, a strong coherent field, called the Local Oscillator (LO). Since the mode of the state under investigation may be completely unknown, we decided to use the experimentally measurable efficiency with which a given quantum state is detected as a fitness parameter to optimize the shape of the LO such that it optimally matches that of the investigated state. Once this optimization has

been successfully completed, the mode of the fragile quantum state is mapped onto that of the intense LO field, which can then be efficiently characterized by standard techniques.

In what follows we will deal with the measurement of the spectrotemporal mode of ultrashort single photon states generated by means of Spontaneous Parametric Down Conversion (SPDC), by using a Genetic Algorithm (GA) for the optimization of the LO mode. As already mentioned, for the Homodyne Detection to work, the two modes -that of the single photon and that of the strong coherent field- need to be perfectly matched in all degrees of freedom: polarization, spatial and spectrotemporal profiles. With spatial mode-matching carefully performed in advance and polarization matched using half-wave plates and polarisers, we keep all the other degrees of freedom fixed and just explore the spectrotemporal mode of our photons. To do this, we incorporate a Spatial Light Modulator (SLM) device in the LO path, able to perform amplitude and phase modulation for each individual wavelength component contained in our broadband LO pulses, when placed at the Fourier transform plane of a zero-dispersion pulse compressor. The GA applies initially random spectrotemporal profiles to the LO. For every profile applied, we obtain a value of the detection efficiency, which is then taken as the criterion for how well the two modes (that of the single photon and that of the LO) are matched. The algorithm proceeds through various loops of optimization of the LO spectrotemporal mode profile until the algorithm's fitness parameter (the homodyne detection efficiency) has converged to a steady maximum value. The LO profile corresponding to this maximized efficiency best describes the profile of our unknown state and is therefore sent to the diagnostic part of the experiment -in this case, the FROG device. As we saw in chapter 3, this device allows a full description of our pulses, including information on their spectral phase.

With this adaptive technique in our hands, we are able to unfold the unknown shape of any quantum state, without any prior information at hand, as long as there is a fitness parameter at our disposal.

4.1 General description of the experimental setup and first version with prism compressor

In the figure below we see a representation of the initial experimental setup.

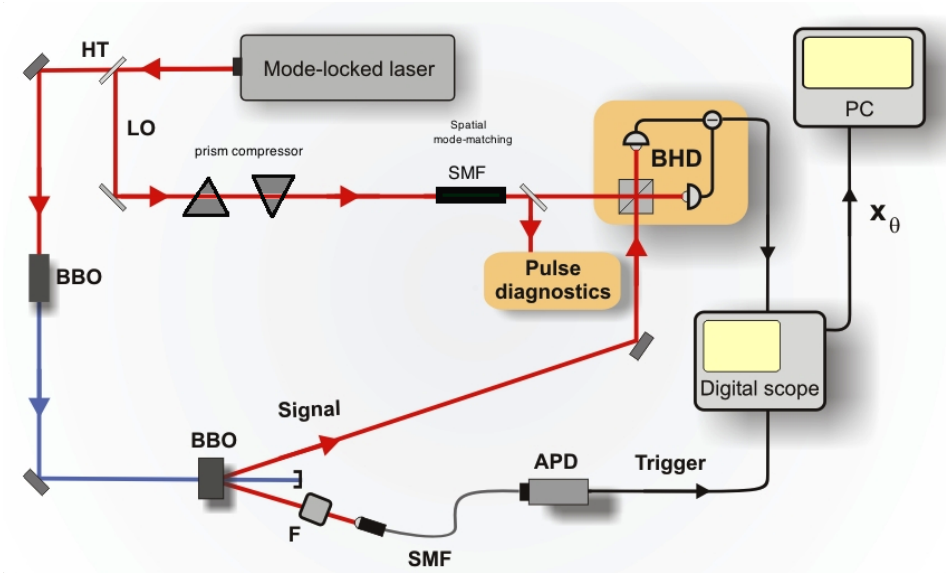

Figure 4.2 Initial experimental setup. Femtosecond-duration pulses at 800 nm and at a repetition rate of 82 MHz from a mode- locked Ti:sapphire laser are split by a high-transmission (HT-BS) beam splitter to serve as (i) the pump for spontaneous parametric down-conversion in a 300 μm-thick, type-I BBO crystal after frequency doubling in a BBO crystal;, (ii) the local oscillator field for balanced homodyne detection (B.H.D.) after mixing with the investigated states in 50% beam splitter. The LO spatial mode-matching is done using a single-mode fibre (SMF) and a pair of prisms is used to pre-compensate the dispersion caused by the SMF. F in the trigger, is a combination of spectral and spatial filters constituted by a narrow filter of 1.5nm spectral width, by a Lens f=600 mm and single-spatial–mode optical fibre directly connected to a single-photon counting module (APD). The relative phase between the interfering signal and LO at the homodyne, is varied by a piezoelectric transducer (not shown). There are additional optics and computer- controlled optical delay lines to adjust the synchronization of the different pulses (not shown).

In its first version, the experiment did not include a programmable pulse shaper based on a SLM for changing the LO spectrotemporal profile, but only made use of a relatively simple, but highly impractical, prism-based pulse compressor.

Starting from the top right, we have a mode-locked Ti:Sa laser as the main source of the apparatus, emitting 80 fs pulses at 800 nm with a repetition rate of 82 MHz. The pulse train is frequency doubled to 400 nm by second harmonic generation in a β-barium borate (BBO) crystal. The UV beam (pump) is then focused to a waist of 60 μm in another thin (300 μm) crystal BBO crystal, where degenerate type I Spontaneous Parametric Down Conversion (SPDC) occurs. Two twin photons are produced in this second crystal, the first one -the signal- is led to a Homodyne detector, while the second one –the idler- is used for heralding the presence of the first and is led to an avalanche silicon photodiode (Perkin Elmer AQR-14) after being spatially and spectrally filtered. The spectral filtering of the idler consists of an interference filter (1.5 nm), while the spatial filtering is implemented using a single-mode optical fibre and a lens of focal length 600mm. The usual pump power before the crystal is about 100 mW which results in 3000 counts/s of trigger count rate after the spectral and spatial filtering.

The signal photon is mixed at a 50:50 beam splitter with the local oscillator (LO), which is an attenuated part of the initial laser beam obtained with a high transmission beamsplitter at the exit of the laser. If necessary, the relative phase between the LO and the investigated state can be changed by applying a voltage to a piezo-electric crystal holding one of the steering mirrors. A single-mode fibre is also placed in the path of the LO in order to obtain a clean and perfectly well-defined spatial mode, which can be easily matched to the spatial mode of the generated single photon by means of a combination of

lenses. Since the spatial beam quality of the LO has to be preserved for the homodyne detection, the mode-cleaning fibre serves only at the ending part of the path of the LO beam, after all the other optics.

In order to pre-compensate the positive dispersion of the LO pulses introduced by the fibre, we use a double prism compressor setup placed just before it.

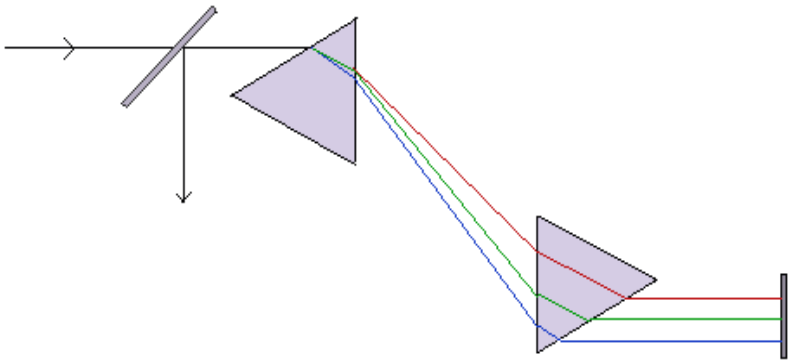

Figure 4.3 Schematic view of the two-prism compressor that was used in the initial experimental setup. Dispersing prisms from Newport, dimensions 25 mm and prism-distance 52 cm, material is SF10, a highly dispersive glass.

For alignment purposes and fine adjustment of the pulse synchronisation between the signal and LO pulses, we use stimulated emission rather than spontaneous. To do this, we inject a relatively intense seed pulse into the trigger channel and significant stimulated emission results in the signal. Using a translation stage we are able to synchronise with an accuracy of 0.1 μm the arrival of the stimulated signal pulse and the LO at the beam splitter and then we maximize the visibility of the resulting classical interference fringes between these two coherent pulses. Because of the very narrow spectral and spatial filtering on the idler path, the heralded single photons are generated in a highly pure state in a signal mode closely mimicked by the stimulated signal field [45]. Following that, we can conclude that the visibility

of the fringes between the stimulated signal and the LO tells us how close the matching is between the single photon and the LO mode beforehand, and so it serves as a criterion whether we can proceed to the homodyne measurements (a high visibility of the interference sets the ground for a good homodyne detection efficiency).

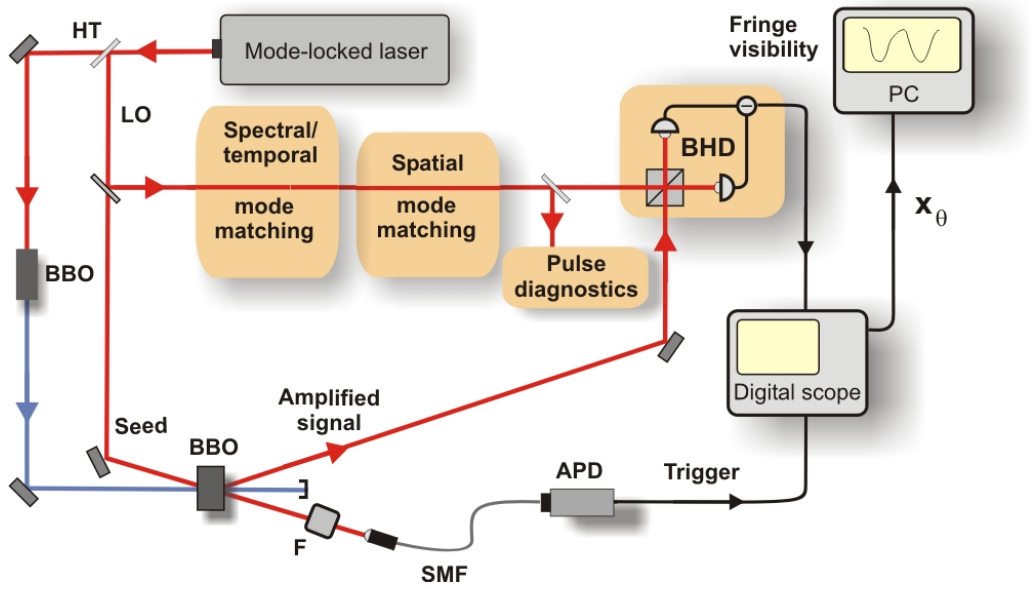

Figure 4.4 Experimental apparatus and conceptual alignment scheme. A part of the laser emission is used as the seed field used for alignment purposes injected in the trigger channel. The amplified signal beam, due to stimulated emission of PDC at the BBO, is then used for the alignment of the interference at the BHD, where the measure of the visibility of the fringes is the criterion of the matching between the interfering signal and LO.

At the homodyne [52-54], the two BS outputs are sent to two photodiodes (Hamamatsu S3883, with active area 1.7 mm2) connected to the positive and negative inputs of a wide-bandwidth (about 100 MHz) amplifier, which provides the difference (homodyne) signal between the two photocurrents on a pulse-to-pulse basis. The high bandwidth allows a temporal resolution such that it makes possible to distinguish the signal coming from consecutive pulses (separated by 12 ns). This permits to associate a single event to a

restricted temporal bin. The detector shows a linear response up to LO powers of about 9 mW, and with a signal-to-noise ratio of about 12 dB when the device is operated at the optimum LO power of 8 mW; the subtraction efficiency is about 60dB at 82 MHz.

The signal is sent to a digital scope (Tektronix TDS-7104), with an analogue bandwidth of 1 GHz, a sampling rate of 10^9 samples/s and a vertical resolution of 8 bits. In order to reduce the dark count rate, the signal coming from the SPCM is triggered in coincidence with the laser pulse train. This reduces the effective count rate, but also the ratio between the "false" and "true" events, which can be made lower than 1%.

Whenever a single-photon event occurs in the trigger channel, the scope stores a frame corresponding to two consecutive LO pulses, the first one is coincident with the trigger event, the second one contains information about the vacuum state and can be used as a reference signal. Since the single-photon state is invariant under rotation in the phase space (the marginal distributions and sections of Wigner function are the same for all values of the phase), the phase between LO and signal field is not controlled during the acquisitions.

About 5000 frames can be stored in a sequence at a maximum rate of 160000 frames per second. With an average rate of trigger counts of about 3000 s^{-1}, this means that each sequence is acquired in a few seconds. Each sequence of frames is then transferred to a personal computer where the areas of the pulses are measured and their statistic distributions, corresponding to the marginal distribution of the Wigner function, are analysed in quasi-real time.
From the acquired data it is possible to apply one of the reconstruction algorithms to obtain the density matrix and the Wigner function of the

detected state. In general, the state measured by homodyne detection in the LO mode – ψ_{LO} - is not pure, but rather a mixture of a single photon and vacuum, whose density matrix can be expressed as :

$$\hat{\rho}_{meas} = \eta|1\rangle_{\Psi_{LO}}\langle 1| + (1-\eta)|0\rangle_{\Psi_{LO}}\langle 0|$$

And its Wigner function corresponds in this case to the convolution of the Wigner function of the single photon with that of the vacuum state.

For the purpose of the present analysis, it is not necessary to reconstruct the full Wigner function of the state, but it is sufficient to compare the measured quadrature distribution to the expected theoretical one for a single photon observed with a global detection efficiency of η :

$$p(x,\eta) = \sqrt{\frac{2}{\pi}}\left[1-\eta\left(1-4x^2\right)\right]e^{-2x^2}$$

The η parameter can be easily extracted with a fit to experimental data and thus provides the fitness parameter for any procedure aimed to optimize the detection of our single photons.

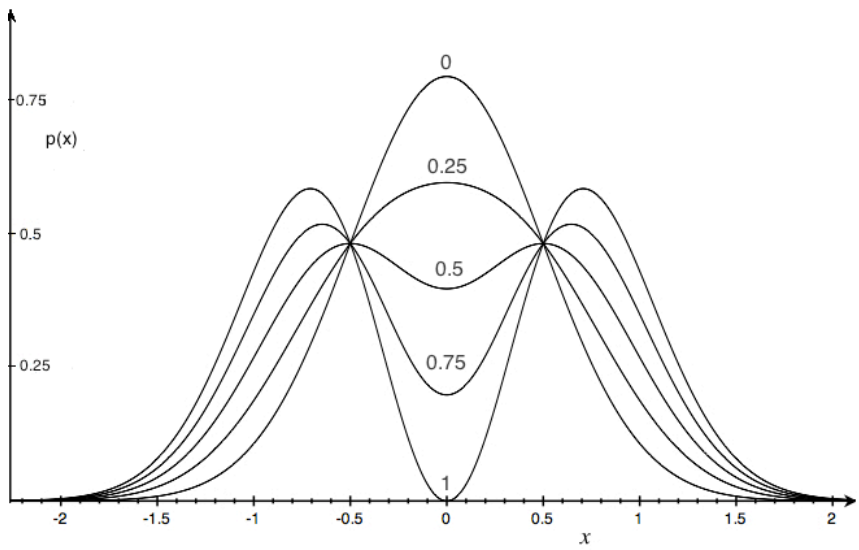

Figure 4.5 Marginal quadrature of the smoothed Wigner function for different values of the overall detection efficiency.

The first task to tackle for my PhD was the optimization of the SPDC process for the conditional generation of single-photon Fock states characterized by a negative Wigner function. In order to increase the efficiency of this process I have applied a new scheme in which the pump beam is tightly focused down to a size of 60 μm in order to exploit the large spatial bandwidth of the crystal (we use a very short crystal) and two lenses of f=100mm are used before and after the BBO crystal. The first lens is used to focus the UV pump beam at the crystal position. The second lens collimates the single photons produced by SPDC. In this way more idler light is coupled into the single-mode fibre, so that the trigger and therefore the acquisition rate of the homodyne detector are increased.

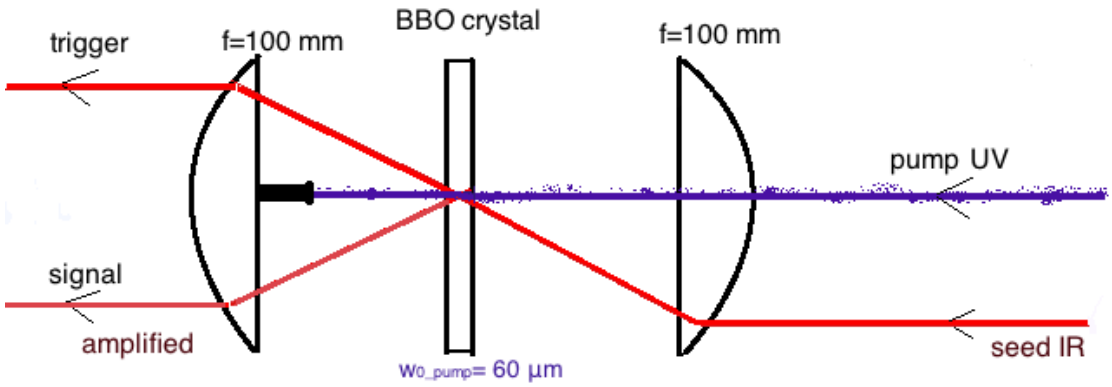

Figure 4.6 SPDC scheme, with focusing lens for the pump, and collimating lens for the single photon after the crystal. Here we see the alignment scheme, with the seed beam in the trigger channel, and the amplified light emitted due to stimulated PDC in the signal.

The collimation lens is also necessary for the alignment scheme, as the beam resulting from the stimulated emission becomes rapidly divergent after the crystal and makes it impossible even to track it down.

For the alignment procedure, we always start with measurement and alignment of laser spectrum that should have a peak centred at λ=802.7 nm and $\Delta\lambda$=10 nm, as well as the UV output from the SHG. Then the UV serves as

the pump for the PDC, so we start with its alignment in order to maximize the SPDC counts in the trigger channel. Using a SMF and an APD, we find this way the right direction for this channel, which then serves as a reference for the entire alignment procedure.

When the system is completely misaligned, meaning there isn't an even rough indication on where the two conjugate (signal and idler) channels are, we perform a basic alignment step, using a 3-hole mask system. This has 3 small hole, with the left and the right at equal distances (1.5 cm) from the middle one. Placing the mask at a distance of 57 cm before and after the crystal, we are in this way choosing the direction for which the idler and the signal beams form an angle of about 3°. We use the mask for an initial rough alignment of the beams and of the detectors, and then we perform a finer search around that area by scanning for the maximum SPDC counts. After the seed beam along the idler/trigger direction has been finely adjusted, we make use of a photodiode to find its best temporal overlap with the pump pulse by looking for the appearance of an amplified pulse along the signal direction. Once it is found, we keep the seed translation stage at that position and we proceed to the alignment of the LO.

For the alignment of the homodyne detection system we need the best overlap between the LO mode and that of the state that we aim to detect. Therefore, we use the amplified signal to simulate the heralded single photon assuming the two share the same spatiotemporal mode [45]. Our aim is thus that of maximizing the visibility of the interference between the amplified and the LO beams.

During the first year, the maximization of the overlap between the two beams was done with the help of a cooled CCD camera (from DTA Scientific Instruments, model Chroma C3 260) but, after we succeeded improving the

SPDC emission, the amplified beam was strong and collimated enough to use a SMF fibre instead. The fibre approach is even more precise and less time-consuming, with respect to using the camera that required the settings to be frequently adjusted. Much more importantly, it gives an additional information about the spectrotemporal matching of the two beams; in fact, by acting as a spatial filter, it gives a value of fringe visibility that correlates directly to the spectrotemporal degrees of freedom only, without contributions from the spatial component of the modes. At a point when we are feeling positive about the spectral overlap, we scan the temporal delay between the two pulses with the LO translation stage. For the femtosecond regime this delay can be very sensitive to changes (such as temperature, wavelength, laser GVD alignment, mirror movements etc.), hence one has to be thorough and for a long day's work and measurements check it on a regular basis.

Next step and the most indicative for the matching of the two beams, and therefore the criterion whether we are ready for the homodyne measurements, is to check the interference visibility without the SMF. We remove the SMF and transfer the photodiode directly at the exit of the homodyne BS to measure the maximum and minimum value of the intensity of the interference fringes after subtracting the background.

$$Visibility(\%) = \frac{I_{\max} - I_{\min}}{I_{\max} + I_{\min} - 2I_{background}} x100$$

We estimate that for a good over 85% visibility, a homodyne measurement is worth to proceed.

After setting the power of the LO at about 1 mW, we check the balancing of the BS to be as close as it gets to 50% and the two mirrors aligned to maximize the positive and minimize the negative signals of the two homodyne photodiodes. We then set the power level of the LO at 8mW, block the seed beam, switch on the APD to start the trigger acquisition. In order to acquire the right signal from the homodyne detector, we also carefully adjust the electronic delay between the homodyne signal and the trigger events. This is only necessary the first time, or once something in the electronics has been changed. To do that, we first roughly estimate the delay of each part separately (according to length of cables etc) for both homodyne and trigger channel and then scan for a range from -20ns to 20 ns around that value.

First measurements of the single photons generated in our setup, once they were successfully located within the scan for the electronic delay, demonstrated a 15% detection efficiency for a start.

In order to improve this, we went through a careful round of checks of the experimental parameters. For example, we checked that the long trigger fibre did not cause any negative effect on the homodyne efficiency. However, we found that there were other variables that did make a significant difference. One was the correct balancing of the light into the two homodyne photodiodes, obtained by moving the two focusing lenses in front of the detectors. Adjusting that brought an improvement of the detection efficiency from 15% to 39%.

Another important parameter to control was the degree of spatial filtering of the trigger channel, which could be adjusted by using lenses of the appropriate focal length: starting with a lens of f=200 mm before the trigger

fibre we got an efficiency of 34%, with a lens of *f*=300mm the efficiency increased to 42% and to a further 45.7% for a lens of *f*=500mm.

We also tested alternative photodiodes for ones with a better quantum efficiency, that is better than 92%, but this was inconclusive as there was no other photodiode with a clear superior efficiency.

At this point the setup was ready and working for the big changes that would turn it into something more than a static detection scheme, as the dispersion compensation capacity with the double-prism configuration was fairly restricted. The latter had to go and make space to the pulse modulation setup, that consisted of the zero-dispersion compressor and the SLM. This change would greatly upgrade the setup, as the double-prism was only able to partially compensate the fibre dispersion and not at all practical in use. For any minor change one had to estimate and measure numerous times for the alignment of the prisms, and then this would always turn out to be tremendously time-consuming without even being sure any direction change was for the better. Only having to relocate the interference fringes and realign a big part of the setup from scratch, every time we touched the prisms was enough evidence of the inefficiency of the setup in its current state.

4.2 Shaping the LO with a pulse shaper and a Genetic Algorithm

The new configuration offered undeniable advantages in that concern. We would be able to control electronically the phase and amplitude of each individual frequency component of our LO pulses. Before inserting the pulse modulation setup into the path of the LO beam, we had first to calibrate it (see chapter 3.2.3) and align it as I will describe below.

Aligning the pulse shaping setup

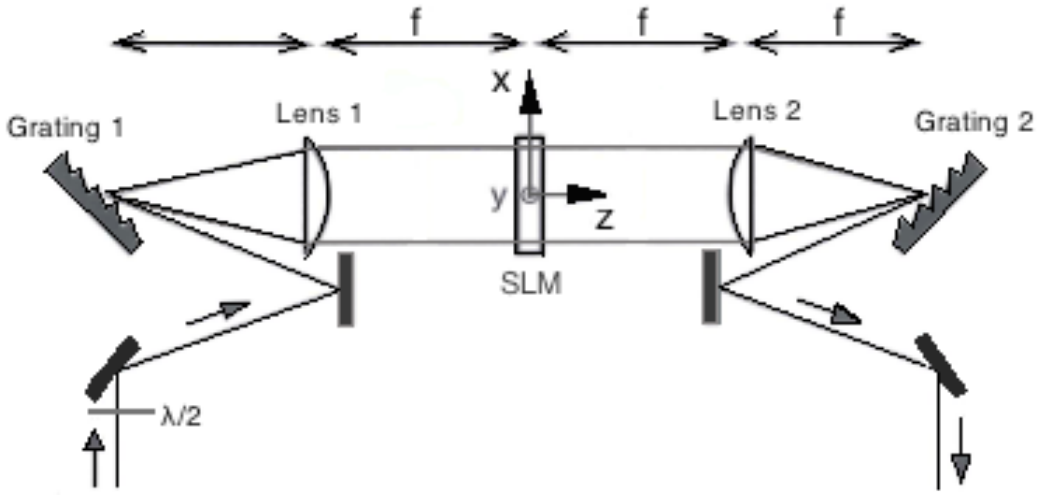

Figure 4.7 Zero-dispersion compressor and modulator. Grating 1 and 2 are the holographic gratings d=1/1800 mm^{-1}. Cylindrical Lenses 1 and 2 of *f*= 75 mm. SLM is the liquid crystal spatial light modulator placed in the Fourier-transform plane.

For the alignment of the 1st grating we followed the procedure described below:

1) We set the angle of incidence as close as possible to the diffracted beam (in order to avoid aberrations one should stay close to the Littrow angle ~46°). That is as much as the mechanical mounting allows as well as the focal length of the lenses in question (*f*≈75 mm) which limits the space and we read the angle of the goniometer 106°.

2) We rotate the grating in order to set the incidence beam normal to the surface of the grating and read the indication of the goniometer of the 1st grating. That would be the value of the normal (i.e. 50,5°). Then we rotate back to 106°. We knew then that the real value of the incidence angle $\theta_{i_1} = 106° - 50.5° = 55.5°$.
3) We calculated the diffraction angle θ_{d_1} = 38° (Equation 3.4 gives the grating equation, for first order of diffraction m=1 and the equation becomes $\lambda = d(\sin\theta_i + \sin\theta_d)$).
4) We set this as the diffraction angle for the 2nd grating $\theta_{d_1} = \theta_{d_2} = 38°$.
5) We repeated step 2 for the 2nd grating. Normal is at 87°, therefore we needed to rotate by 38° therefore the angle that we read on the mount should be 87°-38°=49°.

The two cylindrical lenses are placed on a translation stage to make adjustment of the distance lens-grating which highly affects the dispersion. To align the cylindrical lenses we used a narrow-band filter $\Delta\lambda = 1.4\,\text{nm}$, which we aligned in order to let pass the central wavelength $\lambda = 801.5\,\text{nm}$ of our spectrum. This was necessary because the beam after being angularly dispersed by the first grating, gave the spot size the shape of a highly unbalanced ellipse (one axis much bigger than the other) rather than a circle. With the narrow-band filter and with two irises we only saw a spot (the beam is not spread in the form of a line because of the filter) and this way we align the lenses looking at the back reflections, the best criterion for the finest lens alignment.

The half-wave plate serves for altering the laser's vertical initial polarisation because efficiency of the gratings is maximum for horizontal polarisation and also the transmissivity of the mask is maximum for horizontal light. This is

something to do with the construction of the SLM, as the two polarisers at the input-output windows of the device impose a horizontally polarised light. The polarisation is switched again before the beam splitter for the homodyne detection, in order to match the vertical polarisation of the single photon.

Two main things have to be checked for a proper alignment of a zero-dispersion pulse compressor: the first is to have the same spectrum and pulse duration at the input and output of the setup, which as mentioned above is very sensitive to the right distance between the two lenses and the gratings. The other thing is the shape of the spot at some distance away at the output of the setup. An "ugly" spot shape would be an indication of the incorrect distance of the second grating, meaning that the dispersed frequencies are not properly recombined.

To check the alignment we tried moving the second grating towards and further away from the lens observing the shape and the duration of the pulse, as well as moving both lenses together (in order to keep their distance fixed – with the help of the micrometre stages), and in both cases the pulse was becoming broader. Then, moving only the second lens, first towards the second grating the pulse was becoming shorter, whereas moving the second lens away from the second grating the pulse was becoming broader.

We also found that setting the correct angle of the 2nd grating is a very critical step. For its alignment, we set it first to the theoretically calculated angle (see above), and later we rotate it slightly while looking at the FWHM duration of the autocorrelator signal for fine adjustments.

There was only one more step before moving forward: to calculate the path difference that would be imposed on the LO by the introduction of the

shaper, in order to synchronise the arrival of the LO pulse at the homodyne BS to the single photon pulse again. This was a rather difficult task but several rearrangements on the optical table and large scans of the LO delay line allowed us to recover the interference fringes between the LO pulse and the alignment amplified one.

The other thing we had to work on, was a mode-matching scheme to couple again the LO light into the SMF, as the spatial mode coming from the SLM and entering the fibre was now different. Note that the final LO power level is very important for efficient implementation of homodyne detection measurements –it has to be at least 8 mW before the homodyne BS.

In the meantime we changed other things in the setup, like the SHG crystal (replaced a BBO of length l=0.3mm to a longer one l=0.6 mm) because we noticed damage on it, and the cube homodyne BS (Newport 05BC16NP.7) to a plane ultrafast one (Newport 10RQ00UB.2), more suitable for a femtosecond regime experiment. We also calibrated it, carefully measuring the splitting ratio as a function of the angle of incidence.

By only imposing a quadratic spectral phase with the mask to compensate the dispersion caused by the fibre, we were able to increase the visibility of interference fringes (as seen after with a photodiode after a SMF) between the LO and the amplified reference pulses up to 97-98%. The visibility without the SMF was a promising 90% and this allowed us to start testing the homodyne detection of our ultrashort single photons. After some re-alignments and improvements the homodyne efficiency reached over 55%, which we found by also manually scanning for the optimum quadratic and linear (corresponding to a temporal delay) spectral phase in the SLM.

Since this was the maximum efficiency we could get out of the homodyne detector, we were ready to test the next phase of the experiment, the use of a Genetic Algorithm (GA) to optimize the LO spectrotemporal mode.

The evolutionary or genetic algorithm is a population-based optimisation algorithm [77-79]. It is inspired by biological evolution to evolve a population, based on tools such as reproduction, mutation, recombination and selection. Candidate solutions or profiles to the optimisation problem play the role of individuals in a population, and a fitness function determined by the environment selects which of the individuals can survive and progress to the next generation.

This is the idea we used also for our detection scheme, as we have a computer controlled modulation double-mask system, where we can arbitrarily control the spectrotemporal degrees of freedom of the LO pulses, and the homodyne detection efficiency as the fitness parameter.

In general, we first generate an initial population of random voltage profiles (the individuals). Each individual is sequentially applied to the SLM, thus shaping the LO pulse according to its particular configuration of voltage levels (the genes). Each shaped LO pulse is used for the homodyne detection of the single photon and the observed value of efficiency η is assigned as the fitness parameter of that particular i-th individual. The voltage sequences of the best individuals are then cloned and also used to create the individuals of the next generation by means of cross-overs and mutations.

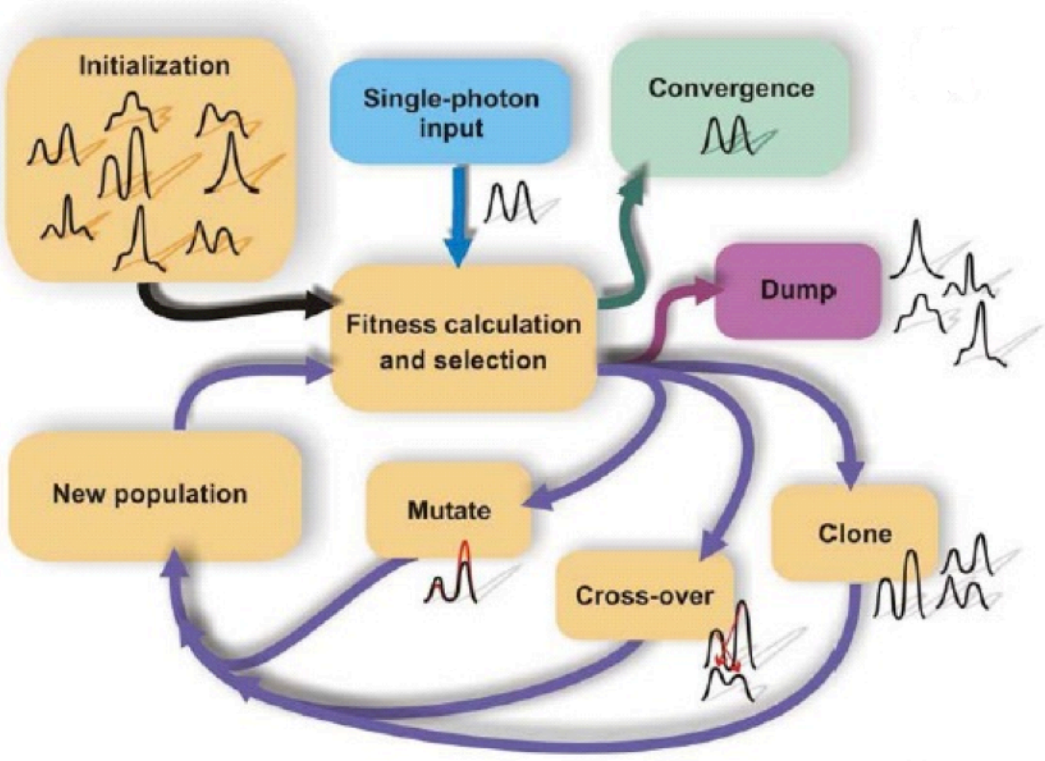

Figure 4.8 Scheme of the genetic algorithm used to match the LO spectrotemporal shape to that of the generated single photons. It starts with a set of a random profiles –a population- that are applied to the LO, out of which the ones with the good fitness are selected. Those are the then cloned, mutated and made part of cross over profiles, to form the new population. The ones that result a bad fitness are sent to the dump. This procedure is repeated iteratively for a number of populations until convergence is reached, which means the fitness parameter –in our case the homodyne efficiency- has reached a maximum value.

It is actually unnecessary (and realistically impossible) to use the full parameter space (of the order of $1000^{2x128} \sim 10^{768}$ possible pixel-voltage configurations) allowed by the SLM to optimize the LO. If the spectrotemporal shape of the investigated quantum states is not expected to be too complicated, as in this case, a much smaller parameter space can be safely considered. This can be done either by decimation and (linear or spline) interpolation of the pixel voltages, or by imposing some simple polynomial form for the amplitude and phase profiles. In these cases, the number of free parameters (the genes of each individual) in the adaptive algorithm is

substantially reduced and, depending on their number and on the number of individuals in the population, a good convergence can be typically reached after a few tens of generations. In the case of simple phase- or amplitude-only spectral modulations, a careful preliminary calibration of the SLM is required in order to fix the voltage profile of one mask according to that determined by the algorithm for the other mask. On the other hand, if both the amplitude and phase are to be optimized, we do not need to impose any restriction on the values of the SLM voltages, and we let the genes of both masks evolve freely in the algorithm, starting from a completely random initial configuration.

The algorithm depends on several parameters determining population features, cross-over and mutation procedures, genome length, etc.. The measurement effectiveness can be improved if these parameters are properly adjusted according to the particular experimental features. From a typical population of 21 individuals, we usually derive 3 clones (the parents), 6 offspring, and 12 mutations that constitute the elements for each new generation. Offspring is obtained by crossing the parent chromosomes in multiple points. Gene by gene mutations are performed on the parent genes with a 50% probability. The gene value is changed by a quantity picked from a Gaussian distribution with an initial standard deviation of about 1/6 of the total voltage range. The distribution width is then continuously adjusted depending on the ratio between successful and total mutations. The initial number of genes is typically 5 (for a phase- or amplitude-only modulation) or 10 (for a complete amplitude/phase optimization), but a finer control of the fitness can be achieved by increasing the gene number during the optimization. Also in the case of the polynomial method, 5 parameters are normally used, i.e. the central frequency and up to the fourth power of the frequency expansion of the spectral phase or amplitude.

Obviously, since the fitness estimation is based on the extraction of statistical information from many homodyne measurements, one has to rely on a large supply of identical single photons for the adaptive procedure to work properly. If the experimental conditions fluctuate too rapidly, it is actually impossible for the system to work, and convergence is never reached. Nevertheless, the adaptive algorithm is intrinsically able to adapt to slow changes: for example, we have clearly observed that it follows the slow temporal drifts between the single photons and the LO occurring during long overnight acquisitions.

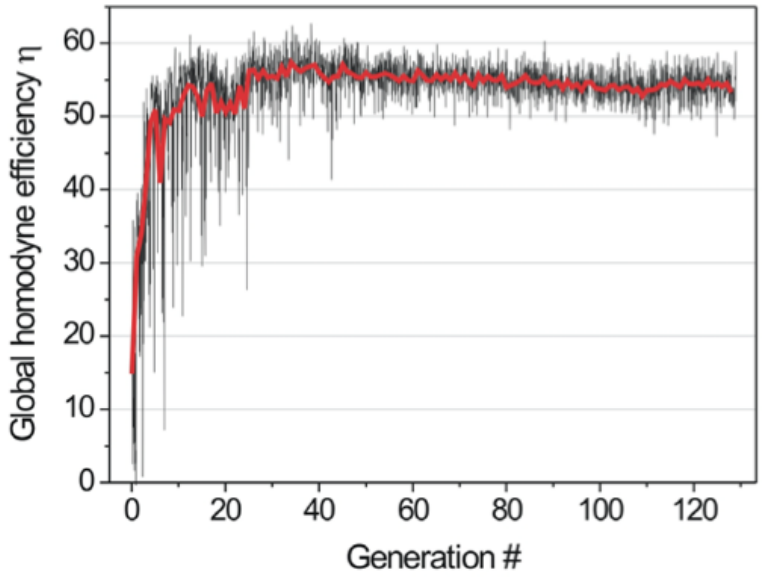

Figure 4.9 Typical evolution of the fitness parameter (the total homodyne efficiency η) across several generations towards convergence to the optimal shape. The black curve corresponds to the different individuals, while the red one is the average efficiency for each generation. Starting from average initial values smaller than 10% for the fitness of the individuals in the first generation, we observe a typically rapid increase of the efficiency over the next few generations followed by a slower adjustment toward the optimum shape. Convergence is obtained already after about 30-40 generations. Here a slow decay is also observed, probably due to deteriorating spatial mode-matching and decreasing laser power during the long (about 14 hours) measurement run. The sudden, isolated, drops in the efficiency curve are due to the appearance of "bad" random mutations.

4.3 Experimental Results

4.3.1 Unmodulated single photon

When the single photons generated by our experimental setup are not modulated in any way, we expect their spectrotemporal mode to be that of an almost Fourier transform limited pulse. Accordingly, the spectrotemporal shape of the LO that optimizes homodyne detection efficiency, should be close to a transform limited pulse, therefore with an almost flat spectral shape indicating no dispersion.

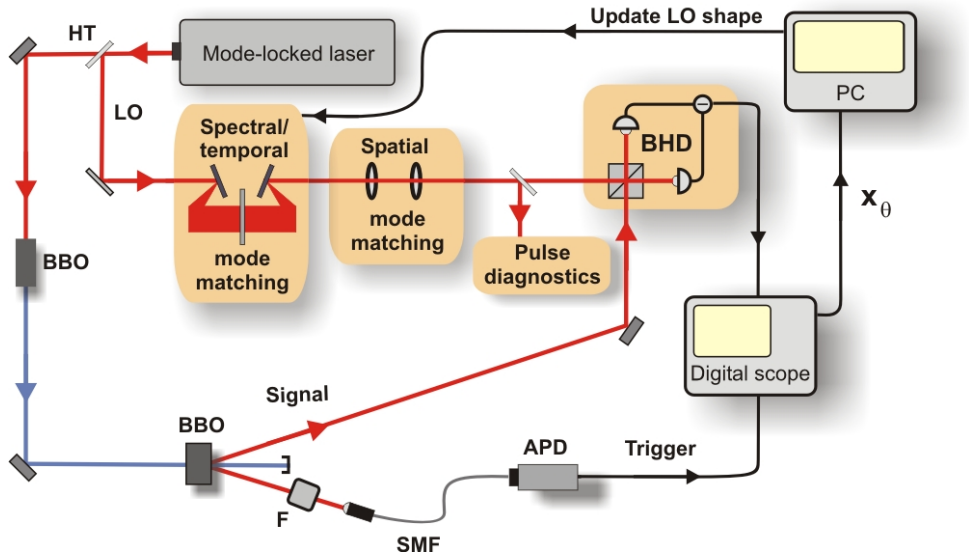

Figure 4.10 Experimental setup for measurement of the unmodulated single photon using the Genetic Algorithm. The LO spatial mode-matching is done using a single-mode fibre (SMF) with a combination of lenses. A pulse shaper has replaced the prism compressor for pre-compensation of the dispersion caused by the SMF, as well as for the spectrotemporal mode matching. The spectrotemporal degrees of freedom are no longer fixed, and they are used as free parameters for the Genetic Algorithm. The best spectrotemporal profiles the Algorithm has retrieved are then sent to the Pulse Diagnostics, that is the FROG device. First test of the setup was done for the unmodulated single photon state.

Since the LO pulses pass through the 10 cm long single mode fibre for spatial mode cleaning, the SLM roughly has to introduce an opposite quadratic dispersion to pre-compensate this effect and send transform limited pulses to the homodyne detector. As the FROG measurement is done after the SMF and just before the homodyne detector, we expect this measurement to reveal the true spectrotemporal shape of the unmodulated single photon, regardless of the modulation imposed to the SLM.

Of course this is true if the pulses coming from the laser itself and used for the LO and the SPDC pump are transform limited. This is not always the case and a careful check of the laser performance has to be performed before any measurement run. In some cases it happened that unexplainable chirps on the measured single photon mode were finally traced back to an imperfect compression of the pulses at the exit of our mode-locked laser.

An example of a typical result from a run of the GA on our unmodulated single photons is reported below. In this case we run the GA for 60 generations while letting both the spectral phase and amplitude to vary during the optimization.

We obtain a final detection efficiency of about 58%. The FROG measurement of the best individual of the last population shows a pulse with an almost flat spectral phase, indicating the absence of any significant frequency chirp.

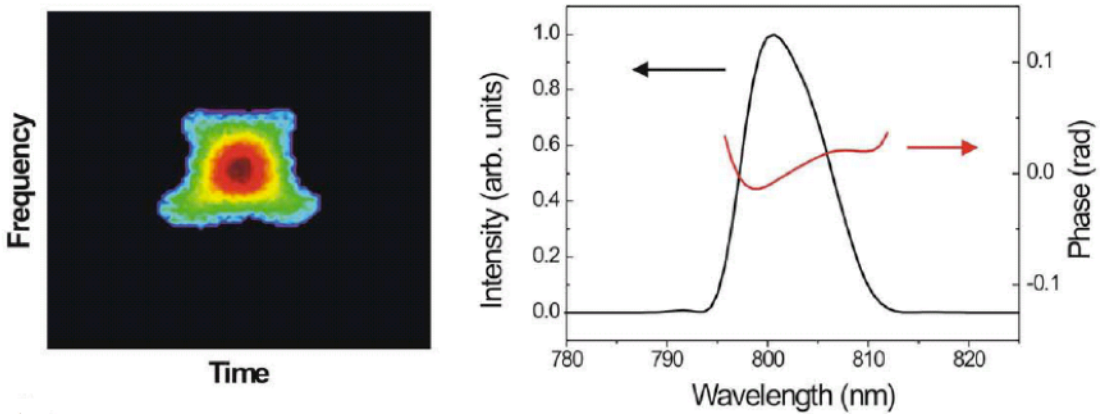

Figure 4.11 Experimental FROG trace (left panel) and reconstructed spectral intensity and phase profile (right panel) for the optimal LO pulse matching the un-dispersed single photons, after a full amplitude and phase optimization.

4.3.2 Dispersed single photon

In order to put the method to a more stringent test, we need to make use of arbitrarily-shaped single-photon pulses. Differently from other recent schemes [23,24] using "long" single photons produced by narrow-band atomic samples, where electronic modulators and detectors can keep up with the slow temporal evolution of the photon wavepacket, here both the modulation and the detection stages have to use completely different approaches due to the ultrashort duration of the wavepackets.

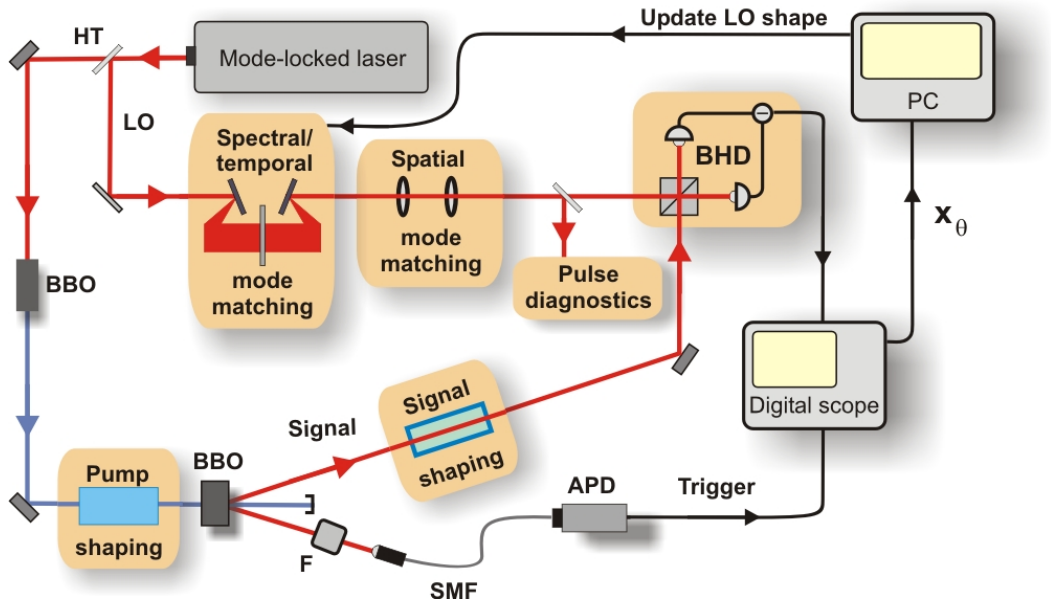

Figure 4.12 Experimental setup for measurement of differently shaped single-photon states using the Genetic Algorithm. In one case the single photon is shaped directly by 10 cm glass block BK7 inserted in the signal path and it is therefore dispersed and temporally stretched, and in the other the single photon inherits the characteristics of the pump through SPDC, that is shaped by a Michelson interferometer. We tested the algorithm for two different configurations of the Michelson interferometer, the spectrally narrow single photon and the double peaked single photon.

We first decided to insert into the path of the pump a 10-cm-long block of BK7 glass, to temporally stretch the pump pulses and, consequently, the generated single-photons. However, despite the fact that the visibility of the interference was ranging around the usual values, the homodyne efficiency dropped significantly (around 45% was the maximum efficiency the GA returned after 16 generations). The reason was that the prolonged pump pulse in this condition was much longer than the trigger pulse selected by the 1 nm bandwidth filter, and the purity of the heralded single photon was therefore severely degraded.

To be able to perform this measurement we moved the BK7 glass and placed it directly in the single photon path, so it wouldn't cause the purity to degrade.

We initially impose a simple phase-only polynomial modulation to the spectrum of the LO. Here, it is the (few) coefficients of the polynomial expansion that constitute the genes on which the evolutionary algorithm operates. While the linear component of the spectral phase accommodates for possible temporal delays between the single photon and the LO, the main correction applied by the mask and visible in Figure 4.13, is in the quadratic phase term, corresponding to the introduction of a linear frequency chirp in the LO pulse.

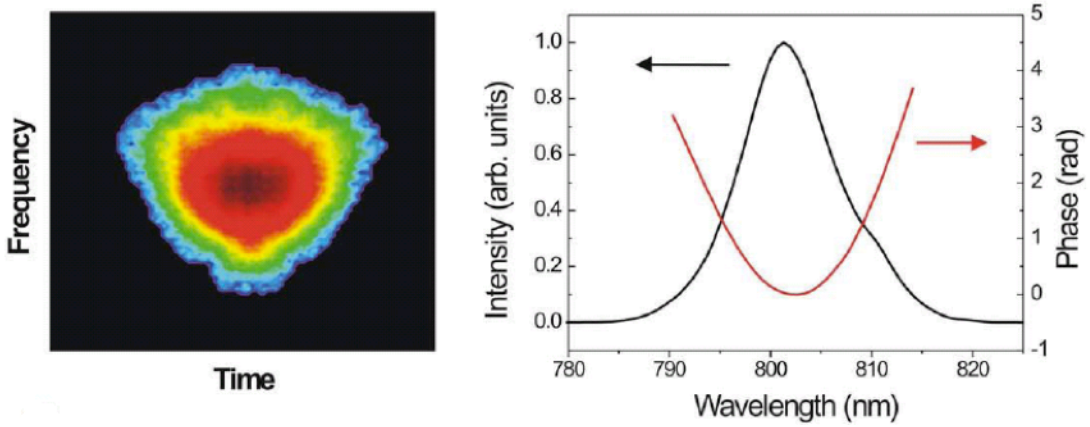

Figure 4.13 Experimental FROG trace (left panel) and reconstructed spectral intensity and phase profile (right panel) for the optimal LO pulse matching a frequency-dispersed single-photon after a phase-only optimization.

In the next run we let both the spectral phase and amplitude of the shaped LO pulses vary in the adaptive algorithm. In this case a better efficiency is reached, and we obtain the shape of Figure 4.14, which still presents the same quadratic spectral phase, but a significantly different spectral intensity that, as expected, is much more similar to that of the un-modulated single-photon.

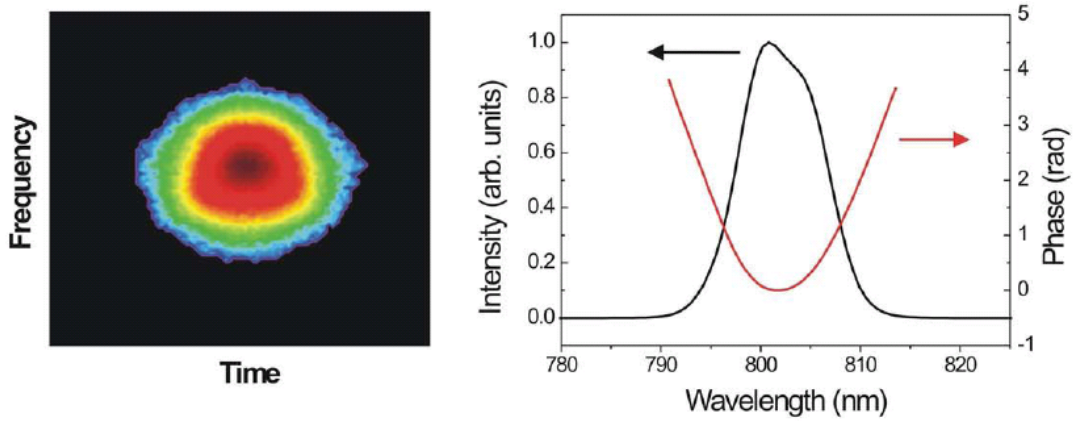

Figure 4.14 Experimental FROG trace (left panel) and reconstructed spectral intensity and phase profile (right panel) for the optimal LO pulse matching a frequency-dispersed single-photon after a full amplitude and phase optimization procedure.

The best detection efficiency obtained while measuring the dispersed single photons with the optimally-shaped LO pulses reaches $\eta_{opt} \approx 60\%$, whereas using a transform-limited LO pulse reduces it to less than 50%. If, instead of a short glass block, one had propagated the single photons through the dispersive transmission line constituted by a long optical fibre, the resulting quantum state would have been essentially lost to a detection system not taking these spectrotemporal modulations into account.

4.3.3 Shaping the single photon by modulating the pump pulse

More complex modulations on the profile of the single photon are obtained by shaping the 400 nm pulses pumping the parametric down-conversion crystal. Indeed, it was demonstrated that the single photon conditionally generated in this way essentially inherits the spectral properties of the pump if the filtering of the herald idler mode is sufficiently tight [45-48]. In this case, we chose to place a Michelson interferometer (MI) in the path of the pump pulses to the parametric crystal.

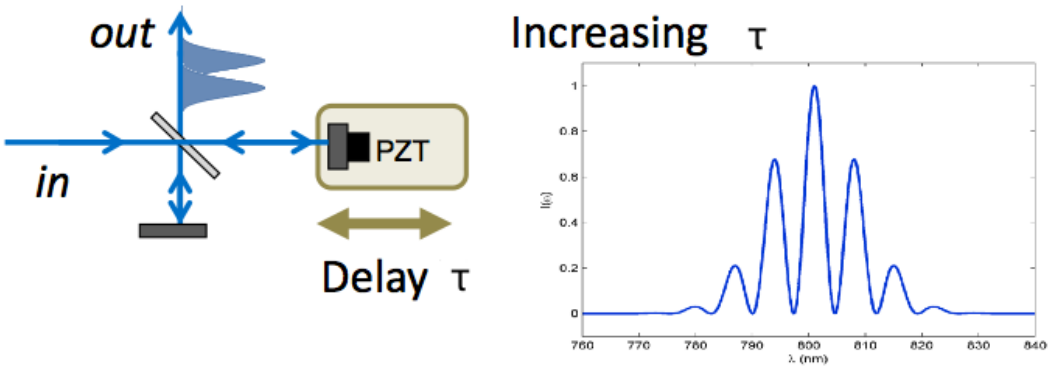

$$H(\omega)=\frac{1}{2}\left(1+e^{i\omega\tau}\right)$$

Figure 4.15 Schematic view of a Michelson interferometer. Translation of one mirror of the interferometer, changes the path of one arm of the interferometer which causes a delay between the interfering pulses- as the delay increases the number of spectral peaks increases too.

In order to introduce the Michelson interferometer, I will be briefly explaining its function with the aid of the figure above. Pulsed light is sent to a beam splitter, where it is separated into two equal components. Mirrors reflect the light back to the beam splitter, where it is then recombined. One is a translating mirror and provides the possibility to alter the path to the BS. The two copies of the pulses then recombine with a variable delay τ. What happens next depends on the difference of paths taken by the two beams. If they have both travelled exactly the same length, they will interfere with each other constructively, but if the distance taken by the two beams is different, a different kind of interference will take place.

Adjustment of the relative delay between the two pulses causes a sinusoidal modulation of the spectrum with a period inversely proportional to the delay. The mirror is mounted on a translation stage for coarse movements and on a piezoelectric translator to finely adjust the relative phase between the two interfering pulses.

In order to roughly calibrate the delay of the MI with a μm precision, we block one arm of the interferometer at a time and do a scan of seed stage looking at the amplified pulse, and then subtract the results corresponding to the two positions of maximum signal.

In our setup the MI was used in two different configurations for the purpose of the pump shaping, placing either a peak or a valley of the sinusoidal modulation in correspondence to the maximum of the pump spectral profile.

Spectrally narrow single photon

In the first case, the MI acts as a spectral filter for the pump, which translates into a stretched temporal profile. These characteristics are then inherited by the single photon. Below we report a typical result for a measurement of a spectrally narrow single photon obtained with a MI delay of about 150 fs and retrieved after running the GA for 126 generations.

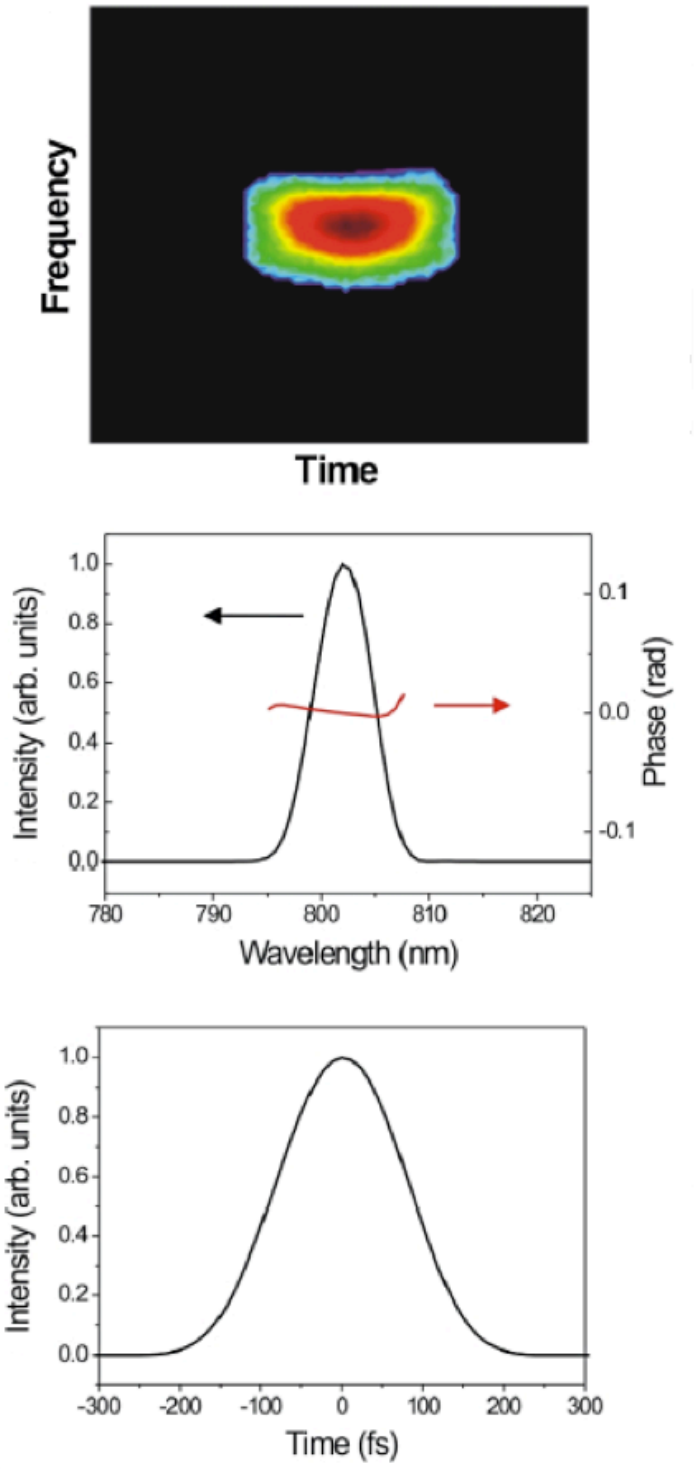

Figure 4.16 Experimental FROG trace (top panel), reconstructed spectral intensity and phase profile (middle panel) and reconstructed temporal intensity (bottom panel) for the optimal LO pulse matching a spectrally-narrow single-photon after a full amplitude and phase optimization procedure.

In these measurements our single photon is shown to acquire the expected narrower spectrum with a flat spectral phase, and a prolonged duration of FWHM in the range between 160-220 fs (depending on the delay imposed on the interferometer), instead of 100 fs, the ordinary duration of an unmodulated single photon. In the particular measurement of Figure 4.16, a FWHM spectral width of 6.4 nm is observed, together with a corresponding FWHM pulse duration of 180 fs.
Note that the same results are also obtained by manually inserting in the SLM the parameters corresponding to the expected spectral modulation due to the MI on the pump path.

Double-peaked single photon

For these measurements the Michelson interferometer is set in a condition that causes a partial destructive interference in the region of temporal overlap between the two outgoing pulses. This results in a double-peaked temporal and spectral profile of the pump field. In more simplistic words we could say that the MI "digs a hole" on the pump spectrum, which is later inherited by the single photon through the process of SPDC.

Below we see a typical FROG results for the case of a double-peaked single photon. In all cases the algorithm is able to retrieve the double peak structure both in the spectral and the temporal profiles of the single photon. Also notice the expected pi phase jump between the two spectral peaks, a result of all the measurements we performed for this condition.

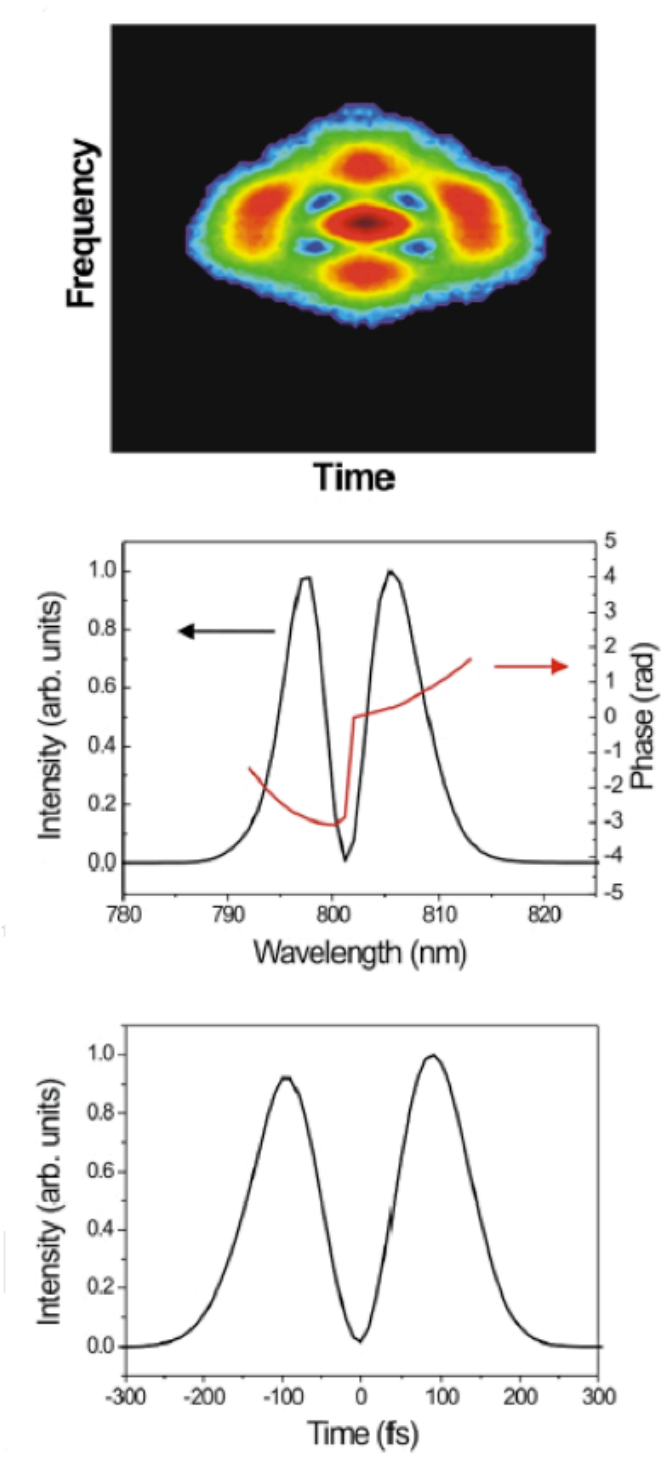

Figure 4.17 Results of the best individual of a 100 generation run of the GA (the profile with the best detection efficiency out of 100 x 21 individuals). We observe the expected π phase jump in the centre of the spectrum. In this case we also find an additional quadratic phase modulation that is likely connected to an observed slight change of the pump spatial mode. Correspondingly, the maximum efficiency achieved with the evolutionary algorithm is limited to about 45-48% in this condition.

One interesting thing with these measurements was the following: In the configuration where the MI induced a narrow single-peaked photon we had a 98% spectral visibility with the SMF, 91.5% visibility without, and a homodyne efficiency of approximately 58%. In the case where the MI induced the double-peaked configuration, the spectral visibility (with the SMF) was still as high as 99%, but the overall visibility (without the SMF) dropped to 82% for no explicit reason. For this, the homodyne efficiency we measured in the double-peaked situation could not overcome the 48%. Due to the fact that the drop in the visibility takes place when the spatial mode-matching is playing a role, we were forced to assume that the MI is somehow also affecting the spatial profile of the pump, even though it is not normally known to behave in such manner. To try and overcome the problem, we used a pinhole-based spatial filter for the pump after the Michelson interferometer but, despite the ensured better stability of the setup, this didn't seem to matter much for the visibility of the double-peak configuration. The result was an improved homodyne efficiency of about 59.5% in the case of the single-peaked configuration, whereas in the double-peaked case the homodyne efficiency remained at 48% as the maximum. This was also the best efficiency the GA returned at the end of a long-run acquisition.

4.3.4 Phase-coherent detection of a spectral single-photon qubit

Following the successful retrieval of the spectrally double-peaked single photon with the genetic algorithm, we tried a different kind of experiment using the same configuration of the MI. In this case, one can consider the single photon to be delocalised both spectrally and temporally, meaning it does not occupy one peak or the other but rather co-exists in a coherent superposition of the two peaks. Thus under the circumstances we can define

two new spectrotemporal modes Ψ1 and Ψ2 based on these peaks, and thanks to the coherent delocalisation in time and frequency this superposition state may be used to encode, manipulate and detect, qubit information with a single photon.

If the state $|1\rangle_{\Psi_1}$ is assigned to the photon occupying the first spectral peak, and the $|1\rangle_{\Psi_2}$ state to the photon in the second one, such a pump modulation allows the realization of the state

$$2^{-1/2}\left(|1\rangle_{\Psi_1}|0\rangle_{\Psi_2}+|0\rangle_{\Psi_1}|1\rangle_{\Psi_2}\right).$$

Reversing the logic sequence of this idea, what if instead of optimizing the LO profile to match this state, we did the exact opposite? That would mean preparing the orthogonal LO spectral mode by adding a $\phi_{LO}=\pi$ phase shift between the two spectral peaks by means of the SLM. This would thus correspond to performing a homodyne measurement that projects the investigated state onto the orthogonal one $2^{-1/2}\left(|1\rangle_{\Psi_1}|0\rangle_{\Psi_2}-|0\rangle_{\Psi_1}|1\rangle_{\Psi_2}\right)$. If the state were indeed in a coherent superposition of the two spectral modes instead of just a statistical mixture of the two, then this would cause the homodyne efficiency to vanish. So, by observing the efficiency drop to zero, we can prove the coherence of the superposition state.

We set the LO in the orthogonal mode by imposing an increasing phase shift in steps of 0.1π between the spectral peaks and measuring the corresponding homodyne efficiency. Below we report the FROG-measured spectral and temporal mode profiles for the two extreme cases of $\phi_{LO}=0$ and $\phi_{LO}=\pi$. Their orthogonality is particularly evident in their measured temporal shapes. We also plot the measured single photon homodyne efficiency η as a function of the phase ϕ_{LO} between the two LO spectral peaks, where a clear sinusoidal modulation is apparent.

Finally, also the reconstructed Wigner functions for the two cases of $\phi_{LO}=0$ and $\phi_{LO}=\pi$ are shown. When the state is analysed in the correct mode, the Wigner function of a single photon is clearly obtained, whereas the Gaussian function of a vacuum state appears when the state is analysed in the orthogonal mode.

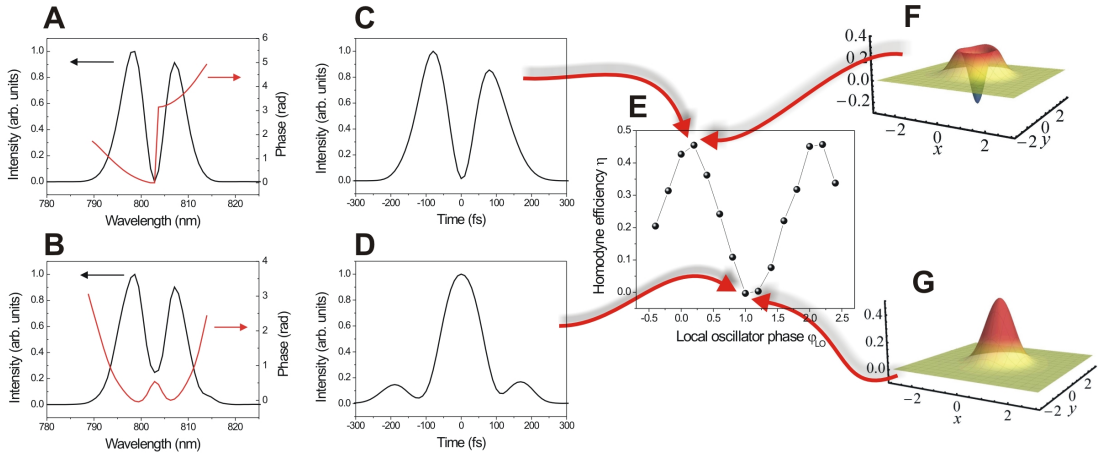

Figure 4.18 Probing a spectrally and temporally delocalized single photon. FROG-measured spectral intensity and phase profiles of the LO mode for (a) $\phi_{LO}=0$, (b) $\phi_{LO}=\pi$. The corresponding temporal intensity profiles are shown in (c) and (d), respectively. Note the clear double-peak structure of the LO in the $\phi_{LO}=0$ case and the nearly orthogonal temporal shape obtained in the $\phi_{LO}=\pi$ condition. (e) Variation of the measured single-photon homodyne efficiency η as a function of the phase ϕ_{LO} between the two LO spectral peaks. Reconstructed Wigner functions of the detected state: a single photon in (f) for $\phi_{LO}=0$ and vacuum in (g) for $\phi_{LO}=\pi$.

This result is significant, as one can only think of the possibility of extending in higher-dimensional spectral qudits. Simply increasing the MI delay between the two pump pulses, the generated single photon remains delocalised between only two temporal modes, but spectrally the number of peaks increases. So in the frequency domain the single photon breaks up into a series of equidistant spectral peaks with a comb-like structure. These

distinct spectral modes correspond to the maxima of the sinusoidal modulation of the pump spectrum and their number is roughly limited by the ratio of pump to idler-filter bandwidth. The larger the pump bandwidth, the more independent spectral channels are available.
Implementing this scheme with multiple spectral peaks, as well as the proof of their mutual coherence is the direction we plan for this experiment and we are already working on.

4.4 Upgraded experimental setup

The fibre placed in the path of the LO and used for collimation has clear benefits for cleaning its spatial mode before the homodyne detection. These benefits were found particularly useful when working on another experiment in the picosecond regime. However, the much higher peak intensities of the femtosecond pulses used in this experiment were discovered to produce nonlinear effects that could distort the LO spectrum. These would increase with increasing input power level in the fibre, but they would be hard to compensate, as the fibre itself is the last optical element before the detector and thus cannot be corrected by the SLM.

We tested for this, measuring the LO pulse characteristics for various quadratic dispersion profiles set with the SLM in the cases with and without the fibre. Below we see a table of these measurements:

Table 1: Without the fibre [1]

Quadratic coefficient set in SLM (a.u)	b2 – retrieved from FROG (fs^2)	FWHM duration (fs)	FWHM bandwidth (nm)	TBP
0	1159	81	9.7	0.36
-500	818	80	9.6	0.36
-1000	-1315	97	9.7	0.44
-1500	-2196	124	9.4	0.55
-2000	-3020	154	9.1	0.65
-2500	-4367	182	9	0.76

Table 2: With the fibre [1]

Quadratic coefficient set in SLM (a.u.)	b2 – retrieved from FROG (fs^2)	FWHM duration (fs)	FWHM bandwidth (nm)	TBP
0	6616	284	12	1.59
-500	6280	255	11.6	1.38
-1000	5189	227	11.2	1.18
-1500	4481	175	10.7	0.87
-2000	3284	142	9.3	0.61
-2500	1099	115	8.4	0.45
-2700	-117	80	11.2	0.42

The data of table 2 tells us that with the SLM at zero the quadratic coefficient is positive and then the SLM then adds negative dispersion to compensate for the positive one introduced by the glass fibre.

[1] The error range in the measurements is about 5% and comes from the retrieval

However, looking at both tables 1 and 2, it is made evident that, without the fibre, the LO pulses are close to transform-limited ones, with the minimum pulsewidth allowed by their spectral bandwidth, for close-to-zero additional quadratic dispersion by the SLM. Actually, a small residual positive dispersion due to lenses, beamsplitters, etc. is present also when the SLM introduces no additional dispersion. The bandwidth of the pulses is also found not to vary substantially with their duration.

On the contrary, when the fibre is inserted, the SLM is only able to partially pre-compensate for its quadratic dispersion, but cannot do anything to adjust for the spectral broadening, most probably due to optical Kerr effect, occurring when the pulses reach their minimum duration and maximum intensity in the fibre.

So, even if the SLM effectively corrects the quadratic dispersion introduced by the fibre, the LO pulses reaching the homodyne detector may have a substantially larger bandwidth (and depending on the LO power used) compared to the one of the heralded single photons. This may therefore reduce the final detection efficiency and the accuracy of the entire approach.
In principle, if the fibre was placed before the SLM and not after, the genetic algorithm would be able to track down any irregularities due to nonlinear effects and compensate for them, but in this case any use of the fibre on the table would have lost its meaning entirely, as it was there to produce a well-collimated mode for the spatial mode-matching necessary for the homodyne detection. If the beam coming out of the fibre passes through all the optics of the zero-dispersion pulse compressor, it loses its clean mode and well-defined spatial properties.

That is why the decision was made to replace this fibre and start designing a spatial filter to do that. The initial thought was to design a filter that would reproduce the mode of the fibre, and keep the homodyne mode-matching lenses intact. After a few attempts in that direction, it was realised that designing a new spatial filter to mode-match the LO directly to the amplified spatial profile was a lot more practical and easier to manipulate. Additionally, this scheme included only two lenses, meaning fewer degrees of freedom to keep under control at this stage. This is what we did at the end. We set up a spatial filter composed by a focusing lens $f1$=80 mm, a pinhole of diameter D=100 μm and a collimating lens $f2$=50 mm, placed on micrometer stages. After a few sets of measurements, the optimum positioning of these optical elements was found that allowed us to recover a good visibility between the LO and the amplified alignment pulse. Now that there was no fibre to account its dispersion for with the SLM, we very rapidly regained a good homodyne detection efficiency of about 56% that allowed us to run new tests of the GA again for differently shaped single photons.

4.4.1 Unmodulated single photon

We started from measuring the dispersion of an unmodulated single photon, by varying the quadratic phase term of the mask in a wide range and measuring the corresponding homodyne efficiency for the detection of the photon. From the plot of the data we see below, the best quadratic coefficient is about +600, in agreement with the settings used to obtain transform-limited LO pulses in Table 1.

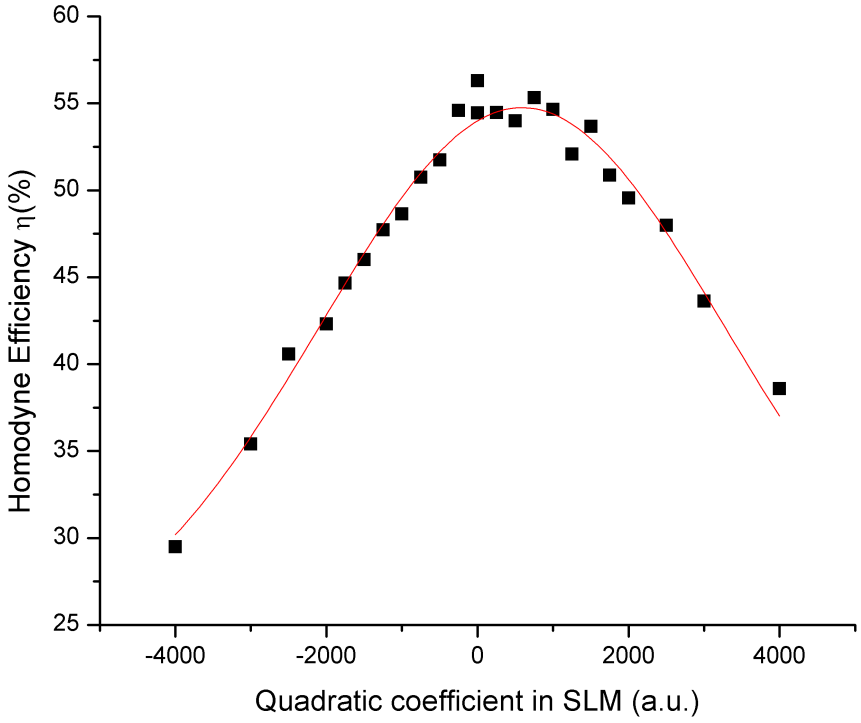

Figure 4.19 Plotted Homodyne Efficiency [2] with quadratic coefficient for an unmodulated single-photon. We see that the mask adds positive dispersion to match the slightly chirped single photon.

We then proceeded with measuring the unmodulated single photon, by running 14 generations of the GA. FROG traces and reconstructed spectral and temporal profiles for the best individual of the evolution are reported below.

[2] The error range in homodyne measurements is usually small, about ±2%.

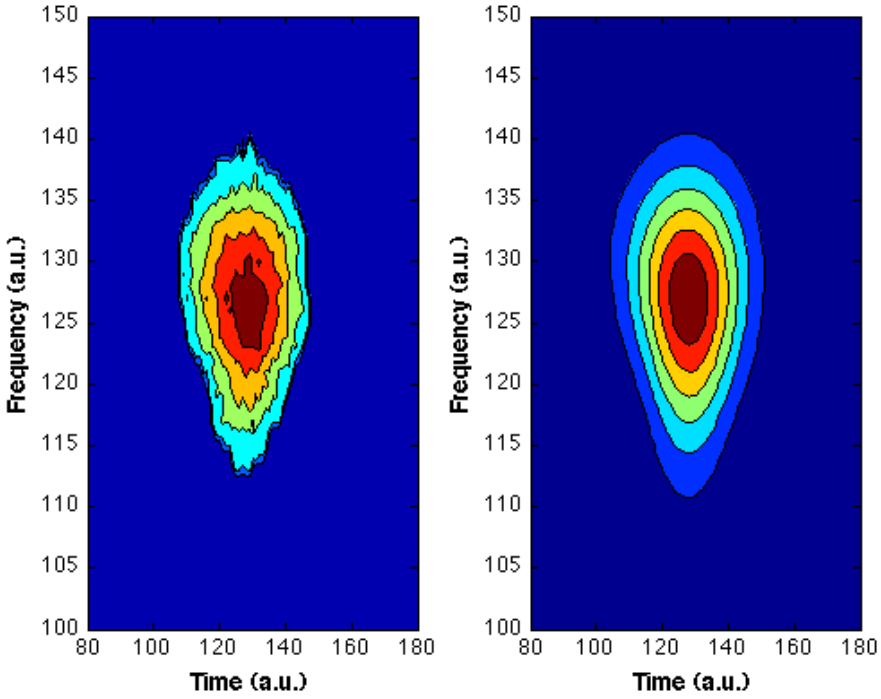

Figure 4.20 Experimental FROG trace, measured and retrieved for an unmodulated single photon. Results for the best individual of a 14 generation run of the GA (the profile with the best detection efficiency out of 14 x 21 individuals).

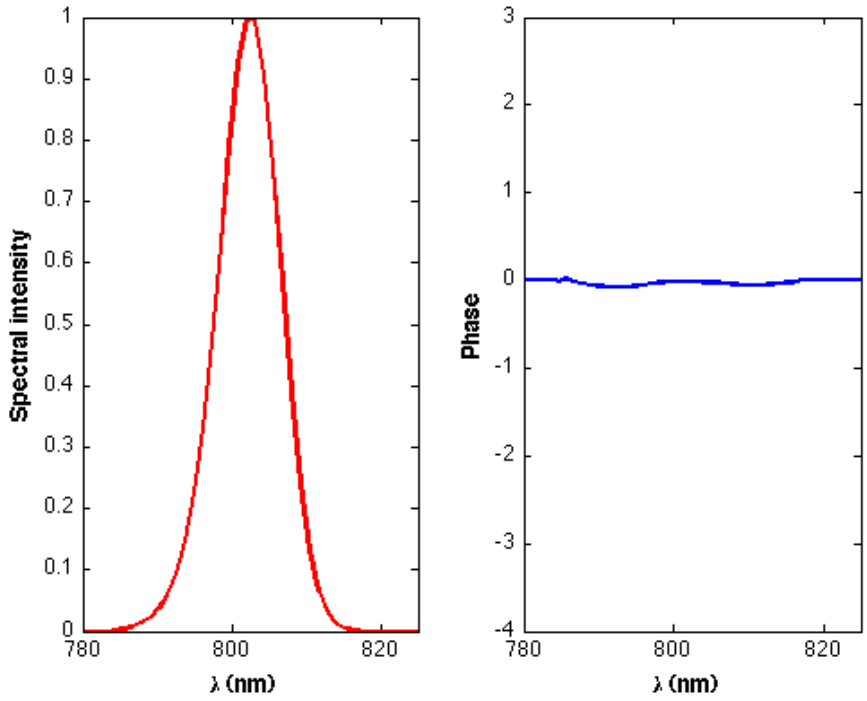

Figure 4.21 Reconstructed Spectral Intensity and Phase. Results for the best individual of a 14 generation run of the GA (the profile with the best detection efficiency out of 14 x 21 individuals).

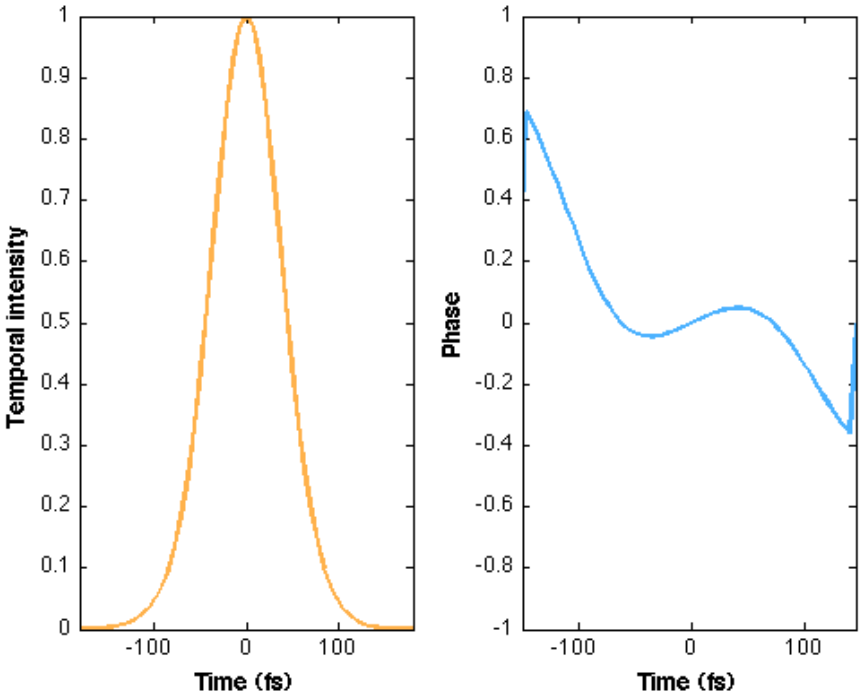

Figure 4.22 Reconstructed Temporal Intensity and Phase. Results for the best individual of a 14 generation run of the GA (the profile with the best detection efficiency out of 14 x 21 individuals).

The result is a pulse with a FWHM duration of about 90 fs and a bandwidth of 9.7 nm. As expected, the spectral phase is essentially flat, a clear indication that our unmodulated single photons are in a transform-limited spectrotemporal mode.

4.4.2 Dispersed single photon

The next step was the detection of the single photon after it travelled through the 10-cm long glass block in the new setup. As we did before, we first performed a manual scan of the quadratic coefficient of the spectral phase imposed by the SLM to the LO in order to find the optimum value for maximum homodyne detection efficiency.

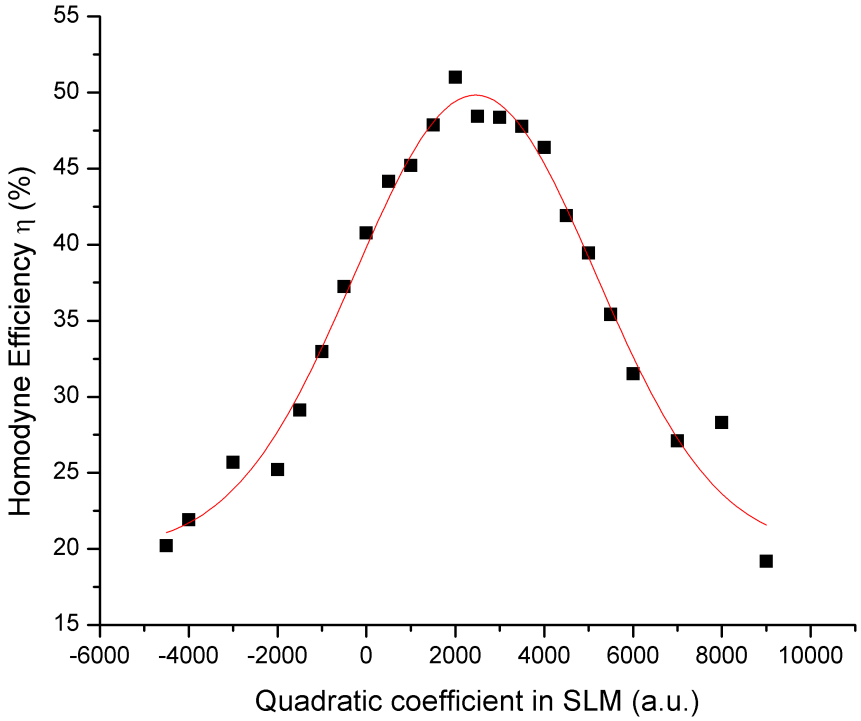

Figure 4.23 Plotted Homodyne efficiency with quadratic coefficient of the SLM for a dispersed single photon. We see that the SLM adds positive dispersion to the LO to match that of the glass in the path of the single photon

We find the best efficiency for a quadratic coefficient of about +2450, which should be compared with the settings of Table xx for the amount of dispersion needed to compensate that of approximately the same length of glass.

By performing the FROG measurements in these conditions we find that the optimal LO pulse now possesses a clear quadratic spectral phase with ϕ_2=6100 fs^2.

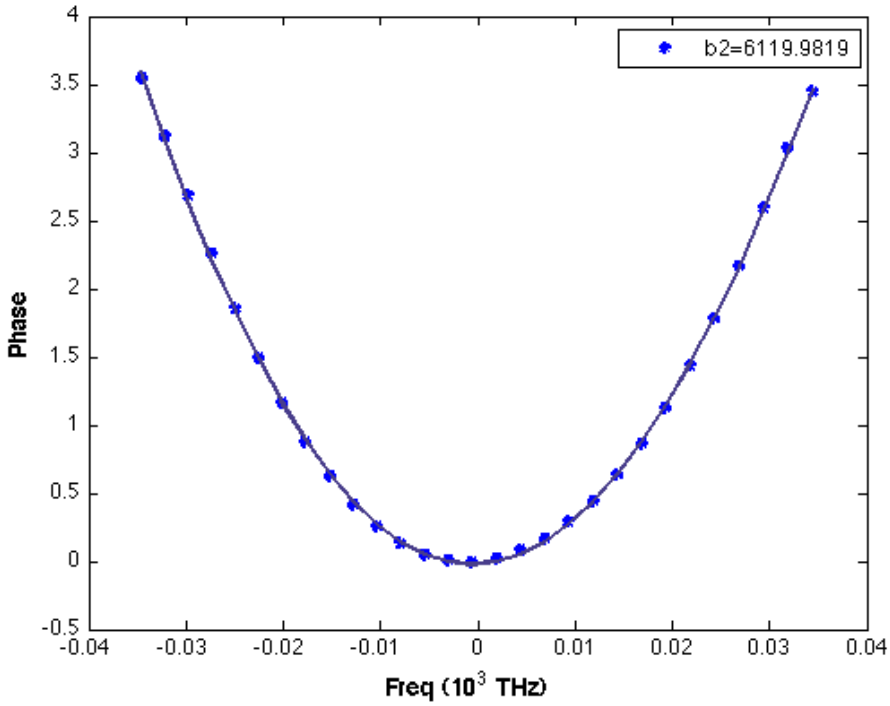

Figure 4.24 Plotted spectral phase for a dispersed single photon, retrieved after a phase optimisation procedure. Quadratic coefficient b_2=6120 fs^2

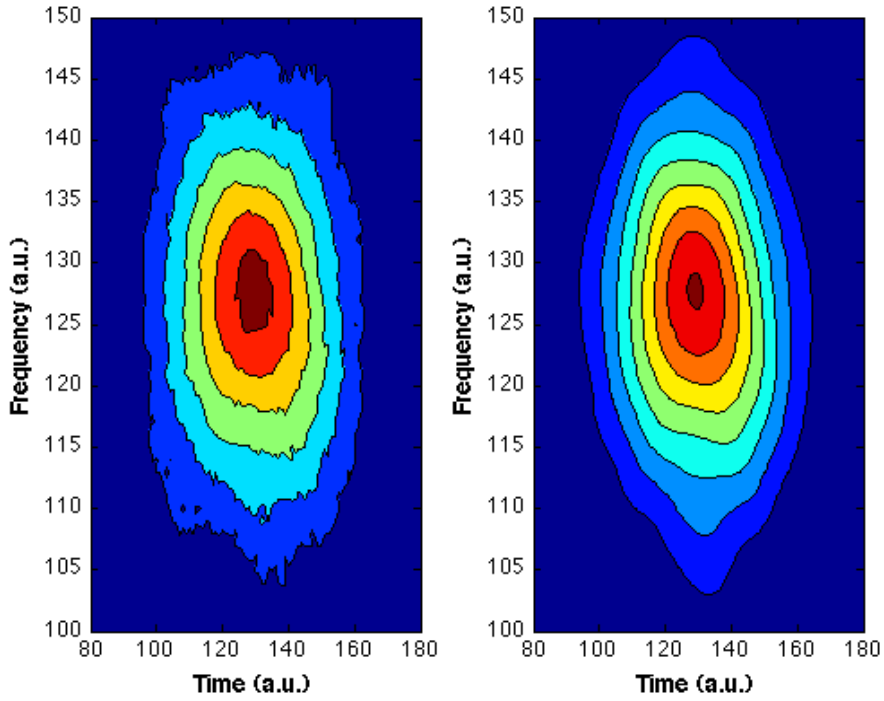

Figure 4.25 Experimental FROG trace measured and retrieved, for a spectrally dispersed single photon.

The next step was to test the genetic algorithm with a phase-only modulation for these long, spectrally dispersed, single photons. Below are reported the FROG measurements for the best individual of a 128 generation GA run.

It is interesting to see that the best result found with the GA is in a pretty good agreement with the one found manually. Here again, the LO pulse possesses a clear quadratic spectral phase with almost the same coefficient, and the measured pulse duration and bandwidth are 225 fs and 10.3 nm, respectively.

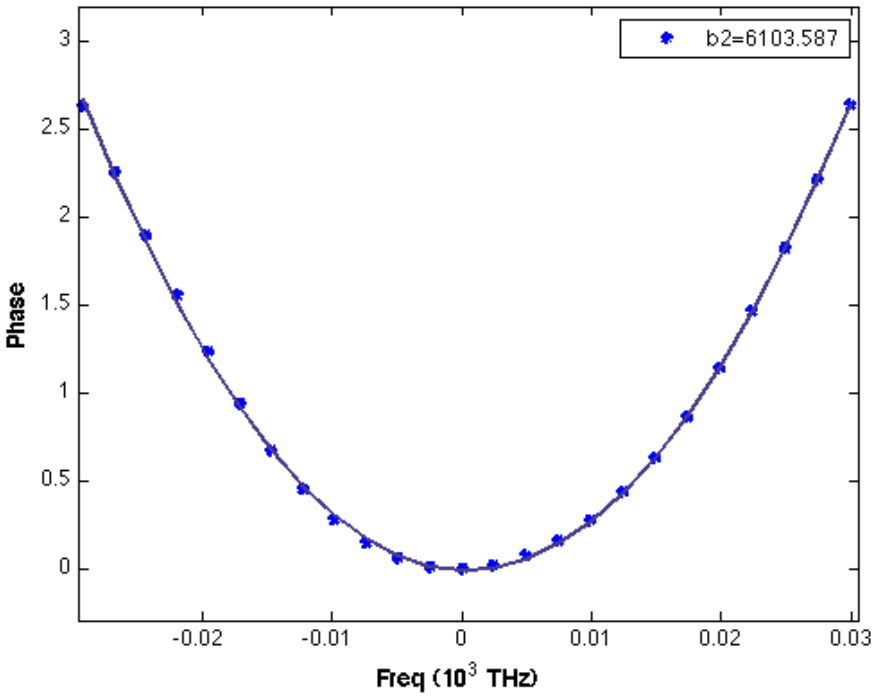

Figure 4.26 Plotted spectral phase for a dispersed single photon. Result of the best individual of a 128 generation run of the GA (the profile with the best detection efficiency out of 128 x 21 individuals). Quadratic coefficient b_2=6103 fs^2

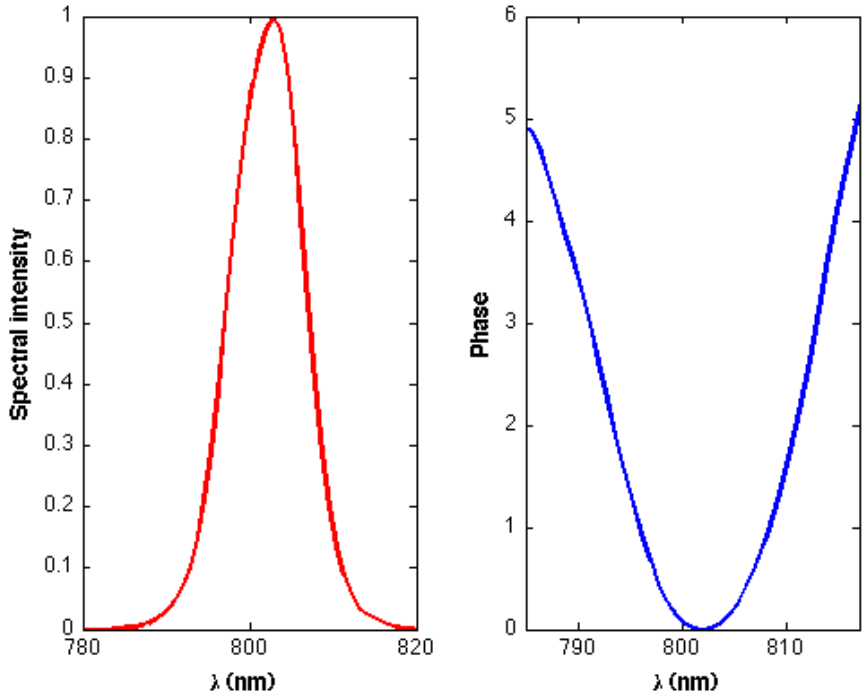

Figure 4.27 Reconstructed Spectral Intensity and phase, result of the best individual of a 128 generation run of the GA (the profile with the best detection efficiency out of 128 x 21 individuals).

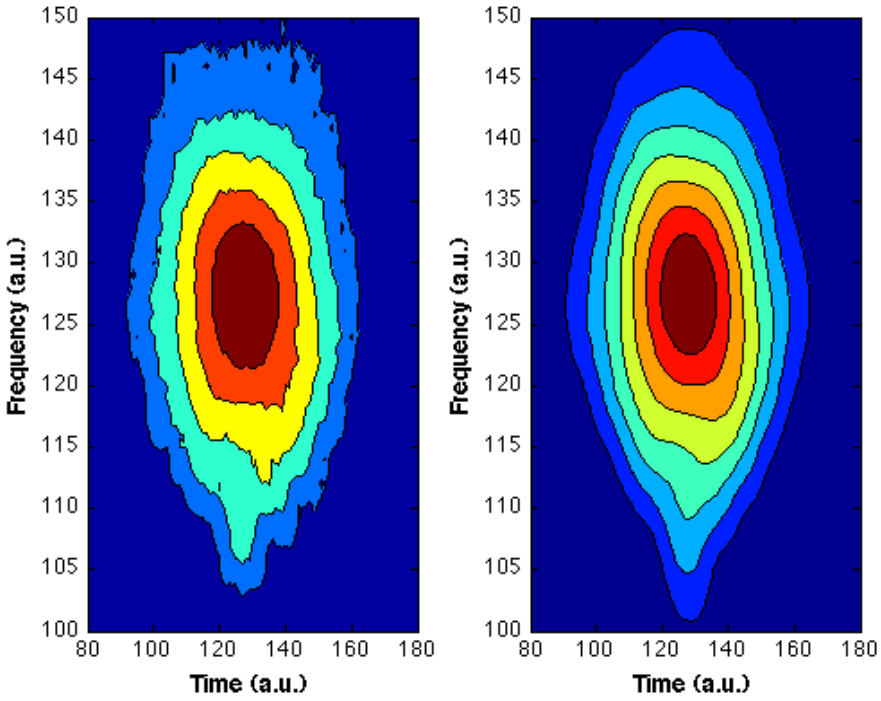

Figure 4.28 Experimental FROG trace, measured and retrieved. Result of the best individual of a 128 generation run of the GA (the profile with the best detection efficiency out of 128 x 21 individuals).

This is one more proof that, using the genetic algorithm in combination with homodyne detection, is very effective in unraveling the unknown spectrotemporal mode of a quantum state, even without any prior information at hand. What is also important to note is that the mode identification can be performed automatically, without any need for a human intervention, and this scheme is able to self-adapt to slow environmental changes rather than having to deal with them as an obstacle.

CHAPTER 5

CONCLUSIONS AND FUTURE DIRECTIONS

The possibility to access the rich mode structure of quantum states of light opens doors to a plethora of potential applications in science, as this also means being able to use new ways of encoding and decoding quantum information. In this thesis I have shown that with our adaptive experimental method, which combines for the first time advanced coherent-control and quantum optics techniques to measure quantum states of light in unknown modes [1], we have made a new important step in this direction.

We performed the first tests of this novel experimental technique by applying it to single photon states. Using homodyne detection efficiency as a fitness parameter for a genetic algorithm, we were able to recover the spectrotemporal profile of our ultrashort single photons. In particular, we have tested the experimental technique on different spectrotemporal profiles: on unmodulated single photons as produced by our heralded source based on spontaneous parametric down-conversion; on dispersed single photons obtained by passing them through 10 cm of a BK7 glass block; on spectrally narrow and spectrally double-peaked single photons produced by shaping the pump pulse. A genetic algorithm has proven able to trace any change made on the single-photon mode and reliably map it to the mode of an intense coherent pulse, which could then be fully analysed by standard pulse characterization techniques. The technique has also shown to adapt to slow changes of the mode of the quantum state that occur on long time scales.

These results are only the starting point for this method. Even if tested here on single-photon Fock states and, contrary to previous techniques, our

scheme is suitable for a much broader class of states, including bright multi-photon ones. It only requires that a fitness parameter is at hand. An interesting follow-up will be to probe the quantum properties of squeezed light emitted from a high-gain SPDC source, like the ones employing waveguides. For such states, the level of measured quadrature squeezing could be used as the fitness parameter.

Based on an adaptive optimization algorithm, our method does not rely on preliminary theoretical knowledge of the mode occupied by the quantum state to be measured, but rather automatically takes into account all the characteristics of experimentally generated states without any preliminary information. To grasp this concept imagine that it can allow one to recover ''unreadable'' quantum features or compensate possible deformations encountered during propagation in arbitrary dispersive or diffractive channels.

Future possibilities to upgrade the setup could involve including spatial mode characterization, so that the full spatiotemporal profile of the quantum state can be measured and exploited. The idea would be to use deformable mirrors as a replacement of the current spatial mode-matching scheme in the LO beam and add the spatial degrees of freedom as free parameters in the genetic algorithm. Deformable mirrors [57] are mirrors whose surface can be deformed, and whose shape can be controlled using wavefront sensors and a real-time control system. The point is that it is possible for the genetic algorithm to introduce random spatial profiles as well as spectrotemporal ones, and again the homodyne efficiency can be a reliable criterion for the matching of the two beams and therefore as a fitness parameter. This could be a significant boost for the scheme, as not only will it allow further optimisation of the homodyne efficiency, but also it will decrease

substantially the time needed for daily alignment procedures related to spatial mode-matching.

Furthermore, our method is not by any means restricted to mode characterization. It can go well beyond that, by probing and manipulating the quantum properties of light states, for example realizing mode-selective state displacements in phase space (the displacement operation has been proved to be crucial for the preparation of cat and NOON states). It is also interesting to note that homodyne measurements with a shaped LO might not only be used in the detection stage, but also in the conditional preparation of multimode quantum states.

We have indeed created a device that not only retrieves the "shape" of the light, but directly gives the tools for manipulating and analyzing it. It has been shown in this thesis how one can retrieve information about the mode structure of the light state, but also how we can probe coherences among different modes. Our adaptive detector opens the way for advancing in the manipulation of multimode states. In this respect, our method would allow one to find and access the whole family of quantum correlated modes existing in multimode light. It would also allow detecting coherent combinations of them, which could be used as a mean of encoding information and further research the nature of multipartite entanglement experimentally.

As Dirac famously once said: "At the heart of quantum mechanics lies the superposition principle" [80]. This is the direction we wish to go to, and the first steps have been taken with the measurements of a spectrally double peaked single photon, and proof of its inner coherence. In the future, we plan to apply the idea to a single photon with more than two spectral peaks, and we have already started testing the method with a birefringent a-BBO crystal,

that works in the same way as the Michelson interferometer for the pump beam shaping, but offers more possibilities and stability to the setup. We also hope that this will be the solution to the degradation of the spatial visibility we observed when we measured the spectrally double-peaked single photon produced with the Michelson interferometer.

New exciting opportunities can emerge if quantum states of light are generated and detected in multiple arbitrary modes, as this provides access to a much larger Hilbert space for encoding, manipulating, and decoding quantum information. The possibility of encoding information in multiple independent quantum channels is not a utopia. Multimode quantum states can provide this possibility, and aside from research in orbital angular momentum that has to do with the spatial domain, here we investigated the spectrotemporal degrees of freedom and saw how advantageous they'd be with respect to other physical properties of light. This is indeed a powerful, versatile scheme, with a long future path. It allows one to deeply probe the structure of complex quantum states, besides optimising their detection. The presented experiments could for example pave the road to the analysis of the intrinsic multi-Schmidt-mode character of quantum states naturally generated in parametric down-conversion pumped by short pulses, envisaged to support multimode quantum information processing [81-83].

It could be argued that the use of a pulse shaping technique based on a SLM is only possible when dealing with spectrally broadband photons. This is merely a limitation; in our opinion the broadband regime is the current frontier and probably the future direction in the field. The ultrashort regime was a choice and not a restriction, it is actually much more challenging to work with pulses lasting ~100 fs and, more interesting too. Ultrashort pulses are the future, since their extended bandwidth allows encoding of more

information in ST modes, higher rate of information transfer, more precise timing etc. Alternatively, if one wanted to apply the technique on temporally long photons, the solution would be simple: replace the SLM with some slower optoelectronic device (like an electro-optical modulator), a technically less demanding (and less interesting) task, and the optimization procedure would still hold.

To conclude, I have presented you the experimental setup as whole and the progress that has been made during the three years of study for my doctorate, taking into account all that has been previously introduced as a theory. Lastly but more importantly, I have presented you with solid argumentation why I believe in this technique's pioneering role in the future of quantum optics.

ACKNOWLEDGEMENTS

Just as we do in quantum mechanics, we think of everything that is going to happen in life in terms of probabilities. And the probability of a person having one or more " Oscar moments" as I like to call them, is very low. For this reason, I would like to treat this acknowledgements page at the end of this thesis as one of those moments. It's impossible to know if and when I will have one. I always like to start with a touch of humour, and in this case I feel like I owe so much to other people that it feels silly that I'm the one getting the "Oscar" moment. For this, I wish to share with the reader here my personal view of who and why I need to be thankful for, that helped even in the slightest way for finally getting this thesis to the printer, my absolutely favourite stage of the thesis preparation process.

I would first like to thank Prof. Massimo Inguscio, who was the first person to believe in me, and offered me this wonderful opportunity to study my topic of choice with a top-notch experimental group in a great city like Florence, in a country of incredible background and wealth in every aspect. His amazing spirit and optimism has been the secret steering force behind a lot of experimental work.

A super enormous thank you goes to my supervisor Marco Bellini, without whom no part of this work would have been possible from the very first measurement to the last sentence of this thesis. No words are enough to express the gratitude I owe to his brilliance as a physicist, but also to his modesty. He has trained me in these three years showing incredible patience and continuous availability for me; never once did he deny me of his precious time and expertise- despite his load of responsibilities that comes together

with his status. Thank you for sticking by me through the hard times, until the very critical final moments before the deadline of submission of this thesis. Your guidance and support have been invaluable to me.

I would like to thank Alessandro Zavatta, for his profound experimental knowledge, contrivances and experience without which any task in the lab would have seemed impossible, and for teaching me the depth of persistence that it takes for experiments to happen.

I would like to thank Katiuscia N. Cassemiro, who in her short visit in our lab has pushed me and the experiment to the next level thanks to her inexhaustible determination and constant inspiration. She has managed to give me so much in so little time (with respect to the experimental time scales). Thank you for taking the time to be my teacher, regardless of the time challenge you had to face.

I would like to thank Giovanni Venturi for setting up the Genetic Algorithm, together with Alessandro they are the giants of programming, and for his resourcefulness with Matlab when I needed it.

Thank you to my friend Antonio Sales, for bringing the samba air in the lab, during his time there, for showing me the "happiness" of measurements that comes with tireless determination and focus. For the positive attitude he dealt with the daily lab routine and PhD life.

Thank you to Massimiliano Locatelli for the collaboration during the first year, and the fascinating debates we had about the SPDC alignment, it has been a pleasure to work together with you.

Thank you to Prof. Ady Arie for bringing a wonderful working atmosphere in our lab, and showing me the fun in teamwork despite the brevity of his visit.

Thank you to Rodolfos Karaiskakis, a very talented teacher who transmitted his passion for physics to me.

Thank you to my college professor Prof. Argyris Nikolaides and my E.U. stage supervisor Anna Katrami for their encouragement and support to my decision to pursue a PhD.

Thank you also to a group of people from GSF (Gruppo Speleologico Fiorentino), who welcomed me in the most fun extracurricular activity I have ever been involved in, even with my lack of experience, for their support and friendship, for making my Florence experience much more colourful.

Thank you to my wonderful parents, who still managed to bring me up in a multicultural environment teaching me open-mindedness, embracing other cultures and ideas despite the fact that I was raised in a tiny village, in a still quite conservative society of Cyprus. For their incredible support in my every life choice and personal sacrifice that never stops. My father, who taught me to face everything in life with a sense of humour. Thank you to my wonderful mother, the most incredible person I have met, and will have met, who believed anything is possible and wouldn't let any small or big thing get in the way of what she set her mind to. The most kind, strong-willed, determined and optimistic person I have met, who lived the last year of her life, fighting with cancer but never allowed me to think about the possibility she might loose the battle, in order to keep me focused on my last year of the doctorate. I will always seek inspiration in her actions, unbreakable spirit and self-sacrifice.

Thank you to the rest of my family and friends for their support during the hardest time of my life and especially my nounna, who helped to take care of my mother while I was away. I am deeply touched.
Thank you to my older sister Elena, for believing in me, for being a mother and a best friend at the same time, and for her major positive influence in my life.

Thank you to Francesco Cataliotti and Chiara Corsi for their kind effort and support.

The reader now may have a rough idea why completing my PhD studies feels something like climbing the top of mountain Everest. As Stephen Hawking once said: “Remember to look up at the stars and not down at your feet. Try to make sense of what you see and wonder about what makes the universe exist. Be curious, and however difficult life may seem, there is always something you can do, and succeed at. It matters that you don’t just give up.” This makes me think that if a person like him didn’t let this extreme kind of disability stop him in doing research and accomplishing what he has as one of the greatest physicists of all times, then the rest of us have no excuse. We must search for inspiration in life and never give up, no matter how painful it gets.

I would like to emphasize how it was worth it all. I am finishing my PhD much richer in knowledge, experience and strength, as well as a personality. Thank you to all the people who made a contribution to this. As well as to the people who collaborated so well in bringing coffee to my vicinity, starting from the workers in the coffee fields of South America, to the producers, to the importers, to the anonymous person serving it at the bar. Couldn’t have done it without them.

Finally, I would like to thank the reader, especially the one who has read the entire thesis, without skipping chapters and going directly to the conclusions, or even worse to this acknowledgements page, no matter how curious or impatient he might have really been.

REFERENCES

[1] Adaptive Detection of Arbitrarily Shaped Ultrashort Quantum Light States, C.Polycarpou, K.N. Cassemiro, G.Venturi, A.Zavatta and M.Bellini, PRL 109, 053602, (2012).

[2] Can quantum-mechanical description of physical reality be considered complete? A.Einstein, B.Podolsky and N.Rosen, Phys. Rev. 47, 777-780, (1935).

[3] Pulsed Energy-Time Entangled Twin-Photon source for quantum communication, J. Brendel, N. Gisin, W. Tittel, and H. Zbinden Phys. Rev.Lett. 82, 2594-2597 (1999).

[4] Remote preparation of arbitrary time-encoded single-photon ebits, A. Zavatta, M. D'Angelo, V. Parigi, and M. Bellini, Phys. Rev. Lett. 96, 020502 (2006).

[5] Quantum states made to measure, K. Banaszek, R. Demkowicz-Dobrzanski, and I. A.Walmsley, Nature Photon. 3, 673 (2009).

[6] Quantum-enhanced measurements: beating the standard quantum limit, V. Giovannetti, S. Lloyd, and L. Maccone, Science 306, 1330 (2004).

[7] Quantum cryptography using larger alphabets, H. Bechmann-Pasquinucci and W. Tittel, Phys. Rev. A 61, 062308 (2000).

[8] Security of quantum key distribution using d-level systems, N.J. Cerf, M. Bourennane, A. Karlsson, and N. Gisin, Phys. Rev. Lett. 88, 127902 (2002).

[9] Entanglement of the orbital angular momentum states of photons, A. Mair, A. Vaziri, G. Weihs, and A. Zeilinger, Nature (London) 412, 313 (2001).

[10] Measuring the orbital angular momentum of a single photon, J. Leach, M. J. Padgett, S. M. Barnett, S. Franke-Arnold, and J. Courtial, Phys. Rev. Lett. 88, 257901 (2002).

[11] Quantum limits on Optical resolution, M.I. Kolobov and C. Fabre, Phys. Rev. Lett. 85, 3789(2000).

[12] Experimental realization of sub-shot-noise quantum imaging, G. Brida, M. Genovese, and I. R. Berchera, Nature Photon. 4, 227 (2010).

[13] Optical entanglement of co-propagating modes, J. Janousek, K. Wagner, J.-F. Morizur, N. Treps, P.K. Lam, C.C. Harb, and H.-A. Bachor, Nature Photon. 3, 399 (2009).

[14] One-way quantum computing in the optical frequency comb, N. C. Menicucci, S. T. Flammia, and O. Pfister, Phys. Rev. Lett. 101, 130501 (2008).

[15] Quantum improvement of time transfer between remote clocks, B. Lamine, C. Fabre, and N. Treps, Phys. Rev. Lett. 101, 123601 (2008).

[16] Generation and characterization of multimode quantum frequency combs, O. Pinel, P. Jian, R. M. de Arau´jo, J. Feng, B. Chalopin, C. Fabre, and N. Treps, Phys. Rev. Lett. 108, 083601 (2012).

[17] Differential phase shift quantum key distribution K. Inoue, E. Waks, and Y. Yamamoto, Phys. Rev. Lett. 89, 037902 (2002).

[18] Optical quantum memory, A. I. Lvovsky, B. C. Sanders, and W. Tittel, Nature Photon. 3, 706 (2009).

[19] Towards high-speed optical quantum memories, K. F. Reim, J. Nunn, V. O. Lorenz, B. J. Sussman, K. C. Lee, N.K. Langford, D. Jaksch, and I.A. Walmsley, Nature Photon. 4, 218 (2010).

[20] Single photons made-to-measure, G. S. Vasilev, D. Ljunggren, and A. Kuhn, New J. Phys. 12, 063024 (2010).

[21] Quantum optical waveform conversion, D. Kielpinski, J. F. Corney, and H. M. Wiseman, Phys. Rev. Lett. 106, 130501 (2011).

[22] Heralded generation of ultrafast single photons in pure quantum states P. J. Mosley, J. S. Lundeen, B. J. Smith, P. Wasylczyk, A. B. U'Ren, C.Silberhorn, and I. A. Walmsley, Phys. Rev. Lett. 100, 133601 (2008).

[23] Phase shaping of single-photon wavepackets, H.P. Specht, J. Bochmann, M. Mucke, B. Weber, E. Figueroa, D.L. Moehring, and G. Rempe, Nature Photon. 3, 469 (2009).

[24] Electro-optic modulation of single photons, P. Kolchin, C. Belthangady, S. Du, G. Y.Yin, and S. E. Harris, Phys. Rev. Lett. 101, 103601 (2008).

[25] Temporal shaping of entangled photons, A. Pe'er, B. Dayan, A.A. Friesem, and Y. Silberberg, Phys. Rev. Lett. 94, 073601, 2005 Phys. Rev. Lett. 94, 073601 (2005).

[26] Continuous-variable optical quantum-state tomography, A. I. Lvovsky and M. G. Raymer, Rev. Mod. Phys. 81, 299 (2009).

[27] Optimizing homodyne detection of quadrature-noise squeezing by local-oscillator selection, J. H. Shapiro and A. Shakeel, J. Opt. Soc. Am. B 14, 232 (1997).

[28] Optical pattern recognition via adaptive spatial homodyne detection, M. T. L. Hsu, J. Knittel, J.-F. Morizur, H.-A. Bachor, and W. P. Bowen, J. Opt. Soc. Am. A 27, 2583 (2010).

[29] Spectral density matrix of a single photon measured, W.Wasilewski, P.Kolenderski, R.Frankowski, PRL 99, 123601, 2007, Phys. Rev. Lett. 99, 123601 (2007).

[30] Quantum state tomography with array detectors, M. Beck, Phys. Rev. Lett. 84, 5748 (2000).

[31] Joint quantum measurement using unbalanced array detection, M. Beck, C. Dorrer, and I. A. Walmsley, Phys. Rev. Lett. 87, 253601 (2001).

[32] Mode optimization for quantum-state tomography with array detectors, A. M. Dawes, M. Beck, and K. Banaszek, Phys. Rev. A 67, 032102 (2003).

[33] Correlation functions for coherent fields, U. M. Titulaer and R. J. Glauber, Phys. Rev. 140, B676 (1965).

[34] Measuring the quantum state of light, Ulf Leonhardt

[35] Introductory Quantum Optics, C.C.Gerry and P.L. Knight, Cambridge University Press, Cambridge, UK, (2005).

[36] Probing fundamental quantum rules by the generation, manipulation and characterisation of nonclassical states of light, PhD thesis, Valentina Parigi, (2008).

[37] Probing quantum commutation rules by addition and subtraction of single photons to/from a light field, V. Parigi, A. Zavatta, M. S. Kim, and M. Bellini, Science, 317, 1890 (2007).

[38] Experimental demonstration of the bosonic commutation relation via superpositions of quantum operators on thermal light fields, A. Zavatta, V. Parigi, M. S. Kim, H. Jeong, and M. Bellini, Phys. Rev. Lett., 103, 140406, (2009).

[39] Observation of simultaneity in Parametric Production of Photon Pairs, D.C. Burnham and D.L.Weinberg, Phys.Rev.Lett. (1970).

[40] Photon Correlations in the parametric frequency splitting of light, B.R.Mollow, PRA Volume 8, Number 5, (1973).

[41] Spatiotemporal coherence properties on entangled light beams generated by parametric down-conversion, A.Joobeur, B.E.A. Saleh, M.C.Teich, Phys. Rev. A 50, 2249-3361, (1994).

[42] Spatial properties of spontaneous parametric down-conversion and their effect on induced coherence without induced emission, T.P.Grayson and G.A.Barbosa, Phys.Rev. A 49, 2948-2961, (1994).

[43] Quantum state reconstruction of the single-photon Fock state, A. I. Lvovsky, H. Hansen, T. Aichele, O. Benson, J. Mlynek, and S. Schiller, Phys. Rev. Lett. 87, 050402 (2001).

[44] Tomographic reconstruction of the single-photon Fock state by high-frequency homodyne detection, A.Zavatta, S.Viciani and M.Bellini, Phys. Rev. A 70, 053821 (2004).

[45] Optical mode characterization of single photons prepared by means of conditional measurements on a biphoton state, T. Aichele, A. I. Lvovsky, and S. Schiller, Eur. Phys. J. D 18, 237 (2002), Eur. Phys. J. D 18, 237 (2002).

[46] Nonlocal modulations on the temporal and spectral profiles of an entangled photon pair, S. Viciani, A. Zavatta, and M. Bellini, PRA 69, 053801, 2004, Phys. Rev. A 69, 053801 (2004).

[47] Parametric down-conversion with coherent pulse pumping and quantum interference between independent fields, Z. Y. Ou, Quantum Semiclassic. Opt. **9**, 599 (1997).

[48] Nonlocal pulse shaping with entangled photon pairs, M. Bellini, F. Marin, S. Viciani, A. Zavatta, and F.T. Arecchi, Phys. Rev. Lett. 90, 043602, (2003).

[49] On the quantum correction for thermodynamic equilibrium, E. Wigner, Phys. Rev. 40, 749 (1932)

[50] Determination of quasiprobability distributions in terms of probability distributions for the rotated quadrature phase, K. Vogel and H. Risken, Phys. Rev. A 40, 2847, (1989)

[51] Statistics of difference events in homodyne detection, Vogel, W, and Grabow, J. *Phys, Rev. A* 47, 4227, (1993)

[52] A guide to experiments in quantum optics, H.A. Bachor and T. Ralph

[53] Time-domain analysis of quantum states of light: noise characterization and homodyne tomography, A. Zavatta, M. Bellini, P. L. Ramazza, F. Marin, and F. T.Arecchi, J.Opt. Soc.Am.B. Vol.19, No.5, May 2002, J. Opt. Soc. Am. B 19, 1189 (2002).

[54] Quantum engineering in non-linear optics, PhD Thesis, Alessandro Zavatta

[55] Sub-two cycle pulses from a Kerr-lens mode-lcoked Ti:Sapphire laser, U. Morgner *et al.,* Opt. Lett. **24**, 411 (1999)

[56] Continuous-wave mode-locked Ti:sapphire laser focusable to 5 x 10^{13} W/cm^2 , L. Xu, G. Tempea, Ch. Spielmann, F. Krausz, A. Stingl, K. Ferencz, and S. Takano, Opt. Lett. **23**, 789, (1998)

[57] Femtosecond pulse shaping using spatial light modulators, A.M.Weiner, Rev.Sci.Instrum.Vol.71., No.5 (1929-60), (2000)

[58] Ultrashort laser pulse phenomena, J.-C. Diels and W. Rudolf, 2nd edition, (2006)

[59] A newcomer's guide to ultrashort pulse shaping and characterisation, A.Monmayrant, S.Weber, B.Chatel, J.Phys. B: At. Mol. Opt. Phys. 43, 103001, (2010)

[60] Automated two-dimensional femtosecond pulse shaping," J. C. Vaughan, T. Feurer, and K. A. Nelson, J. Opt. Soc. Am. B **19**, 2489-2495 (2002)

[61] Multidimensional control of femtosecond pulses by use of a programmable liquid-crystal matrix," T. Feurer, J. C. Vaughan, R. M. Koehl, and K. A. Nelson, Opt. Lett. **27**, 652-654 (2002)

[62] Analysis of programmable ultrashort waveform generation using liquid-crystal spatial light modulators, M.M. Wefers and K.A. Nelson, J.Opt.Soc.Am.B Vol.12, No.7, (1995)

[63] Ultrafast optical pulse shaping: A tutorial review, A. M. Weiner, Optics Communications, 284, 3669-3692 (2011), Opt. Commun. 284, 3669 (2011).

[64] Femtosecond optical pulse shaping and processing, A.M.Weiner, Prog. Quant.Electr. vol.19, p. 161-237, (1995)

[65] Matrix formalism for pulse compressors, O.E.Martínez, IEEE Journal of Quant.Electr. Vol.24, No.12, December, (1988)

[66] Negative dispersion using pairs of prisms, R.L. Fork, O.E. Martinez and J.P. Gordon, Opt. Letters 9, 150-152, (1984)

[67] Generalized multiple-prism dispersion theory for laser pulse compression: higher order phase derivatives, F.J. Duarte, Appl. Phys B 96:809-814, (2009)

[68] Adaptive Femtosecond Quantum Control, PhD Thesis, by Tobias Brixner, (2001)

[69] SLM User manual, Cri

[70] Single-Cycle Nonlinear Optics, Goulielmakis et al., Science, (2008)

[71] The general theory of first-order spatio-temporal distortions of Gaussian pulses and beams, Trebino et al, Optics Express, Vol. 13, No.21, October (2005)

[72] Spatio-temporal couplings in ultrashort laser pulses, Trebino et al., Journal of Optics 12, 093001, August (2010)

[73] Measuring ultrashort laser pulses in the time-frequency domain using frequency-resolved optical gating, Trebino et al & D.J.Kane, Rev. Sci. Instrum., Vol.68, No.9, Sep. (1997)

[74] FROG User manual, Mesaphotonics

[75] Generation of Optical Harmonics, Franken et al, PRL 7, 118-119 (1961)

[76] Second harmonic generation from regeneratively amplified femtosecond laser pulses in BBO and LBO crystals, Zhang et al, J. Opt. Soc. Am. B/Vol. 15, No. 1/January (1998)

[77] Quantum Control of Photoinduced Chemical Reactions, PhD Thesis, Daniel Wolpert, (2008)

[78] Evolutionary algorithms and their application to optimal control studies, D. Zeidler, S. Frey, K.L. Kompa, and M. Motzkus, Phys. Rev. A 64, 023420 , (2001).

[79] Femtosecond pulse shaping by an evolutionary algorithm with feedback, T. Baumert, T. Brixner, V. Seyfried, M. Strehle, and G. Gerber, Appl. Phys. B 65, 779, (1997), Appl. Phys. B 65, 779 (1997).

[80] The principles of Quantum Mechanics, P.A.M. Dirac, Clarendon, Oxford, (1958).

[81] Continuous frequency entanglement: Effective finite Hilbert space and entropy control, C. K.Law, I. A. Walmsley, and J. H. Eberly, Phys.Rev.Lett. 84, 5304 (2000).

[82] Pulsed squeezed light: Simultaneous squeezing of multiple modes, W.Wasilewski, A. I.Lvovsky, K.Banaszek, and C. Radzewicz, Phys. Rev. A 73, 063819 (2006).

[83] Probing multimode squeezing with correlation functions, A. Christ, K. Laiho, A. Eckstein, K.N. Cassemiro, and C. Silberhorn, New J. Phys. 13, 033027 (2011).

PRESS RELEASES

- Focus: “Measuring the Shape of a Photon”, Physics 5, 86 (2012), DOI: 10.1103/Physics.5.86, Aug 3, 2012
- Physicsworld: “Photon shape could be used to encode quantum information”, Aug 10, 2012
- New Scientist: “Quantum “alphabet” easier to read with laser booster”, Aug 16, 2012
- 2physics: “The shape of quantum light”, Sep 16, 2012

ITALIAN PRESS

- La repubblica: “Il Cnr misura forma della luce”, Aug 1, 2012
- ANSA (Scienza&Tecnica): “Misurata la forma della luce”, Aug 1, 2012
- La Nazione, Firenze & Sesto Fiorentino, Sept 15,2012